Investigation of the Discovery Potential for Supersymmetry in Tau Final States and Measurement of the Tau Identification Efficiency for the ATLAS Experiment.

Dissertation zur Erlangung der Doktorwürde

Vorgelegt von

Debra Lumb

Fakultät für Mathematik und Physik
Albert-Ludwigs-Universität Freiburg

Contents

Acknowledgements

First and foremost I would like to thank Prof. Gregor Herten for giving me the opportunity to come to Freiburg to do a PhD, and for his support during my time as a PhD student. I would also like to thank Sascha Caron and Xavier Portell for their guidance and support during my PhD and for their enthusiasm towards my work.

I would like to thank all of my ATLAS colleagues in Frieburg for their support with software development and access to datasets, for their help with translation when my German wasn't good enough and for their patience as I adjusted to life in a new country.

I would also like to thank the ATLAS Collaboration, without whom this research would not have been possible.

Finally I would like to thank my friends and family for their unfailing support and encouragement, especially my fiancé Alastair Dewhurst.

Introduction

Particle physics is the study of the most fundamental constituents of matter and radiation and the way in which they interact with one another. Over the past 50 years particle physicists have built a theory that successfully describes the large number of subatomic particles as compositions of just 12 elementary particles: three generations of leptons (e, ν_e; μ, ν_μ; τ, ν_τ) and three generations of quarks (u, d; s, c; t, b); and describes three of the four known interactions between these particles in terms of the exchange of five elementary particles known as gauge bosons. The three fundamental interactions are the electromagnetic interaction, the weak interaction and the strong interaction. This theory, known as the Standard Model of particle physics, has been tremendously successful in explaining and predicting decades of results from a wide range of experiments, in some cases with exceptional precision.

Despite its success, the Standard Model has a number of short-comings that have led particle physicists to believe the Standard Model is only a low-energy approximation of a more fundamental theory. Discovering what lies beyond the Standard Model is one of the main goals of modern particle physics.

One of the most promising candidates for an extension of the Standard Model is Supersymmetry. Supersymmetric models predict the existence of a superpartner for each Standard Model particle, that differs in spin. Such models offer a solution to many of the short-comings of the Standard Model. Since the predicted superparticle partners have not yet been observed, the masses of the superparticles are expected to be higher than those of the Standard Model particles. This difference in mass has fueled the need for larger experiments capable of reaching

the energies needed to produce and allow the observation of such particles.

Searches for supersymmetric particles have been performed by the four experiments of the Large Electron Positron collider (LEP), that was situated at the European Organization for Nuclear Research (CERN). These searches were able to reach a kinematic limit of 209 GeV before the shutdown of LEP in 2000. Searches are currently being performed by the Tevatron Experiments at the Fermi National Accelerator Laboratory in the United States with a centre-of-mass energy of 1.96 TeV. So far no conclusive evidence has been found for the existence of supersymmetric particles at these energy scales. At the end of 2009 the search for Supersymmetry will be taken into a new energy regime with the Large Hadron Collider (LHC) experiments at CERN. The LHC is a proton-proton collider. With a centre-of-mass energy of up to 14 TeV and a design luminosity of 10^{34} $cm^{-2}s^{-1}$, it is the highest energy particle accelerator ever built. Two dedicated multipurpose detector systems, ATLAS and CMS, are installed at the LHC to analyse the proton-proton collisions. The LHC experiments will investigate the existence of the Higgs boson and Supersymmetry and will also further probe the Standard Model by exploring this higher energy domain. If Supersymmetry exists at the energy scale of the LHC, these detectors should be well equipped to observe evidence of it.

This Ph.D. thesis presents a new search strategy to look for supersymmetric particles with the ATLAS detector at the CERN LHC using tau-leptons (τ). In many models of Supersymmetry taus are predicted to be predominantly produced over the other lepton species and so decay modes involving taus are potentially promising for observing evidence of Supersymmetry. However, tau leptons are difficult to separate from the large QCD multijet backgrounds present at high energy hadron colliders, and so these channels are often avoided in search strategies. This thesis shows that inclusive searches using taus can be competitive with other inclusive channels when searching for Supersymmetry with the ATLAS detector.

The measurement of the tau identification and reconstruction efficiency with data will be crucial for any analysis that uses tau objects whether the aim of the anal-

ysis is to look at Standard Model or beyond the Standard Model processes. This thesis presents a new method for measuring the tau identification efficiency in early data, using top quark (t) pair production. This allows measurements of the tau identification efficiency in busy environments such as those that will be found in supersymmetric decay chains.

Chapter 1 presents a brief overview of the Standard Model with particular attention to top quarks, tau leptons and the motivations for Supersymmetry. It also provides a brief introduction to Supersymmetry and a summary of the results of direct and indirect searches for Supersymmetry to date. Chapter 2 introduces the phenomenology of hadron colliders before an introduction to the LHC and the ATLAS experiment in Chapter 3. Chapter 4 describes the process of event simulation used to model particle physics events and describes the simulated samples used in this thesis. Chapter 5 describes the algorithms used by the ATLAS Collaboration to reconstruct physics objects. The use of these algorithms in this thesis and their performance is also described. Chapter 6 presents a new search strategy to look for supersymmetric particles with the ATLAS detector using tau leptons. The motivation for using taus is also discussed. Chapters 7 and 8 present a new method for measuring the tau identification efficiency for the ATLAS experiment using top quark pair production. Chapter 9 provides an overview and summary of this thesis.

Chapter 1

Theoretical Aspects

This chapter provides a brief introduction to the Standard Model of particle physics as motivation for introducing Supersymmetry. A brief introduction to Supersymmetry is also given. More detailed introductions to the Standard Model can be found in various text books, for example Ref. [1–3]. Ref. [4, 5] provide excellent introductions to Supersymmetry.

1.1 The Standard Model

1.1.1 Overview

The Standard Model (SM) attempts to explain all the phenomena of particle physics in terms of the properties and interactions of a small number of fundamental particles; that is, point-like particles without internal structure or excited states [3]. The particle content of the SM is divided by a property of these particles known as spin. This is a quantum number that can take integer or half-integer values. Particles with half-integer spin are known as fermions and particles with integer spin are known as bosons. Fermions are the fundamental particles of matter whereas the SM bosons are the 'force carrying' particles that propagate interactions between fermions.

In the SM the strong, weak and electromagnetic interactions are described by gauge theories. A gauge theory is a field theory in which the Lagrangian remains

invariant under a group of local transformations [6]. Quantisation of the theory introduces quanta of the fields. These quanta can be identified as the spin-1 SM particles known as gauge bosons, which mediate the interactions between fermions. References [7, 8] provide good introductions to Gauge Theories.

The strong interaction is described by Quantum Chromodynamics (QCD); a gauge theory based on the $SU(3)_c$ symmetry group [9]. QCD describes the interactions between particles that carry colour charge i.e. quarks. The interactions are mediated by the spin-1 gluons, which are also coloured. Since the gluons carry colour themselves self-interactions can occur and so the gauge theory is non-Abelian.

The electromagnetic and weak interactions are described by a unified electroweak theory that requires invariance under the combined $SU(2)_L \times U(1)_Y$ groups of transformations generated by the hypercharge Y and the weak isospin T [9]. The index L for the SU(2) component denotes that it only acts on the left-handed part of the fermion fields, the U(1) component acts on both right- and left-handed components. Invariance under the $U(1)_Y$ symmetry group results in the introduction of one massless vector boson field, B_μ and invariance under the $SU(2)_L$ symmetry group results in the introduction of three massless vector boson fields, W_μ^i (where $i = 1, 2, 3$). The W_μ^1 and W_μ^2 boson fields mix to form two charged bosons:

$$W_\mu^\pm = (W_\mu^1 \mp i W_\mu^2)/\sqrt{2}, \tag{1.1}$$

and the B_μ and W_μ^3 fields mix to form the Z_μ and A_μ fields:

$$Z_\mu = \cos\theta_w W_\mu^3 - \sin\theta_w B_\mu, \tag{1.2}$$

$$A_\mu = \sin\theta_w W_\mu^3 + \cos\theta_w B_\mu, \tag{1.3}$$

where θ_w is the weak mixing angle [7]. The A_μ field can be identified as the photon field of the SM. The $W_\mu^\pm$ and Z_μ fields resemble the Standard Model $W^\pm$ and Z gauge bosons but in this description they are restricted to being massless, and

therefore are inconsistent with the massive $W^{\pm}$ and Z bosons. Mass can be introduced to these vector fields by way of the Higgs mechanism through spontaneous symmetry breaking, whilst preserving gauge invariance. Spontaneous symmetry breaking occurs when a system that is symmetric with respect to some symmetry group falls into a vacuum state that is not symmetric. The system then no longer appears to behave in a symmetric way [10].
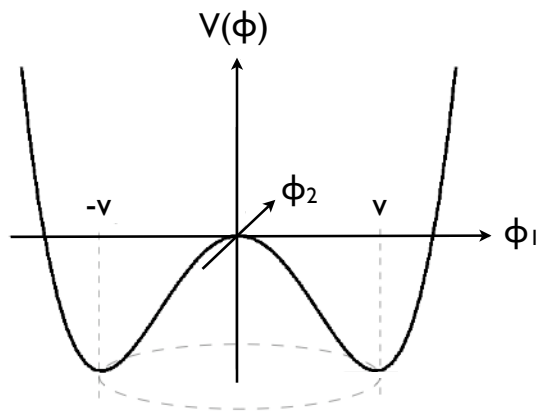
Figure 1.1: The Higgs potential V for the case of a single complex scalar field ϕ.

The Higgs mechanism involves the introduction of a complex scalar field with two components:

$$\phi = \begin{pmatrix} \phi^{+} \\ \phi^{0} \end{pmatrix} \tag{1.4}$$

and its conjugate $\bar{\phi}$ with four degrees of freedom. For a potential of the form:

$$V(\phi, \bar{\phi}) = \mu^2 \phi\bar{\phi} + \lambda(\phi\bar{\phi})^2 \tag{1.5}$$

with $\mu^2 < 0$ and $\lambda > 0$, a degenerate minimum exists [10]. The shape of such a potential is demonstrated in Figure 1.1. It can be seen that the potential also has an unstable state corresponding to $\phi = 0$. This state has U(1) symmetry. Once the system falls into a specific stable vacuum state this symmetry will be lost (spontaneously broken), leaving a minimum with a non-zero vacuum expectation value. The vacuum state is chosen such that the neutral component of the scalar

doublet acquires a vacuum expectation value $v = 246$ GeV [10]. This sets the scale of the electroweak symmetry breaking. One of the four degrees of freedom of the introduced complex scalar field becomes the Higgs boson. From the three remaining degrees of freedom three massless Goldstone bosons are generated, which become the longitudinal polarizations of the $W^{\pm}$ and Z bosons that are needed for them to acquire mass [10]. The Higgs field also enables the fermions to acquire mass via Yukawa couplings between the scalar Higgs and fermions fields. Whilst the Higgs mechanism for electroweak symmetry breaking successfully predicts the masses and couplings of the $W^{\pm}$ and Z bosons that have been observed by experiment, the Higgs boson has yet to observed.

1.1.2 The Tau Lepton

Of particular importance to this thesis is the Standard Model tau lepton (τ). The tau lepton is the heaviest of the three charged lepton species with a mass of (1776.84 ± 0.17) MeV [9]. It is unstable, with a mean lifetime of $(290.6 \pm 1.0) \times 10^{-15}$ s [9] and undergoes only electroweak interactions.

The dominant SM production of taus at the LHC will come from events producing $W^{\pm}$ and Z bosons. The $W^{\pm}$ boson decays to a tau and tau neutrino with a branching fraction of 11.3%. The Z boson decays to a tau-antitau pair with a branching fraction of 3.4%. Figure 1.2 shows the production cross-section for various processes in $pp(p\bar{p})$-collisions as a function of the centre-of-mass energy. It can be seen that the cross-sections for the production of W and Z bosons increases with centre-of-mass energy making the production of these gauge bosons dominant processes at the LHC. It can also be seen that the production cross-section for top quarks increases steeply with centre-of-mass energy. Since the top quark decays almost exclusively to a W boson and a b quark [9] it will also contribute to the production of tau leptons at the LHC.

Due to its large mass the tau lepton, unlike the other lepton species, is able to decay to hadrons as well as leptons. Figure 1.3 illustrates the decay of the tau
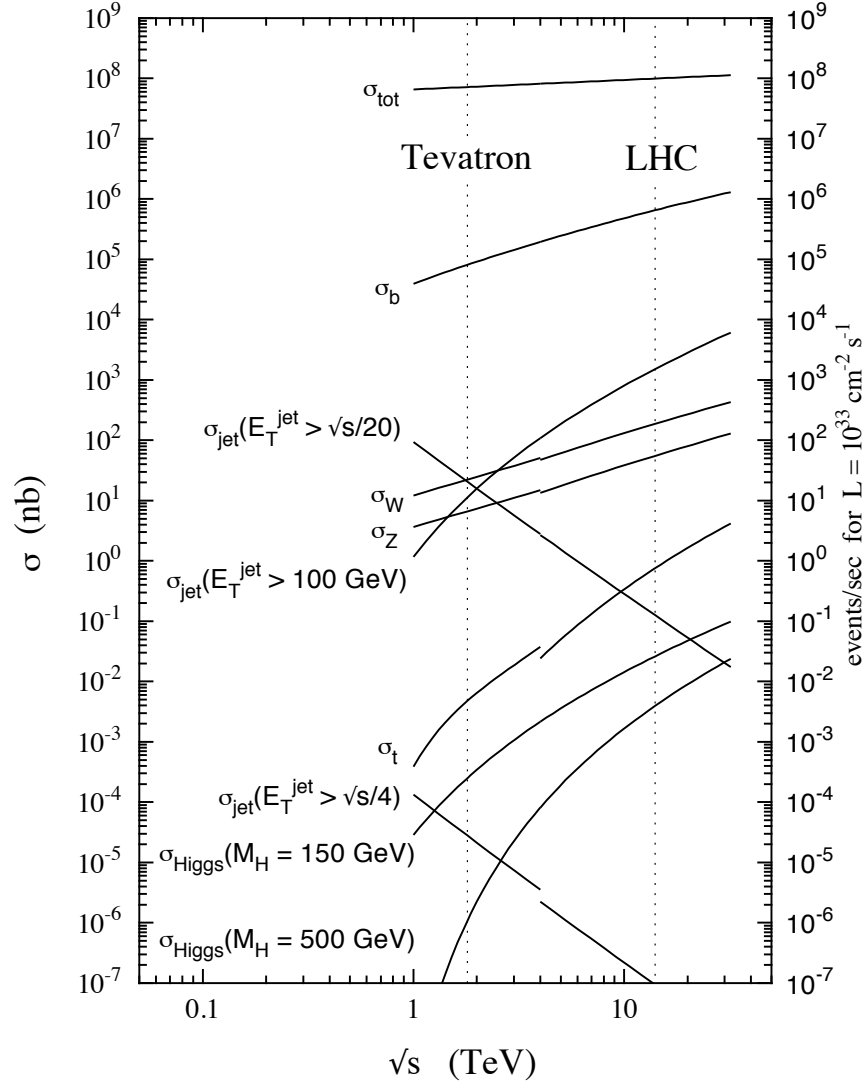
Figure 1.2: Cross-sections for the hard scattering as a function of the centre-of-mass energy $\sqrt{s}$ at the Tevatron and at the LHC. Discontinuities in the cross-section are a result of the difference in the cross-section for $p\bar{p}$ collisions as at the Tevatron and pp collisions as at the LHC. Taken from Ref. [11].

lepton. Table 1.1 demonstrates the main tau decay modes. All tau decays produce at least one neutrino, resulting in missing transverse energy in the detector, leaving only a visible component of hadrons and leptons that must be used to reconstruct the taus. Taus decay leptonically with a branching fraction of $\sim 35\%$ [9]. The electrons and muons from these decays are indistinguishable from other electrons and muons in the detector making it impossible to identify these taus. The hadronic decays, with a branching fraction of $\sim 65\%$ [9], are dominated by final states containing charged and neutral pions. These can be categorised into "1-prong", "3-prong" and "5-prong" modes according to the number of charged particles in the final state. These hadronic decays are challenging to reconstruct due to their similarity to QCD multijets. As such, the tau leptons are the most challenging lepton species to identify at collider experiments where a large background from QCD multijet processes is present.
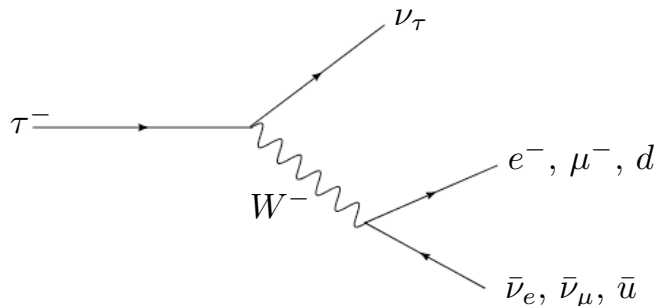
Figure 1.3: Feynman diagram illustrating the decay of the tau lepton via the production of a virtual W boson.

1.1.3 The Top Quark

Of all the observed elementary particles the top quark (t) is the most massive, with a mass of $171.3\pm1.1\pm1.2$ GeV [9]. In pp collisions top quarks are produced in pairs through both gluon-gluon and quark-antiquark scattering as demonstrated in Figure 1.4. At the Tevatron the production of $t\bar{t}$ pairs is kinematically limited to the quark scattering processes but at the LHC the gluon scattering processes will dominate making up $\sim 90\%$ of the production [12]. From Figure 1.2 it can be

6

	Decay Mode	Γ [%]	$\Gamma_i/\Gamma_{lep/had}$[%]
Leptonic	$e^-\bar{\nu}_e\nu_\tau$	17.85	50.7
	$\mu^-\bar{\nu}_\mu\nu_\tau$	17.36	49.3
Hadronic 1-prong	$h^-\nu_\tau$	11.61	17.9
	$h^-\nu_\tau\pi^0$	25.94	40.0
	$h^-\nu_\tau 2\pi^0$	9.51	14.7
	$h^-\nu_\tau 3\pi^0$	1.18	1.8
Hadronic 3-prong	$h-h^+h^-\nu_\tau$	9.80	15.1
	$h^-h+h^-\nu_\tau\pi^0$	4.75	7.3

Table 1.1: Overview of the most common tau decay modes, their individual branching fractions Γ_i and their branching fractions relative to the total leptonic branching fraction Γ_{lep} or total hadronic branching fraction Γ_{had} depending on whether the decay is leptonic or hadronic [9]

seen that the cross-section for $t\bar{t}$-pair production at the LHC will be around 100 times larger than at the Tevatron. With a cross-section of 833 pb for a centre-of-mass energy of 14 TeV and a cross-section of 401 pb for a centre-of-mass energy of 10 TeV, millions of $t\bar{t}$-pairs will be produced every year making the LHC a top quark factory [12].

In the SM, top quarks may also be produced singly via three different processes: W boson and gluon fusion (t-channel), associated production of a top quark and W boson, and s-channel production. These processes are demonstrated on Figure 1.5. The total cross-section for single top production at the LHC with a centre-of-mass energy of 14 TeV is approximately 320 pb [12]. The dominant contribution to this comes from the t-channel process (250 pb). This thesis will focus on the production and decay of $t\bar{t}$-pairs.

The top quark has a lifetime of $\sim 0.5 \times 10^{-24}$ s [9]. As such it is expected to decay before top-flavoured hadrons or $t\bar{t}$-quarkonium-bound states can form. It decays almost exclusively (99%) to a W boson and a b quark [9]. Thus, the final state topologies of $t\bar{t}$ events depend on the decay modes of the W bosons. The W
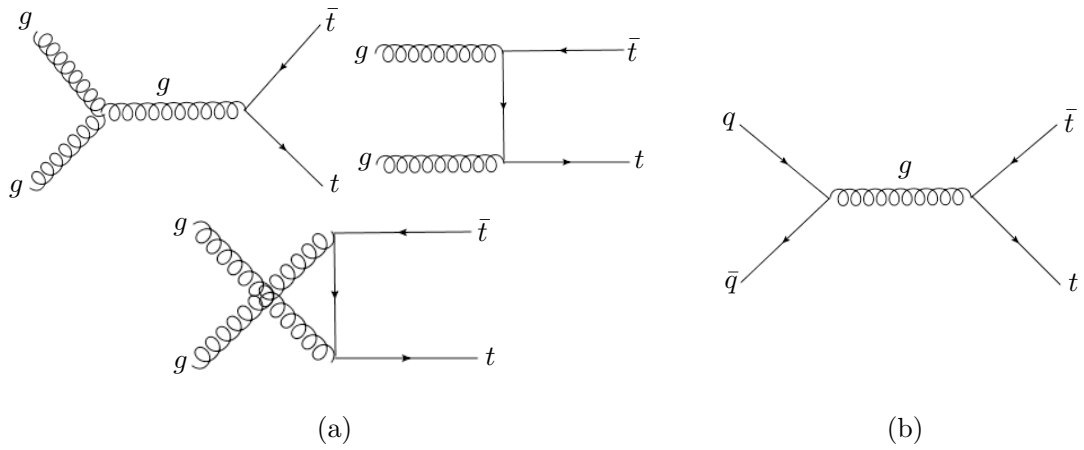
Figure 1.4: Production of $t\bar{t}$-pairs via gluon-gluon scattering (a) and quark-quark scattering (b). Processes are shown at lowest order.
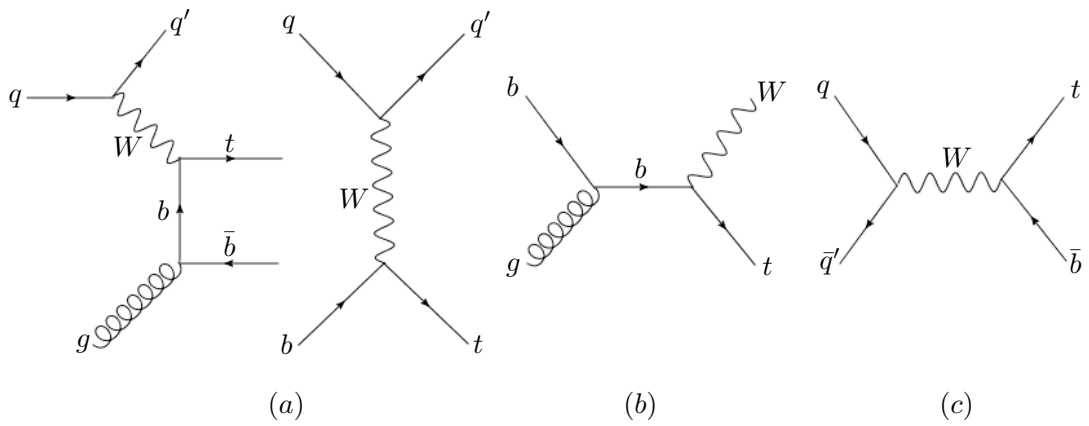
Figure 1.5: The tree level processes contributing to the production of single top quarks: (a) t-channel, (b) Wt associated production, (c) s-channel.

boson decays approximately $\frac{1}{3}$ of the time into a lepton-neutrino pair (leptonic decay) and $\frac{2}{3}$ of the time into a quark pair (hadronic decay) [9].

By classifying the $t\bar{t}$ decays according to the decays of the W bosons three channels are defined:

- **Fully hadronic channel**: both W bosons decay to quark pairs. The fully hadronic channel results from approximately $\frac{4}{9}$ of $t\bar{t}$ decays. The channel has a signature of a number of high p_T jets: two b jets from the decay of the top quarks and four light jets from the decay of the W bosons. The signal for this channel is difficult to distinguish from QCD multijet production that is abundant at hadron colliders.

- **Semileptonic channel**: one W boson decays to a quark pair and the other to a lepton-neutrino pair. The semileptonic channel results from approximately $\frac{4}{9}$ of $t\bar{t}$ decays. The channel has a signature of high p_T jets, missing transverse energy in the detector ($E_\mathrm{T}^{\mathrm{miss}}$) from the neutrinos escaping detection, and a lepton. The presence of the single lepton allows suppression of backgrounds from QCD multijet processes.

- **Dilepton channel**: both W bosons decay to lepton-neutrino pairs. The dilepton channel (also known as fully leptonic) results from approximately $\frac{1}{9}$ of $t\bar{t}$ events. The channel has a signature of least 2 high p_T b-jets, $E_\mathrm{T}^{\mathrm{miss}}$ from the neutrinos, and leptons. Since two neutrinos escape detection this channel cannot be fully reconstructed.

The top quark will be very important in the early data taking phase at the LHC. The first measurements of the top quark mass will provide feedback on the performance of the detector and will allow calibration of the jet energy scale and the tagging of b-jets [12]. Precise measurements of the top quark mass will also provide consistency tests of the SM and allow to constrain the Higgs boson mass. The measurements of the properties of the top quark will need to be understood before any discoveries of new physics can be claimed.

1.1.4 Limitations of the Standard Model

Despite its success, the SM has a number of limitations. Its main limitation is that it does not incorporate the gravitational interaction which inhibits it from describing interactions at arbitrarily high energies. At present the SM ignores all gravitational effects. This is a valid approximation in the currently explored energy domains near the electroweak scale ($\mathcal{O}(100)$ GeV), but a new description will be required at the reduced Planck scale ($M_P = (8\pi G_{\text{Newton}})^{-1/2} = 2.4 \times 10^{18}$ GeV), where quantum gravitational effects can no longer be ignored [4].

(a)   (b)
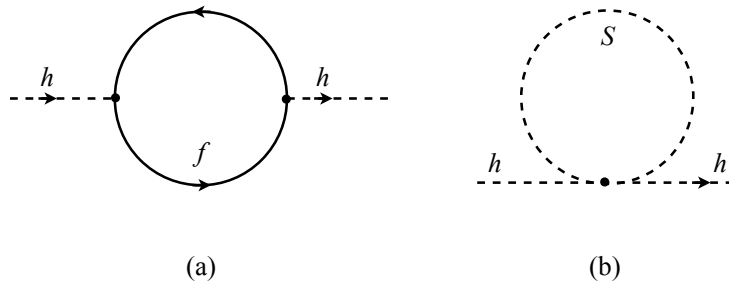
Figure 1.6: Quantum corrections to the Higgs boson mass from (a) fermions and (b) bosons.

There are doubts as to whether the SM is an effective theory that is able to describe physics up to the Planck scale. All dimensionless couplings and fermion masses are logarithmically sensitive to the scale Λ at which new physics becomes relevant. However, the square of scalar masses are quadratically sensitive to Λ and so the Higgs boson mass receives quadratically divergent radiative corrections on the order of Λ. For example, the coupling of the Higgs boson to a fermion f, with a mass m_f and coupling strength λ_f, as demonstrated in Figure 1.6(a), can result in corrections to the Higgs mass of the form:

$$m_H^2 = m_0^2 + \Delta m_H^2 \tag{1.6}$$

where

$$\Delta m_H^2 = \frac{|\lambda_f|^2}{16\pi^2}[-2\Lambda^2 + 6m_f^2 \ln(\Lambda/m_f) + ...]. \qquad (1.7)$$

m_0 is the bare Higgs mass; the mass of the Higgs neglecting quantum corrections due to virtual particle loops, m_H^2 is the observed Higgs mass [4]. Electroweak precision measurements [13] and unitarity constraints [14] indicate that the Higgs mass should be observed to be near the electroweak scale ($\mathcal{O}(100$ GeV$)$). Therefore, if the scale of new physics Λ is much larger than the electroweak scale, for example $\Lambda \sim M_P$, very precise cancellations must occur to remove the quadratic dependence of the Higgs mass on this high energy scale and leave the Higgs with a mass on the order of the electroweak scale. It is therefore expected that new physics will appear at scales just above the electroweak scale, stabilising the hierarchy between the electroweak scale and the Planck scale in a more natural way.
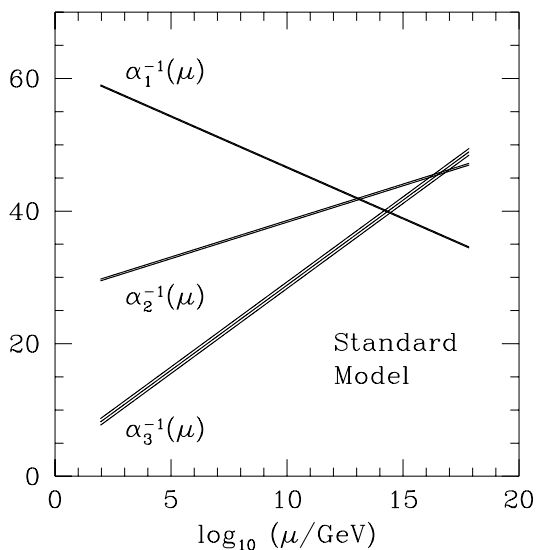
Figure 1.7: The running of the SU(3), SU(2) and U(1) gauge couplings according to one loop renormalization group equations. The bands reflect contemporary experimental uncertainties. Taken from Ref. [15].

Another limitation of the SM is that it does not yet allow the unification of the

electroweak and strong interactions. The running of the electroweak and strong coupling constants hints that a unification at higher energies could be possible, but extrapolating the currently measured values the coupling constants approach each other but do not meet at the same energy [15] as shown in Figure 1.7. This suggests that the SM could be part of a more fundamental theory, a so-called "Grand Unified Theory" (GUT), where a higher symmetry group unifies the electroweak and strong interactions at a higher energy known as the GUT scale (M_{GUT}) and is broken at lower energies into the known SM SU(3)×SU(2)$_L$×U(1)$_Y$ symmetry group.

The SM also does not provide a candidate for the cold dark matter which is believed to make up almost a quarter of the energy density of the universe [9].

1.1.5 Supersymmetry

The limitations of the SM lead particle physicists to believe that it is merely a small part of a more fundamental theory. One of the most popular proposed extensions of the SM is Supersymmetry (SUSY). SUSY is based on the idea that a symmetry exists between bosons and fermions. A supersymmetric transformation changes the spin of a single-particle state by $\pm\frac{1}{2}$ transforming fermionic states into bosonic states and vice versa [4]:

$$Q|\mathrm{Fermion}\rangle = |\mathrm{Boson}\rangle; \quad Q|\mathrm{Boson}\rangle = |\mathrm{Fermion}\rangle \tag{1.8}$$

The consequence of this is that for every fermion there exists a bosonic superpartner and for every boson their exists a fermionic superpartner. This provides a solution to the SM hierarchy problem which can be seen by considering the quantum corrections resulting from scalar particles, as demonstrated in Figure 1.6(b) [4]:

$$\Delta m_H^2 = \frac{\lambda_S}{16\pi^2}[\Lambda^2 - 2m_S^2 \ln(\Lambda/m_S) + ...]. \tag{1.9}$$

If the fermions of the SM are accompanied by two complex scalar superpartners with $\lambda_S = |\lambda_f|^2$, then the relative minus sign between these scalar loops and the

fermion loops demonstrated in Equations 1.7 and 1.9 allows a natural cancellation of the quadratic divergences.

If SUSY were an exact symmetry of nature then the SM particles and their superpartners would be degenerate in mass but the superpartners have not yet been observed in any particle physics experiment to date, therefore SUSY must be a broken symmetry with the superpartners having higher mass than their SM partners. Thus SUSY predicts the existence of a new spectrum of particles at higher energies. The presence of these particles affects the running of the gauge couplings, and can allow unification. An example of successful unification is demonstrated in the minimal supersymmetric extension of the SM (discussed in Section 1.1.6), in which supersymmetric masses lie below a few TeV. In the MSSM, unification occurs at a scale of $\sim 10^{16}$ GeV [4] as demonstrated in Figure 1.8.
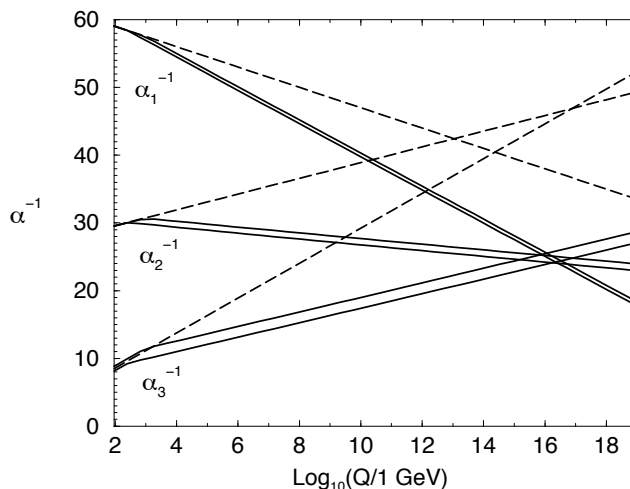
Figure 1.8: The evolution of the inverse gauge couplings in the Standard Model (dashed lines) and an MSSM SUSY model (solid lines). Taken from Ref. [4].

SUSY particles and SM particles are distinguished by a multiplicative quantum number known as R-parity, related to the baryon number B, lepton number L

13

and spin S of a particle as follows [4]:

$$R \equiv (-1)^{3(B-L)+2S}. \tag{1.10}$$

As a result, all SM particles have R-parity +1 and all supersymmetric particles have R-parity -1. Requiring that R-parity be conserved results in two consequences: supersymmetric particles are always produced in pairs and the lightest supersymmetric particle (LSP) cannot decay. The LSP provides a potential candidate for cold dark matter [9].

1.1.6 The Minimal Supersymmetric Standard Model (MSSM)

The Minimal Supersymmetric Standard Model (MSSM) is a supersymmetric extension to the SM, which introduces the minimum particle content necessary to give rise to all of the SM particles and their SUSY partners [5]. It is most convenient to describe the MSSM in terms of the gauge eigenstates in which the particles can be treated as massless. Table 1.2 provides an overview of the particle content.

The SM fermions have two chiral degrees of freedom; they each have left-handed and right-handed components (except the neutrinos which only have a left-handed component). Therefore the MSSM includes two scalar particles for each SM fermion, one for each chiral degree of freedom [4]. Each scalar particle and the corresponding chiral component of the SM fermion are known as superpartners and form chiral supermultiplets. The names of the new scalar superpartners to the fermions are formed by taking the fermion name with a preceeding "s" and the particles are known in symbol form by placing a tilde over the corresponding particle. For example, the superpartner of the left-handed electron e_L is denoted $\tilde{e}_L$ and is known as a selectron. Although the scalar superpartners of the SM fermions are given labels corresponding to left-handed and right-handed they have no handedness themselves since they are spin-0 particles, the label merely denotes which chiral component of the fermion they are associated with.

The massless SU(2)×U(1) gauge bosons of the SM form gauge supermultiplets with their fermionic superpartners [4]. The names of the fermionic partners are formed by taking the gauge boson name and appending it with "ino", for example, the superpartner of the gluon g is the gluino denoted $\tilde{g}$.

The Higgs sector is extended with respect to the SM; two complex Higgs doublets are required to guarantee cancellation of anomalies from the introduction of the Higgs superpartners, known as higgsinos, and to generate mass for both "up"-type and "down"-type quarks. Together the two Higgs doublets and their conjugates have eight internal degrees of freedom. Three of these are used to give mass to the Z and $W^{\pm}$ gauge bosons. The other five degrees of freedom produce massive Higgs bosons consisting of neutral CP-even scalars (h^0 and H^0), a neutral CP-odd scalar (A^0) and two charged scalars (H^+ and H^-) [4].

Chiral Supermultiplets	Spin 0	Spin $\frac{1}{2}$	$SU(3)_C$	$SU(2)_L$	$U(1)_Y$
Squarks, Quarks	$(\tilde{u}_L, \tilde{d}_L)$	(u_L, d_L)	$\mathbf{3}$	$\mathbf{2}$	$\frac{1}{3}$
	$\tilde{u}_R$	u_R	$\bar{\mathbf{3}}$	$\mathbf{1}$	$-\frac{4}{3}$
	$\tilde{d}_R$	d_R	$\bar{\mathbf{3}}$	$\mathbf{1}$	$\frac{2}{3}$
Sleptons, Leptons	$(\tilde{\nu}_L, \tilde{e}_L)$	(ν_L, e_L)	$\mathbf{1}$	$\mathbf{2}$	-1
	$\tilde{e}_R$	e_R	$\mathbf{1}$	$\mathbf{1}$	2
Higgs, Higgsinos	(H_d^0, H_d^-)	$(\tilde{H}_d^0, \tilde{H}_d^-)$	$\mathbf{1}$	$\mathbf{2}$	-1
	(H_u^+, H_u^0)	$(\tilde{H}_u^+, \tilde{H}_u^0)$	$\mathbf{1}$	$\mathbf{2}$	1
Vector Supermultiplets	Spin $\frac{1}{2}$	Spin 1	$SU(3)_C$	$SU(2)_L$	$U(1)_Y$
Gluon, Gluino	g	$\tilde{g}$	$\mathbf{8}$	$\mathbf{1}$	0
Gauge, Gaugino	$W^{\pm}, W^0$	$\tilde{W}^{\pm}, \tilde{W}^0$	$\mathbf{1}$	$\mathbf{3}$	0
	B	$\tilde{B}$	$\mathbf{1}$	$\mathbf{1}$	0

Table 1.2: The particles of the MSSM and their SU(3)×SU(2)×U(1) quantum numbers. Only one generation of quarks and leptons is demonstrated. For each lepton, quark and Higgs supermultiplet, there exists a corresponding anti-particle multiplet [5].

The superparticle states described above correspond to the gauge eigenstates.

These eigenstates mix in linear combinations to form the physical mass eigenstates. The charged gauginos and higgsinos mix to form charginos ($\tilde{\chi}_1^{\pm}$, $\tilde{\chi}_2^{\pm}$). The neutral gauginos and higgsinos mix to form neutralinos ($\tilde{\chi}_1^0$, $\tilde{\chi}_2^0$, $\tilde{\chi}_3^0$, $\tilde{\chi}_4^0$). Mixing also occurs in the squark and slepton states, however, the effect is only significant for the third generation where the stop squark eigenstates ($\tilde{t}_L$, $\tilde{t}_R$) mix to form the mass eigenstates ($\tilde{t}_1$, $\tilde{t}_2$); the sbottom squark eigenstates ($\tilde{b}_L$, $\tilde{b}_R$) mix to form ($\tilde{b}_1$, $\tilde{b}_2$) and the stau eigenstates ($\tilde{\tau}_L$, $\tilde{\tau}_R$) mix to form the mass eigenstates ($\tilde{\tau}_1$, $\tilde{\tau}_2$) [5].

1.1.7 Supersymmetry Breaking

The SUSY breaking mechanism that leads to the SUSY particles having different masses to their SM partners is unknown. For SUSY to be a valid theory the mechanism must break SUSY such that its effects are hidden at low energies where they have been unseen thus far. It must also ensure that the quadratic divergences that were naturally cancelled by introducing SUSY are not reintroduced by attempts to break SUSY at low energy scales. This can be achieved through "soft" SUSY breaking. Soft SUSY breaking decouples the origin of the symmetry breaking from its phenomenological consequences with a Lagrangian of the form:

$$\mathcal{L}_{\mathrm{MSSM}} = \mathcal{L}_{\mathrm{SUSY}} + \mathcal{L}_{\mathrm{soft}} \tag{1.11}$$

where $\mathcal{L}_{\mathrm{SUSY}}$ preserves SUSY and $\mathcal{L}_{\mathrm{soft}}$ contains the terms that break SUSY [4]. The symmetry breaking is assumed to originate in a "hidden sector" at some higher energy scale consisting of particles that are neutral with respect to the Standard Model gauge group. The symmetry breaking is then communicated down to the "visible sector" by some mechanism, often involving mediation by particles that comprise an additional "messenger sector".

Unlike the SUSY preserving $\mathcal{L}_{\mathrm{SUSY}}$, $\mathcal{L}_{\mathrm{soft}}$ introduces 105 new parameters that were not present in the SM, including the masses of the MSSM fermions and scalars, phases and mixing angles [9]. Such a large number of parameters is not ideal, however, many of these parameters can be constrained since they imply flavour

mixing or CP violating processes of the types that are restricted by experimental results.

There are many proposed mechanisms for mediating the SUSY breaking between the hidden and visible sectors [9]. The main phenomenological features of models of supersymmetry arise from the choice of this mechanism, and the choice of the soft SUSY breaking terms. This thesis will concentrate on gravity-mediated models, in particular, minimal supergravity (mSUGRA).

1.1.8 Gravity Mediated Supersymmetry Breaking

Gravity mediated SUSY breaking models, also known as supergravity, provide a natural mechanism for communicating the symmetry breaking of the hidden sector to the visible MSSM. In these models the symmetry breaking is communicated via flavour-blind gravitation interactions [16]. Here the gravitino mass is of the order of the electroweak symmetry breaking scale, whilst its couplings are approximately gravitational in strength. Assuming that the couplings of all gauginos and scalars to the hidden sector are equal at M_{GUT} results in a minimal model of supergravity (mSUGRA). This model has just five free parameters [9]:

1. $m_{1/2}$: a universal gaugino mass at the GUT scale

2. m_0: a universal mass for all scalar particles at the GUT scale

3. A_0: a universal trilinear coupling

4. $\tan\beta$: the ratio of the vacuum expectation values of the two MSSM Higgs doublets

5. $\mathrm{sgn}(\mu)$: the sign of the higgsino mass parameter.

The parameters at the electroweak scale, such as the masses of the supersymmetric particles, can be calculated from these parameters using renormalization group equations (RGEs). Figure 1.9 shows an example of the running of the masses from the GUT scale to the electroweak scale.
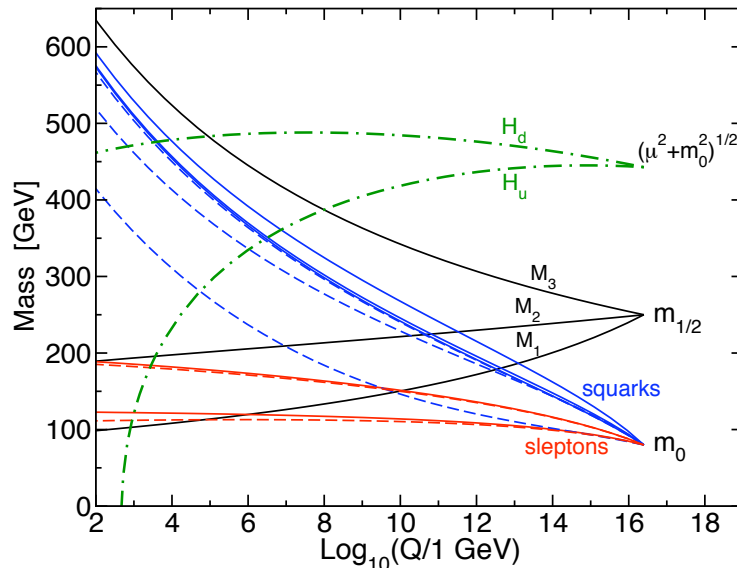
Figure 1.9: An example of the running of the soft-supersymmetry breaking parameters in the MSSM with energy scale Q. Taken from Ref. [4].

1.1.9 Experimental Constraints

Over the past few decades a number of searches for direct observations of super-symmetric particles have been performed. Thus far no direct evidence has been found to suggest SUSY is the correct description of the Universe, but the results from these experiments have placed constraints on current models, allowing physicists to rule out certain areas of the SUSY parameter space, narrowing the search for future experiments. The most notable searches are those carried out at the e^+e^- collider LEP and at the Tevatron $p\bar{p}$ collider. The following limits are at 95% confidence level for the MSSM with R-parity conservation.

At LEP, only the kinematic limit causes a phase space reduction that suppresses the production of SUSY particles, via electroweak interactions, compared to similar SM processes; a suppression that is stronger for scalar particles than for charginos. The results from LEP have enabled mass limits to be placed on SUSY particles, which when interpreted within a specific SUSY model, allow to constrain the parameter space of the model excluding the regions where the predicted

masses are outside these limits.

Figure 1.10 shows the LEP constraints for sleptons as a function of the lightest neutralino mass when the results from all four LEP experiments are combined. Smuon masses below 95-99 GeV, depending on the $\tilde{\chi}_1^0$ mass, are excluded provided the $m_{\tilde{\mu}_R} - m_{\tilde{\chi}_1^0}$ mass difference exceeds 5 GeV [9, 17]. Stau masses below 86-95 GeV, depending on the $\tilde{\chi}_1^0$ mass, are excluded as long as the stau-$\tilde{\chi}_1^0$ mass difference exceeds 7 GeV [9, 17]. The lower limit on the $\tilde{e}_R$ mass is 100 GeV for $m_{\tilde{\chi}_1^0} < 85$ GeV [9, 17].
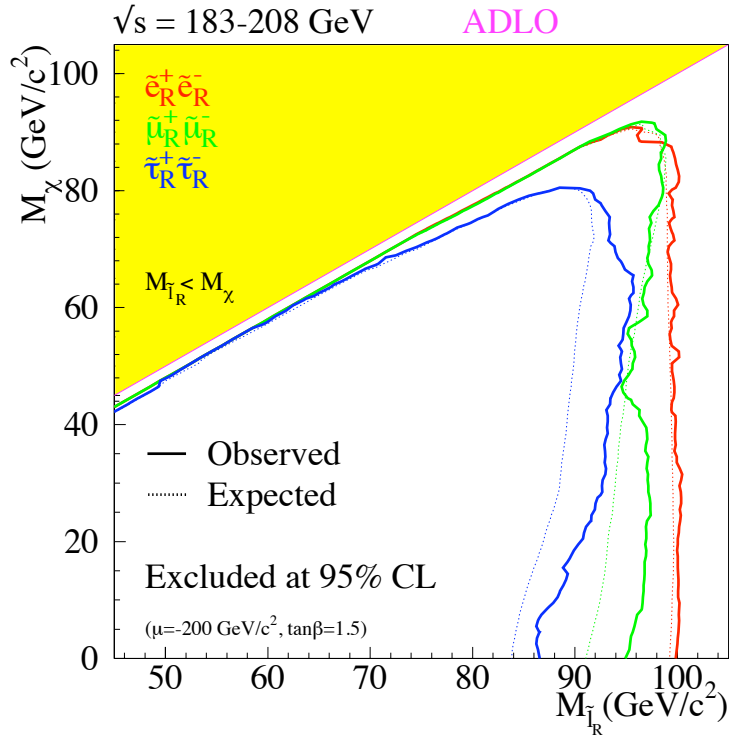

Figure 1.10: The combined lower limits from the LEP experiments in a constrained MSSM scenario for slepton masses as a function of the mass of the lightest slepton with $\mu = -200$ GeV and $\tan\beta = 1.5$. Taken from Ref. [17].

Chargino masses below 92 GeV are excluded by LEP assuming gaugino and sfermion mass unification [9, 18]. Figure 1.11 shows the lower mass limit for the

lightest neutralino as a function of $\tan\beta$, produced from the results of searches at LEP for charginos, sleptons and neutral Higgs bosons. A lower limit of 47 GeV, obtained at large $\tan\beta$, is placed on the mass [9, 19]. In a more constrained mSUGRA scenario, where μ is no longer a free parameter, a tighter limit of 50 GeV has been derived [9, 20].
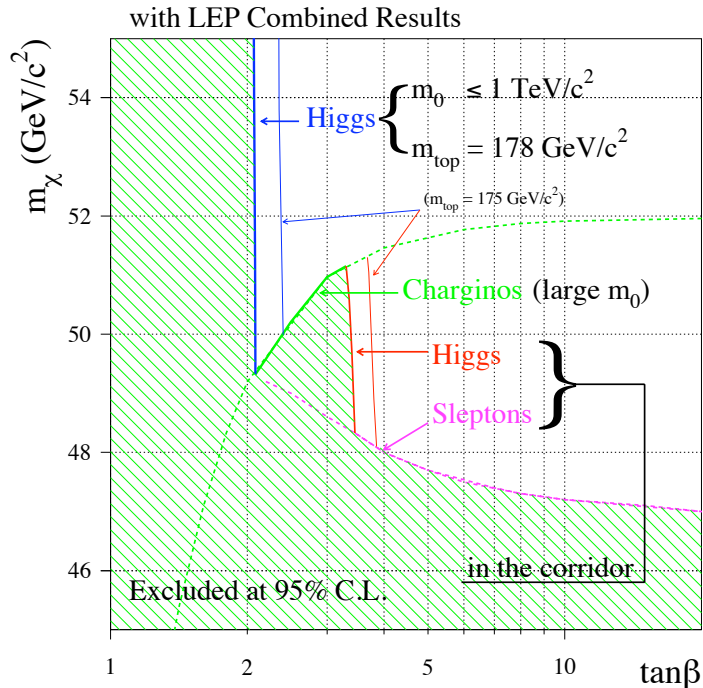
Figure 1.11: The lower mass limits of the lightest neutralino as a function of $\tan\beta$ using the combined results from chargino, slepton and Higgs boson searches from the four LEP experiments. A constrained MSSM model is assumed with negligible mixing in the stau sector. Taken from Ref. [19].

Due to the higher centre-of-mass energy at the Tevatron (1.98 TeV for Run II compared to 209 GeV at LEP) the mass reach of the Tevatron supersymmetry searches are expected to exceed those achieved at LEP. Mass limits placed on the squark and gluino masses by LEP have been extended by searches for squark/gluino production at the Tevatron. Figure 1.12 shows the region of the

$(m_0, m_{1/2})$ plane excluded by the CDF collaboration and by the the LEP experiments. Assuming an mSUGRA scenario with $A_0 = 0$, $\mu < 0$ and $\tan\beta = 5$, a mass limit of 392 GeV has been placed on the squark and gluino masses in the region of the parameter space where the squark and gluino masses are similar. For every squark mass a lower mass limit for the gluinos of 280 GeV has been set and for gluino masses up to 423 GeV squark masses below 378 GeV have been excluded [21]. Similar results were obtained by the D$\oslash$ collaboration [22].
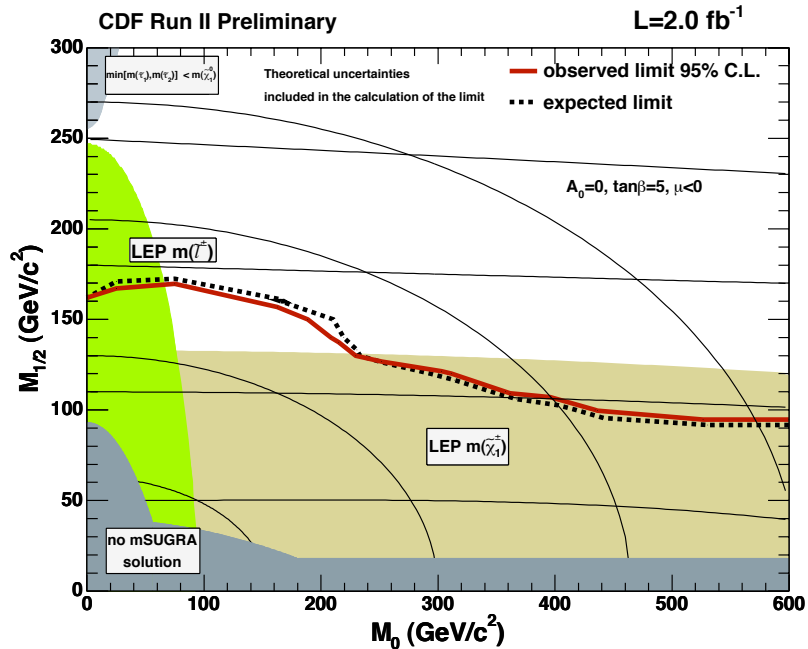
Figure 1.12: Region in the $(m_0, m_{1/2})$ plane excluded by CDF and the LEP experiments. Taken from Ref. [21].

A number of experiments whose main purpose is not to look for supersymmetry have lead to constraints on the SUSY parameter space. For example, the WMAP experiment [23, 24], which measures differences in the Cosmic Microwave Background Radiation across the sky, has lead to indirect constraints on the LSP. If the LSP is considered to be a candidate for dark matter it must conform to the prescriptions set by current cosmological measurements. The LSP must also be stable on cosmological timescales, it must interact very weakly, and must supply

the correct relic density. The recent data from the WMAP satellite confirm with greater accuracy that the current energy density of the Universe is comprised of $\sim 73\%$ dark energy and $\sim 27\%$ matter [9], most of which is non-baryonic dark matter. The data provides strong evidence for cold non-baryonic matter with a density of: $\Omega_{CDM}h^2 = 0.106 \pm 0.008$ [9] (where h is the Hubble constant). This constrains the mass of the LSP, which must be less than ~ 1 TeV for its relic density to fall within the correct range. Figure 1.13 shows the allowed regions of the constrained mSUGRA parameter space as a function of m_0 and $m_{1/2}$ for fixed values of A_0 and sgn(μ) and two different values of $\tan \beta$, taking into account a cold dark matter density consistent with the data from WMAP.

Measurements of rare decay processes can also be used to constrain the SUSY parameter space, for example, processes involving flavour-changing neutral currents (FCNCs). These processes have small branching fractions in the SM, but may get significant enhancements from supersymmetric processes. For example, the decays $B_s^0(B^0) \to \mu^+\mu^-$ only proceed at second order in weak interactions in the SM, but in the MSSM contributions from supersymmetric loops can increase the branching fraction by several orders of magnitude at large $\tan \beta$ with an enhancement proportional to $\tan^6 \beta$ [9]. The SM expectations for the branching fractions are $(3.42 \pm 0.54) \times 10^{-9}$ [9] and $(1.00 \pm 0.14) \times 10^{-10}$ [9] for B_s^0 and B^0 respectively. The most recent limits are $< 5.8 \times 10^{-8}$ and $< 1.0 \times 10^{-8}$ respectively [25]; just one order of magnitude above the predictions in the case of the B_s^0.

Precision measurements of the anomalous magnetic moment of the muon are also sensitive to supersymmetry [9].
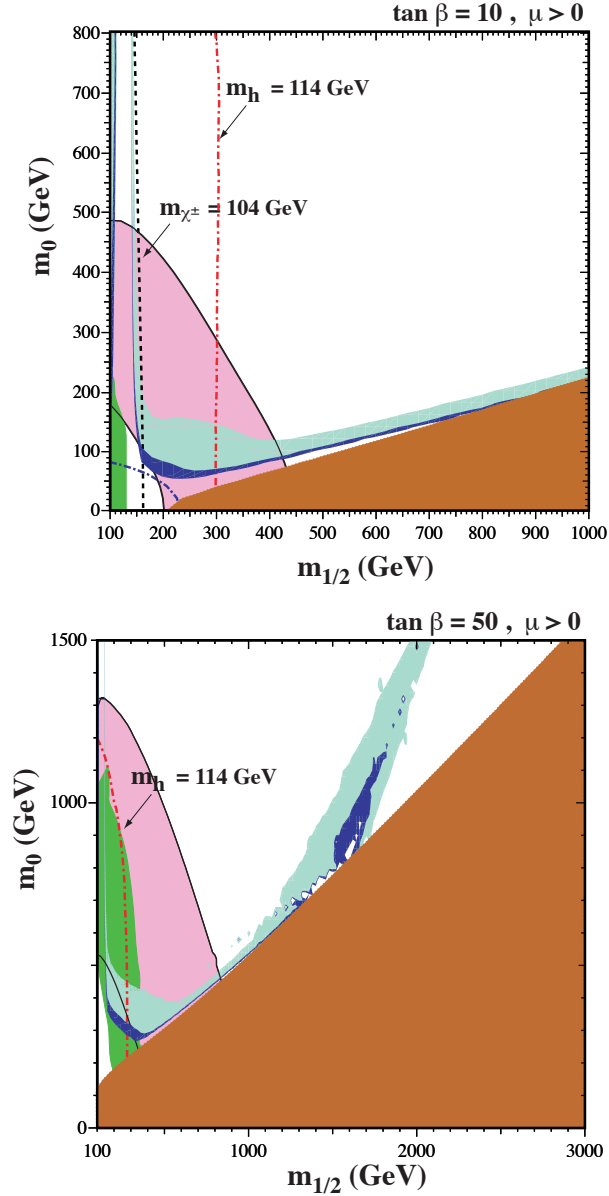
Figure 1.13: The regions excluded in the $(m_0, m_{1/2})$ parameter space for $A_0 = 0$, $\mu > 0$ and $\tan\beta = 10$ (left) or $\tan\beta = 50$ (right). The brown regions are those disallowed because $m_{\tilde{\tau}_1} < m_{\tilde{\chi}}$ and so the LSP is charged. In green are the regions excluded using precision measurements of $b \to s\gamma$. The pink regions are those favoured by measurements of the anomalous magnetic moment of the muon. The light blue regions are those consistent with pre-WMAP data. The dark blue regions are in agreement with the dark matter relic density measured by WMAP: $0.094 \leq \Omega_\chi h^2 \leq 0.129$. Also included are lines showing an MSSM Higgs boson mass of 114 GeV and a $\tilde{\chi}_1^{\pm}$ mass of 104 GeV. A dot-dashed line indicates the LEP constraint on the $\tilde{e}$ mass. Taken from Ref. [26].

Chapter 2

Phenomenology of Hadron Colliders

2.1 Partonic substructure

Hadrons are composite particles consisting of quarks and gluons. The quarks that give rise to the quantum numbers of the hadrons are known as valence quarks. In addition to these quarks, hadrons contain an indefinite number of virtual quarks, antiquarks and gluons. These virtual quarks are known as sea quarks and do not contribute to the quantum numbers of the hadrons [2]. Collectively the constituents are known as partons. Due to their composite nature, collisions between hadrons must therefore be considered as interactions between the partonic substructures.

Inside an accelerated hadron, the longitudinal momentum that a single parton carries is not precisely know. However, the transverse momentum of the partons is zero, therefore it is convenient to describe objects resulting from the collision of partons in terms of their transverse energy E_T and transverse momentum p_T.

The longitudinal momentum of a parton is described by a parton distribution function (PDF), which describes the probability density of finding a parton with a particular longitudinal momentum fraction x for a given momentum transfer Q^2 [2]. The PDFs are determined by global fits to data from various experiments.
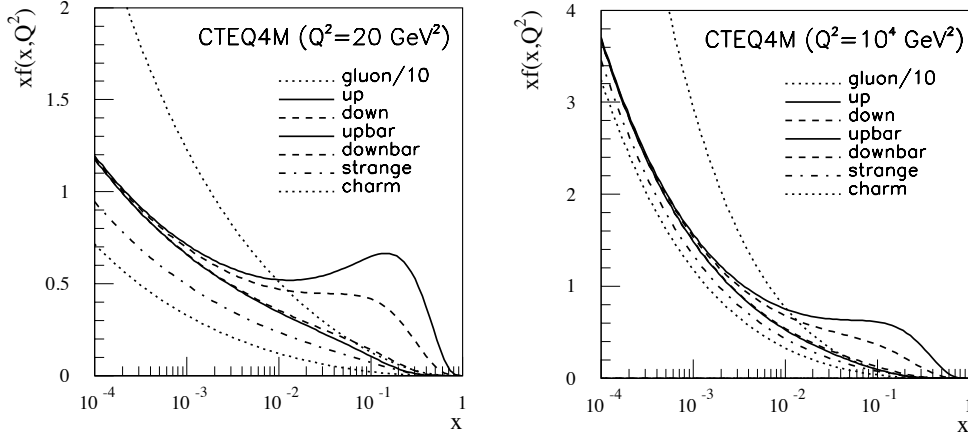
Figure 2.1: Parton distributions at $Q^2 = 20$ GeV^2 (left) and $Q^2 = 10^4$ GeV^2 (right) from the CTEQ group. The gluon distributions have been reduced by a factor of 10. Taken from Ref. [9].

.

Figure 2.1 shows the PDFs for the different quark flavours and the gluons as obtained by the CTEQ group [27] for $Q^2 = 20$ GeV^2 (left) and for $Q^2 = 10^4$ GeV^2 (right). For small values of Q^2 only the valence quarks are visible to the interaction and so the PDFs for these valence quarks peak at large values of x. At large values of Q^2, the fine structure of the protons is visible and so the sea quarks become involved in the interaction, thus the PDFs are shifted to smaller values of x [28]. The majority of interactions at hadron colliders are characterized by small momentum transfer [29]. These are known as soft interactions. The more interesting physics events are characterized by high momentum transfer, known as hard scattering events. Hard scattering events result in final state particles with high p_T.

In hard scattering interactions at a hadron collider, the centre-of-mass energy of the interaction ($\sqrt{\hat{s}}$) is reduced compared to the specified centre-of-mass energy of the collider ($\sqrt{s}$), due to the colliding partons taking only a fraction of the total momentum of the hadrons. The centre-of-mass energy of the interaction is

given by:

$$\sqrt{\hat{s}} = \sqrt{x_a x_b s} \tag{2.1}$$

where x_a and x_b are the fractions of momentum carried by the colliding partons a and b respectively.

2.2 Cross-section

The likelihood of a particular physics process occurring is indicated by the cross-section σ for that process. Cross-sections are usually measured in units of barn (1 b $= 10^{-24}$ cm^2).

Consider the generic process:

$$h_a h_b \rightarrow V + X \tag{2.2}$$

where h_a and h_b are the colliding hadrons, V denotes e.g. vector bosons and X denotes hadronic debris after the collision. The cross-section for this process is given by:

$$\sigma(h_a h_b \rightarrow V + X) = \sum_{a,b} \int dx_a \int dx_b f_a(x_a, Q^2) f_b(x_b, Q^2) \sigma_{ab}(p_a p_b \rightarrow V) \tag{2.3}$$

where $f_a(x_a, Q^2)$ and $f_b(x_b, Q^2)$ are the parton distribution functions for two interacting partons and σ_{ab} is the partonic cross-section [11]. The indicies a,b denote the parton flavours (g, u, $\bar{u}$, d, $\bar{d}$, ...). Figure 2.2 shows a possible schematic of the process given in Equation 2.2.

The partonic cross-section is given by:

$$d\sigma_{ab}(a + b \rightarrow V) = \frac{1}{2\hat{s}} \frac{1}{(2\pi)^2} \int \frac{d^3 p_V}{2E_V} \delta^4(p_a + p_b - p_V).F_{\text{colour}}.F_{\text{spin}} \sum_{\text{spin, colour}} |\mathcal{M}|^2 \tag{2.4}$$
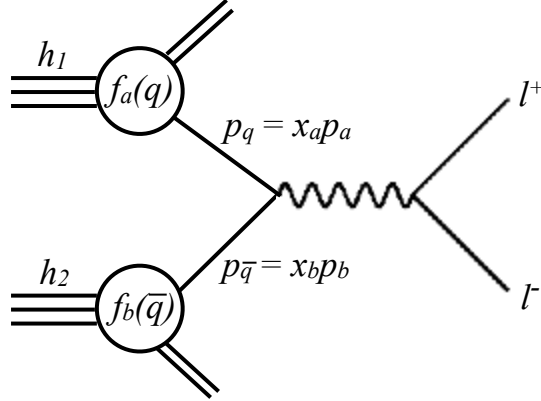
26

Figure 2.2: Schematic of a *pp*-collision in which two leptons are produced from the interaction of the partons.

where $\hat{s}$ is the centre-of-mass energy, F_{colour} and F_{spin} are factors which result from averaging over the colour and spin states and $|\mathcal{M}|$ is the matrix element which relates the initial and the final states of the interaction.

The partonic cross-section is calculated using perturbation theory. The leading order (LO) calculation may suffer from large uncertainties. In order to get the full cross-section higher order contributions from virtual corrections e.g. emission and absorption of gluons, must be taken into account. Examples of next-to-leading order (NLO) contributions, are demonstrated in Figure 2.3. These higher order terms can lead to considerable corrections to the total cross-section. For most processes at hadron colliders NLO cross-sections are available.

2.3 The Final State

There are a number of processes that contribute to the final state topology at hadron colliders besides the hard scattering event:
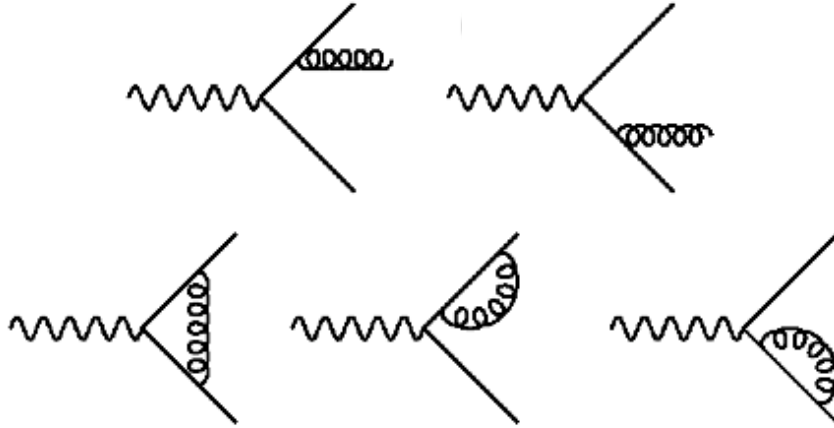
Figure 2.3: Example next-to-leading order (NLO) contributions.

- **Hadronisation**: Single quarks and gluons are never seen in the detector. Due to a property known as colour confinement they will always undergo a process known as hadronisation in which jets of colourless hadrons and mesons are produced.

- **Initial and Final State Radiation**: Coloured or electrically charged particles in the initial and final state can emit additional particles, known as initial state radiation (ISR) and final state radiation (FSR) respectively.

- **Beam remnants**: The partons involved in the hard scattering process carry only a fraction of the momentum of the initial hadron, the rest is carried by the so-called hadron remnant. Since this remnant is not colour neutral it must undergo hadronisation leading to additional particles in the final state.

- **Minimum bias events**: Most of the events that occur in hadron colliders are soft inelastic interactions. Multiple interactions of this type can occur per bunch crossing. Such events are called minimum bias events.

Processes that occur in addition to the hard scattering are known as the underlying event.

At high luminosity it is possible that more than one hadron will undergo an interaction contaminating the signal from the hard-scattering process of interest. This is called pile up.

2.4 Luminosity

The rate R at which a particular process occurs at a hadron collider is given by:

$$R = \frac{dN}{dt} = \sigma L$$

where L is the instantaneous luminosity of the hadron collider given by:

$$L = f \frac{n_a n_b}{4\pi \sigma_x \sigma_y}. \tag{2.6}$$

n_a and n_b are the number of hadrons in bunches colliding with a frequency f [9]. The denominator represents the effective interaction area. The total number of events N observed during some time period is obtained via integration of the rate R over the time period:

$$N = \sigma \int L dt. \tag{2.7}$$

The quantity $\mathcal{L} = \int L dt$ is known as the integrated luminosity and is used to quantify the amount of data collected over a given period of time at hadron colliders.

Chapter 3

The LHC and the ATLAS Experiment

This chapter provides a brief introduction to the Large Hadron Collider and the ATLAS detector. For further details of the specifications and design performance of the LHC and the ATLAS detector see Ref. [30] and Ref. [31, 32] respectively.

3.1   The Large Hadron Collider

The Large Hadron Collider (LHC) is the world's largest particle accelerator spanning a circumference of 27 km. It is situated approximately 100 m underground at CERN near Geneva, Switzerland. The LHC is designed to accelerate and collide beams of protons at unprecedented centre of mass energies up to 14 TeV. The main LHC ring is fed with a proton beam accelerated in stages by a chain of smaller accelerators. The protons are produced in a 50 MeV linear accelerator (LINAC 2), they are then fed into the Proton Synchrotron Booster (PSB) where they are accelerated to 1.4 GeV. Following this they are injected into the Proton Synchrotron (PS) where they are accelerated to 26 GeV. The protons are then injected into the Super Proton Synchrotron (SPS) where they are accelerated to 450 GeV before finally being injected into the main LHC ring where the beams are accelerated, focussed and eventually brought to collision at four points around the ring. Ultimately bunches containing 10^{11} protons will collide with a nominal

energy of 14 TeV with a design luminosity of 10^{34} cm^{-2}s^{-1} and with bunch crossings 25 ns apart [31]. The energies and luminosities are higher than any previous collider experiment.

Positioned around the LHC ring at the four points where collisions will occur are the main LHC experiments: ATLAS, CMS, LHCb and ALICE. The ATLAS (A Toroidal LHC ApparatuS), and CMS (Compact Muon Solenoid) detectors are large multi-purpose detectors whilst LHCb (Large Hadron Collider beauty) will specialise in the physics of b-quarks and ALICE (A Large Ion Collider Experiment) will study heavy-ion physics.

3.2 The ATLAS detector

3.2.1 Overview

ATLAS is the world's largest particle detector with a length of 44 km, a height of 25 m, weighing approximately 7,000 tonnes [31]. Rather than focussing on a specific physical process, ATLAS is a multi-purpose detector designed to measure as wide a range of signals as possible. The reason ATLAS was built this way was to ensure that if there are new physics processes or new particles produced by the LHC collisions, whatever form these processes or particles take, ATLAS will be able to detect them and measure their properties. ATLAS is by no means the first multi-purpose detector but the unprecedented energy and extremely high collision rate of the LHC require ATLAS to be larger and more complex than any detector ever built.

The layout of the ATLAS detector is shown in Figure 3.1. The detector has a cylindrical design and consists of several sub-detector systems arranged radially around the interaction point. Closest to the interaction point is the Inner Detector surrounded by a 2 T solenoid magnet, used for tracking and precision measurement. The inner detector is surrounded by the electromagnetic and hadronic calorimeters, which will be used to accurately measure the energies of

particles, particularly jets of particles, and also the $E_{\mathrm{T}}^{\mathrm{miss}}$ performance of the detector. The calorimeter system is surrounded by the muon spectrometers and toroidal magnets, which will be used to identify muons and accurately measure their momenta. The muon system also forms an important part of the trigger system. The detector subsystems and the trigger system are briefly described in the next sections of this chapter.
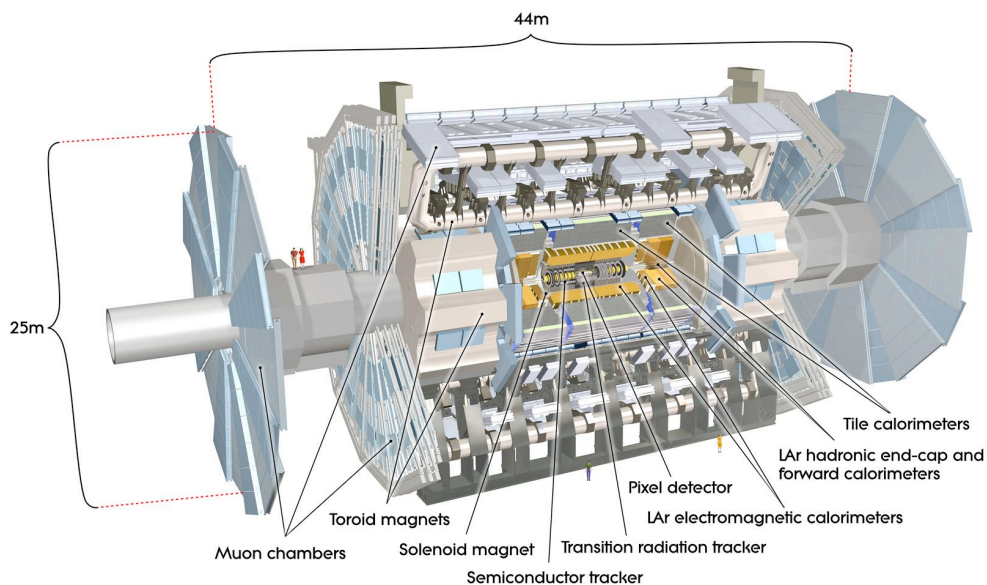

Figure 3.1: Schematic of the ATLAS detector. Taken from [33].

3.2.2 Coordinate System and Nomenclature

Figure 3.2 shows the coordinate system used to describe the ATLAS detector. It is a right-handed coordinate system with the x-axis pointing towards the centre of the LHC ring, the z-axis following the beam direction and the y-axis pointing upwards. Due to the curvature of the LHC tunnel, the y-axis is slightly tilted with respect to the vertical. The azimuthal angle ϕ is measured around the beam axis, and the polar angle θ is the angle from the beam axis. $\phi = 0$ corresponds to

the positive x-axis and ϕ increases clockwise looking in the positive z-direction. The direction of positive z is defined as detector side A, and negative as detector side C.
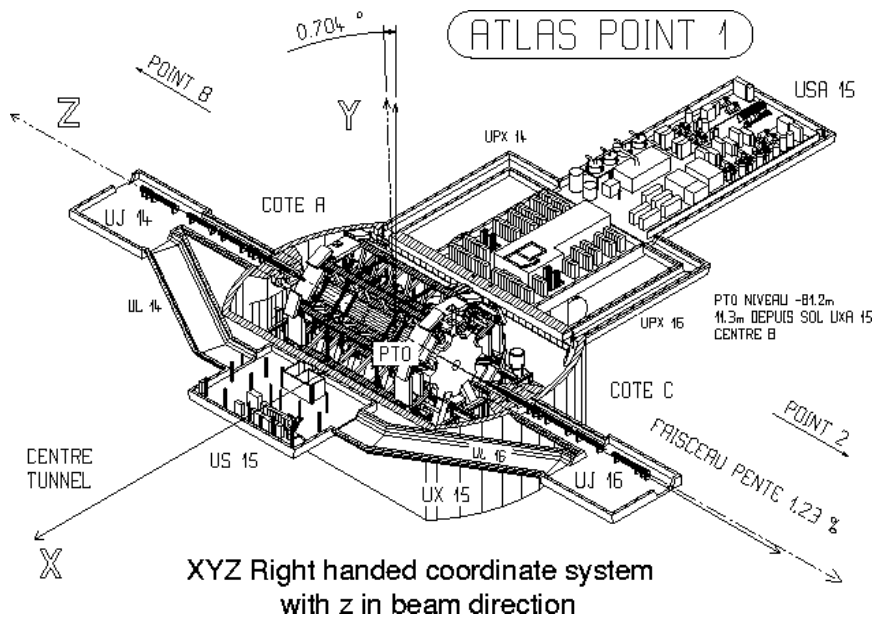

Figure 3.2: The coordinate system of the ATLAS detector. Taken from Ref. [34].

Inside the ATLAS detector particles are described in terms of the parameters (p_T, η, ϕ) where p_T is the transverse component of the particle's momentum i.e. the momentum perpendicular to the beam axis, ϕ is the azimuthal angle defined above and η is the pseudorapidity defined as:

$$\eta = -\ln\left[\tan\left(\frac{\theta}{2}\right)\right] \tag{3.1}$$

The pseudorapidity is 0 for particle tracks perpendicular to the beam pipe ($\theta = 90°$) and approaches ∞ as the track approaches the beam pipe ($\theta = 0°$). Separations between particles in the $\eta - \phi$ plane are described in terms of ΔR defined

as:

$$\Delta R = \sqrt{\Delta \eta^2 + \Delta \phi^2} \tag{3.2}$$

Some particles, such as neutrinos, have a vanishingly small probability of interacting with the materials of the detector. Their presence can be inferred from the apparent non-conservation of momentum of the particles that are observed.

3.2.3 The Magnet System

The ATLAS detector uses two large superconducting magnet systems to bend the tracks of charged particles so that their momenta can be measured. Figure 3.3 shows the layout of the magnet systems inside the ATLAS detector. The first system is a central solenoid (CS) providing a magnetic field for the Inner Detector. The CS has a length of 5.8 m, an inner diameter of 2.46m and an outer diameter of 2.56 m. It provides a central field of 2 T with a peak magnetic field of 2.6 T at the superconductor itself. It is positioned in front of the barrel electromagnetic calorimeter.

The second system is the toroid magnet system, which consists of a 25.3 m long barrel toroid (BT) with an inner and outer radius of 9.4 m and 20.1 m respectively, and two end-caps toroids (ECT) with lengths 5.0 m and inner radii of 1.65 m and outer radii of 10.7 m, at each end of the barrel. Each of the three toroids consists of 8 flat coils assembled radially and symmetrically around the beam axis. The ECTs are rotated by 22.5° with respect to the BT in order to provide radial overlap and to optimise the bending power in the interface regions of both coil systems. Both the BT and the ECTs are situated outside the calorimeters and within the muon system.

3.2.4 The Inner Detector (ID)

The Inner Detector begins centimeters from the proton beam pipe, extends to a radius of 1.15 m and is 7 m in length along the beam pipe. It covers the angular
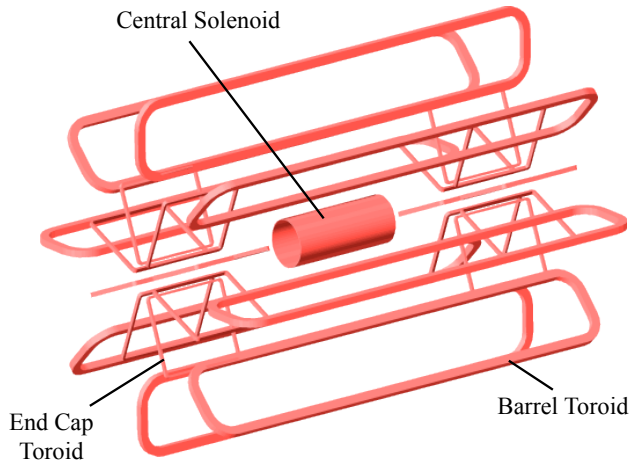
Figure 3.3: The magnet system of the ATLAS detector. Adapted from Ref. [33].

regions corresponding to $|\eta| < 2.5$. It is designed to provide hermetic and robust pattern recognition, excellent momentum resolution and both primary and secondary vertex measurements. It is also designed to provide electron identification in the region $|\eta| < 2.0$ for a wide range of energies (between 0.5 GeV and 150 GeV) pushing existing technology to its limit. This is achieved with the combination of three independent but complementary detector subsystems: discrete high-resolution semiconductor pixel and strip detectors in the inner part of the ID, and continuous straw-tube tracking detectors with transition radiation capability in its outer part. Figure 3.4 shows a cutaway view of the ID and its subsystems. Figures 3.5 and 3.6 show the subsystems and structural elements traversed by 10 GeV charged particles passing through the barrel and end-cap regions respectively.

The resolution of the inverse transverse momentum of a track in the ID is given by [35]:

$$\sigma(\frac{1}{p_T}) = (0.34 - 0.41 \text{ TeV}^{-1}) \left(1 \oplus \frac{(44 - 80 \text{ GeV})}{p_T} \right) \tag{3.3}$$

where the range represents the variation from lower values of $|\eta|$ to higher values.
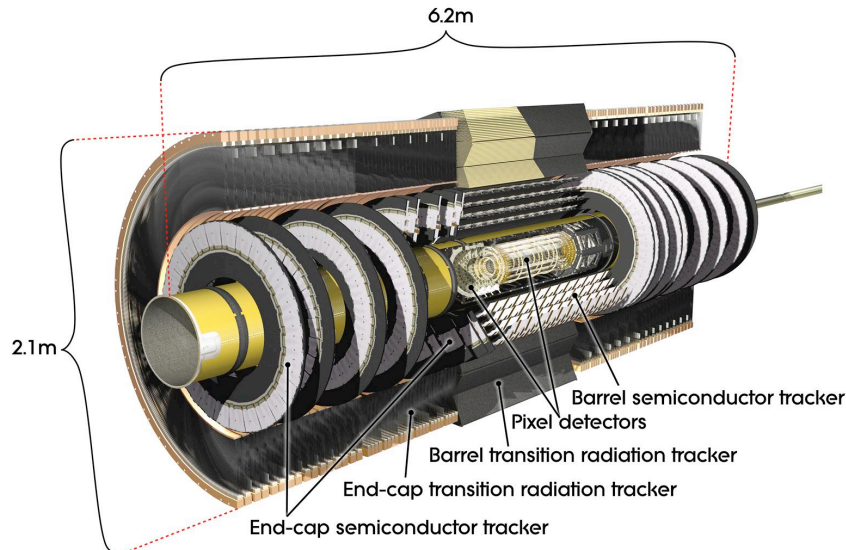
Figure 3.4: Cutaway view of the Inner Detector. Taken from [33].

The Pixel Detector

The pixel detector is designed to provide very high granularity, high precision measurements as close to the interaction point as possible. The system consists of 3 silicon barrel layers at average radii of ∼4 cm, 10 cm and 13 cm from the interaction point, and 5 disks on each side to complete the coverage with radii of 11 cm and 20 cm. Both the disk and barrel regions are instrumented with modular units of size 62.4 × 21.4 mm, where the long side of the module is positioned parallel to the beam in the barrel and radially in the disks.

The pixel detector lies closest to the interaction point where particle tracks are densest, therefore it must have a high density of active elements in order to achieve the low occupancy required for pattern recognition. The sensitive part of the module is a silicon wafer 250 μm thick, segmented into 46,080 pixels. Each of the pixels are 50 × 400 μm.

The system provides three precision measurements over the full acceptance. Each layer has a spatial resolution of 10 μm in $R\phi$ and 115 μm in z (R for the disks) [31].
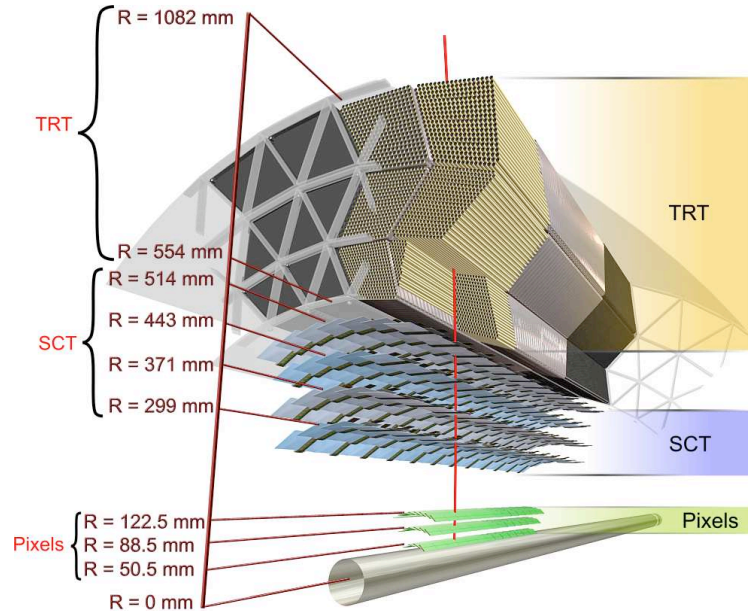
Figure 3.5: Schematic of the barrel ($\eta = 0.3$) of the Inner Detector showing the sensors and structural elements traversed by a charged track with $p_{\mathrm{T}} = 10$ GeV. Taken from Ref. [33].

The Semiconductor Tracker (SCT)

Surrounding the pixel detector is the SCT, designed to provide 8 precision measurements per track in the intermediate radial range. The SCT is designed to to provide high granularity measurements allowing good pattern recognition, as well as contributing to the measurement of momentum, impact parameter and vertex positions.

Like the pixel detector, the SCT uses silicon sensors to detect the passage of charged particles. Due to the increased distance from the interaction point and the larger area to be covered by the SCT compared to the pixel detector, silicon microstrips are used rather than modules made of silicon pixels. The microstrips are formed on silion wafers, with a strip pitch of 80 μm. The wafers are arranged onto modules. The barrel modules use 4 wafers of size 6.36×6.40 cm^2 combined into two layers where each layer is formed from two wafers wire-bonded together
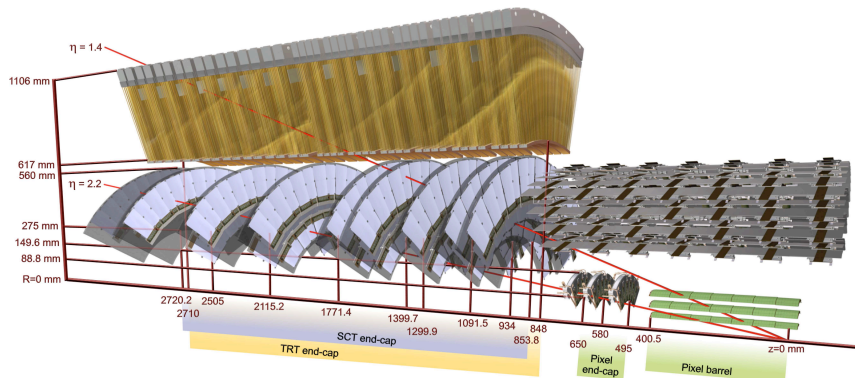
Figure 3.6: Schematic of the end-cap Inner Detector ($\eta = 1.4$ and 2.2) showing the sensors and structural elements traversed by two charged tracks with $p_\mathrm{T} = 10$ GeV. Taken from Ref. [31].

to give a combined sensor length of 12.8 cm. The end-cap modules are very similar but use tapered strips, with one set radially aligned. The strips are aligned on the modules to give precisions points in the $R\phi$ and z coordinates, using a small angle stereo to obtain the z measurement.

The barrel SCT uses eight layers of silicon microstrip detectors arranged coaxially on four barrels at radii of 30.0, 37.3, 44.7 and 52.0 cm. The end-cap SCTs are made of nine disk layers. In total, the SCT consists of 61 m^2 of silicon detectors, with 6.2 million readout channels. The spatial resolution is 17 μm in $R\phi$ and 580 μm in z (R for the disks) [31], per module containing one $R\phi$ measurement and one stereo measurement. Tracks can be distinguished if separated by more than $\sim$200 μm.

Transition Radiation Tracker (TRT)

The outer most layer of the Inner Detector is the TRT. The TRT is a system of straw detectors and forms the majority of the Inner Detector. It is designed to make a large number of measurements of the positions of charged particles and also to assist in the identification of these particles. Electron identification capability is added by employing xenon gas to detect transition-radiation photons

created in a radiator between the straws.

Each straw is a 4 mm diameter cylindrical tube with an inner surface coated in aluminium which acts as a high-voltage cathode. In the middle of the straw is a 31 μm gold-plated tungsten anode wire from which the signal is read out. The straws are filled with a xenon-based gas mixture such that a charged particle traversing the gas causes ionisation , which is detected on the wire. The cathodes are operated at -1530 V to give a gain of 2.5 $\times 10^4$. The drift-time provides a measure of the $R\phi$ position within the straw.

The gaps between the straws contain radiators consisting of polypropylene fibres in the barrel and foils in the end-caps, that facilitate the production of transition radiation. The TRT contains up to 73 layers of straws interleaved in the barrel and 160 straw planes in the end-caps. Each straw in the barrel is 144 cm long and is divided in two at the centre and read out at each end. In the end-caps the straws are 37 cm long and are arranged radially in wheels. In total there are approximately 351,000 electronic channels; each channel providing a drift-time measurement, with a spatial resolution of $\sim$ 130 μm, and two independent thresholds. The low threshold will detect the charge liberated by the passage of minimally ionising particles. The high threshold is designed to detect the transition radiation photons since low energy transition radiation photons are absorbed by the Xe gas mixture resulting in much larger signal amplitudes. The high threshold allows some discrimination between electrons and hadrons, with electrons producing more transition radiation than pions.

At least 36 straws will be traversed by charged tracks with $p_T > 0.5$ GeV and $|\eta| < 2.0$, except in the barrel-end-cap transition region ($0.8 < |\eta| < 1.0$), where this number decreases to a approximately 22 straws [31].

3.2.5   Calorimeter

The ATLAS calorimeters are designed to accurately measure the energy and direction of both charged and neutral particles such as electrons, jets and photons.

The calorimeter system is crucial to the measurement of the $E_{\mathrm{T}}^{\mathrm{miss}}$ in an event. It is also designed to allow separation of different types of particles for example separation of electrons and photons from hadrons and jets and separation of hadronic tau decays from jets. Like many general purpose detectors the ATLAS detector employs two calorimeter systems: an electromagnetic calorimeter (ECAL) and a hadronic calorimeter (HCAL). Typically hadronic showers penetrate more deeply than electromagnetic showers so the ECAL is optimised to measure the energy of electromagnetic showers, and the HCAL designed to measure hadronic showers. Figure 3.7 shows an overview of the ATLAS calorimeter system.
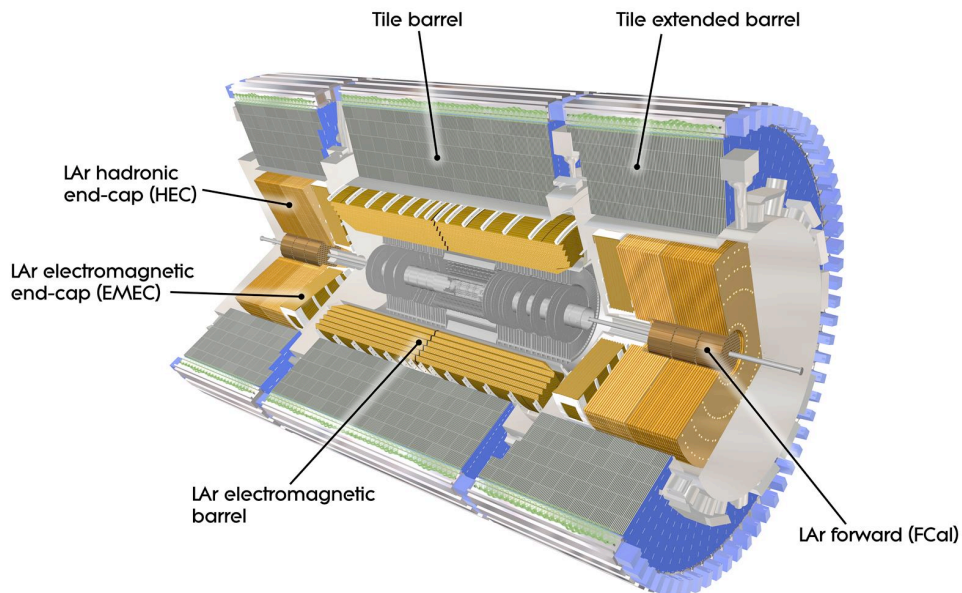

Figure 3.7: Overview of the ATLAS calorimeter systems. Taken from [33].

Electromagnetic Calorimeter (ECAL)

The ECAL is a lead liquid-argon (LAr) sampling detector. Liquid argon is used as the sampling material while lead plates are used to absorb energy. The absorbers and electrodes of the ECAL have accordion geometry, which provides complete ϕ symmetry without azimuthal cracks. The ECAL consists of a barrel region

($|\eta| < 1.475$) and two end-caps ($1.375 < |\eta| < 3.2$). The barrel calorimeter consists of two identical half-barrels of length 3.2 m with inner and outer diameters of 2.8 m and 4 m respectively, separated by a gap of 6 mm at $z = 0$. The end-cap calorimeters consist of two wheels, one on each side of the barrel. The wheels are 63 cm thick with external and internal radii of 2098 mm and 330 mm respectively. The wheels are mechanically divided into an outer wheel covering the region $1.375 < |\eta| < 2.5$ and an inner wheel covering the region $2.5 < |\eta| < 3.2$.

In the region $|\eta| < 1.8$ the ECAL is preceded by a presampler detector; a layer of liquid argon. This presampler is used to correct for the energy lost in the material of the Inner Detector, the cryostats and the coils, upstream of the calorimeter.

The central η region of the ECAL ($|\eta| < 2.5$) is devoted to precision measurements as the ECAL is matched to the Inner Detector in this region. Here the ECAL is segmented into three longitudinal sections. The first is the strip section which is finely granulated in η and acts as a 'preshower' detector. It has a constant thickness as a function of η of approximately 6 radiation lengths (X_0) including the upstream material. This section enhances particle identification making γ/π^0 and e/π separation possible, and it also provides a precise position measurement in η. The middle section is transversally segmented into square towers of size $\Delta\eta \times \Delta\phi = 0.025 \times 0.025$. This is the thickest part of the ECAL with total calorimeter thickness up to the end of this section approximately 24 X_0, tapered with increasing rapidity. The thickness of the back section varies between 2 X_0 and 12 X_0 and has a granularity of 0.05 in η.

The desired energy resolution for the ECAL is [32]:

$$\frac{\sigma(E)}{E} = \frac{10\%}{\sqrt{E(GeV)}} \oplus 0.7\%. \tag{3.4}$$

Test-beam measurements have shown that the ECAL meets these design performance goals well [31].

The Hadronic Calorimeter (HCAL)

The HCAL consists of barrel, end-cap and forward calorimeters, providing coverage out to $|\eta| = 4.9$. The total thickness of the HCAL is 11 interaction lengths (λ) at $\eta = 0$, including approximately 1.5 λ from the outer support. Both measurements and simulations have shown this to be sufficient to contain hadronic showers within the HCAL and reduce punch-through to the muon system. Together with the large η-coverage this enables good E_T^{miss} resolution.

The barrel calorimeters and two extended barrel calorimeters cover the regions $|\eta| < 1.0$ and $0.8 < |\eta| < 1.7$ respectively. These are sampling tile calorimeters using steel plates as the absorbing material interspersed with plastic scintillator tiles as the active medium. The tiles are placed radially and are staggered in depth. The tiles are 3 mm thick and the total thickness of the iron plates in one period is 14 mm. Radially the tile calorimeters extend from an inner radius of 2.28 m to an outer radius of 4.25 m. They are longitudinally segmented into three layers, approximately 1.4, 4.0 and 1.8 λ thick at $\eta = 0$. In the first two layers the granularity is $\Delta\eta \times \Delta\phi = 0.1 \times 0.1$ and in the last layer 0.2×0.1. In the gap region between the barrel and the extended barrel are special modules made of steel-scintillator sandwiches with the same sampling fraction as the rest of the tile calorimeter, which allow partial recovery of the energy lost in the crack regions of the detector. Where space in the gaps is limited thin scintillator counters are used.

The end-cap calorimeters are liquid argon calorimeters since high levels of radiation in the forward region would severely degrade the scintillator technology used in the barrel. Copper is used as the passive material. The end-cap calorimeters extend from $1.5 < |\eta| < 3.2$, overlapping with the barrel tile calorimeters and the forward calorimeters. This overlap is designed to reduce the drop in density in the gaps between the different sections. Each end-cap consists of two independent wheels of outer radius 2.03 m, each one built of 32 modules and two longitudinal segments, giving a total of four samplings. The granularity of the samplings is $\Delta\eta \times \Delta\phi = 0.1 \times 0.1$ for $1.5 < |\eta| < 2.5$ and 0.2×0.2 for $2.5 < |\eta| < 3.2$.

In the very forward region $3.1 < |\eta| < 4.9$, the forward calorimeter measures both hadronic and electromagnetic activity. As the forward calorimeter modules are located at high η, approximately 4.7 m from the interaction point, they are exposed to very high levels of radiation but the calorimeter provides clear benefits in terms of uniformity of coverage as well as reducing radiation background levels in the muon spectrometer. The forward LAr calorimeters are split into three 45 cm deep modules: one electromagnetic module and two hadronic modules. In the electromagnetic module copper is used as the passive material to optimise the resolution and the heat removal. In the hadronic modules tungsten is used to provide containment and minimise the lateral spread of hadronic showers. The granularity in each module is approximately $\Delta\eta \times \Delta\phi = 0.2 \times 0.2$.

The desired jet energy resolution of the hadronic calorimeter is [36]:

$$\frac{\sigma(E)}{E} = \frac{50\%}{\sqrt{E(GeV)}} \oplus 3\% \text{ for } |\eta| < 3$$
$$\frac{\sigma(E)}{E} = \frac{100\%}{\sqrt{E(GeV)}} \oplus 10\% \text{ for } 3 < |\eta| < 5$$

$$(3.5)$$

3.2.6   Muon Spectrometer

The muon spectrometer forms the outer part of the ATLAS detector. It has been designed to provide high-resolution momentum measurements of muons in the region $|\eta| < 2.7$ and stand-alone triggering capability in the region $|\eta| < 2.4$. Four different chamber technologies are employed by the muon spectrometer: Monitored Drift Tubes (MDTs), Cathode Strip Chambers (CSCs), Resistive Plate Chambers (RPCs) and Thin Gap Chambers (TGCs). The layout of these technologies within the muon spectrometer is shown in Figure 3.8. The chambers are arranged such that particles from the interaction point traverse three stations of chambers. The positions of the stations are optimised for full coverage and momentum resolution. The barrel chambers are arranged in three concentric cylinders at radii of 5, 7.5 and 10 m, covering $|\eta| < 1$. The end-cap chambers are arranged in four disks, concentric with the beam axis, at distances $|z| \approx 7.4$,

10.8, 14 and 21.5 m from the interaction point, covering $1 < |\eta| < 2.7$.

The performance goal of the muon spectrometer is a stand-alone transverse momentum resolution of approximately 10% for 1 TeV tracks [31].
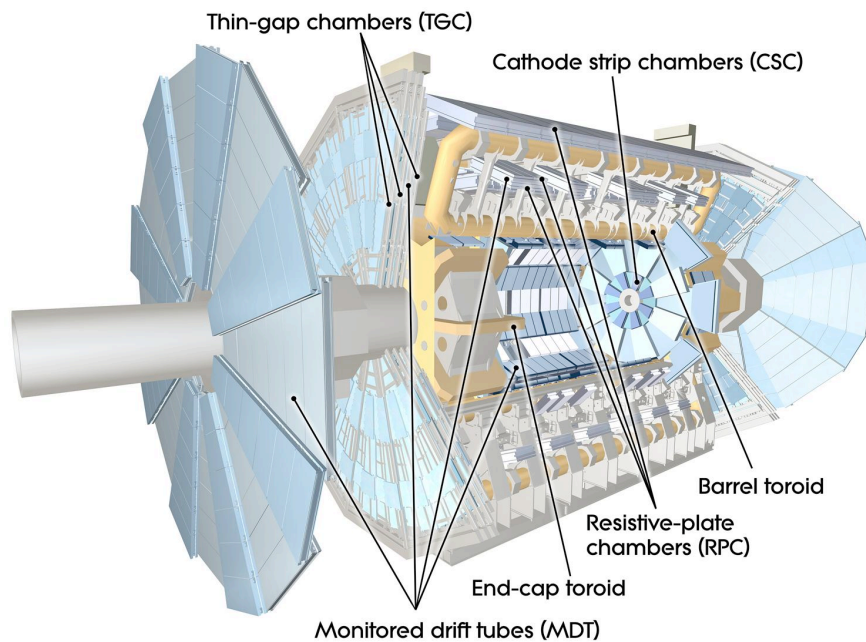

Figure 3.8: Overview of the ATLAS muon spectrometers. Taken from [33].

Monitored Drift-Tube Chambers (MDTs)

The MDTs provide precision measurements in the barrel and end-caps. Each drift tube is made from aluminium, filled with a non-flammable argon and carbon dioxide $(Ar(93\%)CO_2(7\%))$ mixture at 3 bar absolute pressure, with a 50 μm diameter tungsten-rhenium (WRe) wire running through the centre. The tubes are 30 mm in diameter with a wall thickness of 400 μm. The maximum drift time is $\sim$700 ns. The average resolution per tube is $\sim$80 μm [31]. Each MDT chamber consists of 2×4 or 2×3 monolayers of drift tubes, as demonstrated in Figure 3.9, in order to improve the resolution beyond the single-wire limit and to

achieve adequate redundancy for pattern recognition. An in-plane optical system is used to monitor any mechanical deformations in the chambers; hence the name 'monitored drift-tube chambers'.
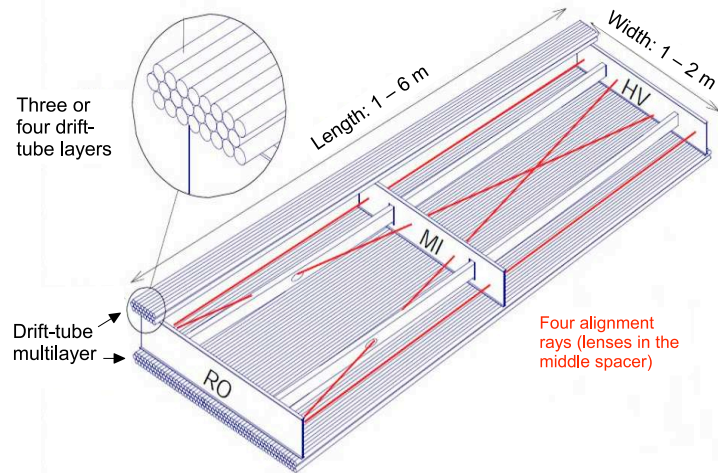
Figure 3.9: Mechanical structure of an MDT chamber as described in the text. Four optical alignment rays monitor the internal geometry of the chamber. Taken from Ref. [31].

Cathode Strip Chambers (CSCs)

In the first layer of the end-cap in the region $|\eta| > 2$ the limit for safe operation of the MDTs will be exceeded, thus in this region the MDTs are replaced with CSCs. The CSCs combine high spatial, time and double track resolution with high-rate capability and low neutron sensitivity. The CSCs are multi-wire proportional chambers with cathode strip readout. The anode wires are closely spaced and oriented in the radial direction. The cathodes are segmented. The precision coordinate is provided by a cathode with strips perpendicular to the wires and the transverse coordinate is provided by a cathode with strips parallel to the wires. The baseline gas is a non-flammable mixture of argon, carbon dioxide and carbon tetrafluoride ($Ar(30\%)CO_2(50\%)CF_4(20\%)$) with a total volume of 1.1 m^3. The small gas volume and the absence of hydrogen gives the CSCs

their low neutron sensitivity.

The CSCs system consists of two disks each with eight chambers (eight small chambers and eight large) as shown in Figure 3.10. Each chamber consists of four CSC planes resulting in four independent measurements in η and ϕ along each track. In the bending direction the CSC resolution reaches 60 μm per CSC plane, compared to the 80 μm resolution of an MDT tube layer. In the non-bending direction the resolution is 5 mm since the cathode segmentation is coarser. The CSCs have a small electron drift time of 30 ns and a good time resolution of 7 ns [31].
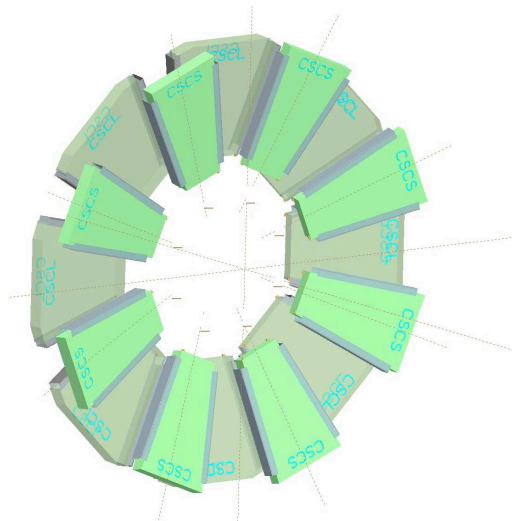
Figure 3.10: Schematic of the CSC end-cap with eight small and eight large chambers. Taken from [31].

Resistive Plate Chambers (RPCs)

The RPCs provide triggering in the barrel region. As shown in Figure 3.11, the trigger system in the barrel consists of three concentric cylindrical layers of RPC chambers around the beam axis. The three layers are referred to as the three trigger stations. Each station consists of two detector layers, each providing a measurement in η and ϕ. Therefore a track passing through all three stations will

have six measurements in η and ϕ.

The RPCs are gaseous parallel electrode-plate detectors consisting of a narrow gas gap formed by two parallel resistive bakelite plates with a thickness of 2 mm separated by insulating spacers also 2 mm thick. The spacers are placed at 10 cm intervals on both plates. The outside surfaces of the resistive plates are coated with thin layers of graphite paint, which are connected to the high voltage supply. A 7 mm wide polycarbonate frame is used to seal the gas gap at all four edges. The gap is filled with a gas mixture based on tetrafluoroethane ($C_2H_2F_4$) with a small admixture of sulphur hexaflouride (SF_6), which allows for a relatively low operating voltage. The primary ionisation electrons are multiplied into avalanches by a high, uniform electric field of typically 4.9 kV/mm. Amplification in avalanche mode produces pulses of typically 0.5 pC. Metal strips on both sides of the detector allow the signal to be read out via capacitive coupling. Each chamber consists of two detector layers and four readout strip panels. The RPCs have a typical space-time resolution of 1 cm $\times$ 1 ns.
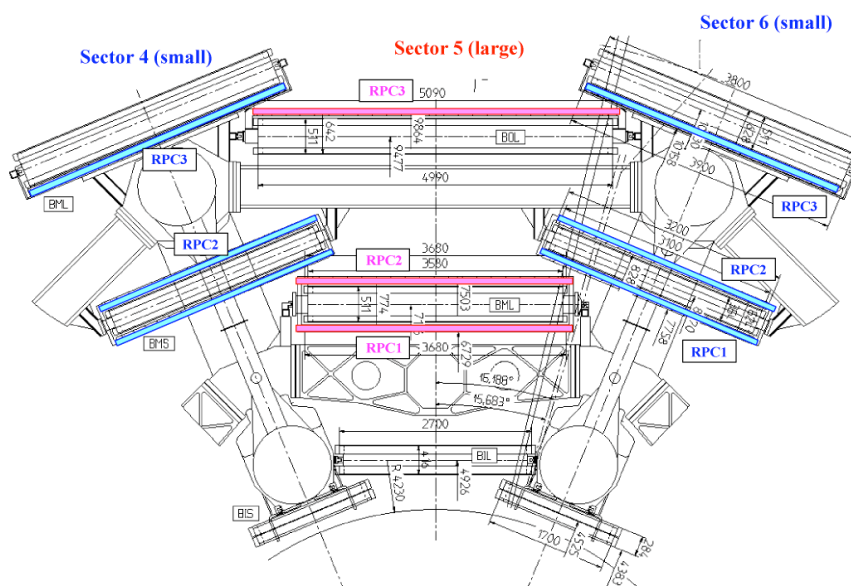
Figure 3.11: Cross-section through the upper part of the barrel with the RPC's marked in colour. All dimensions are in mm. Taken from Ref. [31].

Thin Gap Chambers (TGCs)

TGCs provide two functions in the end-caps: muon trigger capability and the determination of the second, azimuthal coordinate to complement the measurement of the MDTs in the radial direction. They are multiwire proportional chambers with the characteristic that the distance between the anode wire and the cathode (1.4 mm) is smaller than the distance between anode wires (1.8 mm). The anode wires, which are 50 μm in diameter, are arranged parallel to the MDT wires and provide the trigger information together with the readout strips, which are arranged orthogonal to the wires. The readout strips also provide the measurement of the second coordinate. The TGCs are operated with a highly quenching gas mixture of $CO_2(55\%)n\text{-}C_5H_{12}(45\%)$. The operating high voltage is forseen to be 3.1 kV. A trigger signal is formed by grouping several anode wires together and feeding them into a common readout. The number of wires per group depends on the desired granularity as a function of η and can be between 6 and 31.
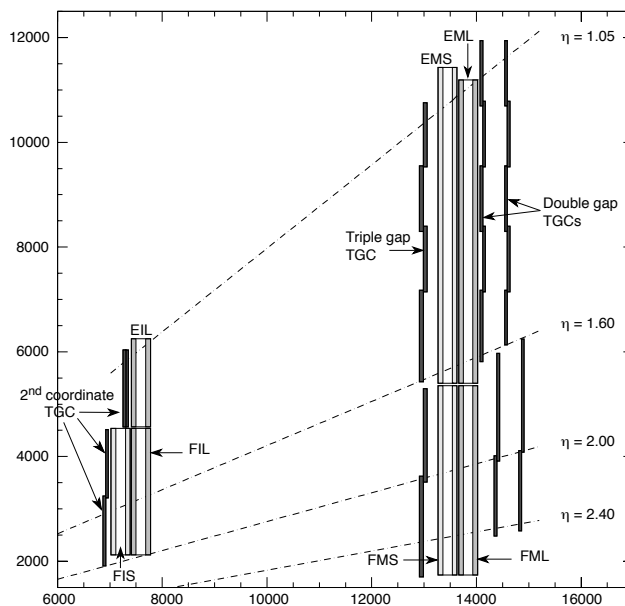
Figure 3.12: Longitudinal view of the TGC system. Dimensions are in mm. Taken from Ref. [34].
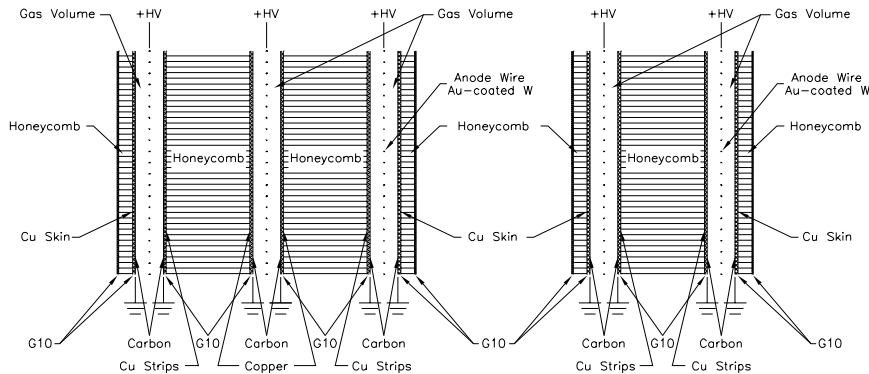
Figure 3.13: Schematic of the cross-section of a TGC triplet and doublet module. The dimensions of the gas gaps are enlarged with respect to the other elements. Taken from Ref. [31].

The TGCs are constructed in doublets and triplets of chambers. The inner station consists of one doublet and is used to measure the second coordinate, while the chamber layers in the middle station are arranged in one triplet and two doublets and provide the trigger and the second coordinate measurements. The arrangement of the doublets and triplets in the inner and middle stations is demonstrated in Figure 3.12. The arrangement of the wires and readout strips within these chambers is demonstrated in Figure 3.13.

The small wire distance and electric field configuration of the TGCs result in a short drift time and thus a good time resolution. Including the variation of the propagation time along wires and strips, signals arrive with 99% probability inside a time window of 25 ns [31].

3.3 The ATLAS Trigger System

At the design luminosity of 10^{34} cm^{-2} s^{-1} the ATLAS detector will experience an interaction rate of $\sim$1 GHz. The amount of data produced will be far too large to be feasibly stored and processed, therefore a trigger system is employed to identify the basic signatures of interesting physics events in order that such

events can be saved and the rest of the data can be discarded. The ATLAS trigger system aims to reduce the rate to around 200 Hz [31].

The ATLAS trigger system employs three successive levels of online event selection as demonstrated in Figure 3.14. The first level, known as Level-1 (L1), uses the trigger chambers of the muon spectrometer and coarse calorimeter information to reduce the event rate from 40 MHz to around 75 kHz (upgradable to 100 kHz). The latency of this stage is 2.5 μs. The L1 trigger is able to look for high p_T jets, leptons and photons as well as events with large missing transverse energy (E_T^{miss}). It forms Regions of Interest (RoIs) for use by the Level-2 (L2) trigger. For particularly high rates a pre-scale can be applied where a pre-scale of X indicates that only 1 in every X events are passed to the next levels of the trigger system.
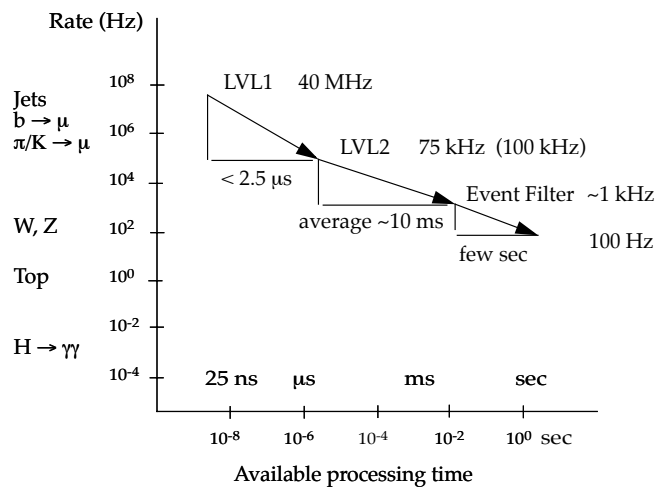
Figure 3.14: Event rate and processing times for the three levels of the ATLAS trigger. Rates for particular physics processes are demonstrated. Taken from Ref. [32].

L2 is a software based trigger. It examines each RoI from L1 in the detector system from which it originated, using the full granularity, to confirm whether it is a valid object. The advantage of this is that only 1-4% of the data for the event is

unpacked and analysed saving time[1]. After confirmation, additional features may be searched for in other detector systems e.g. for RoIs suspected of being taus, L2 may search for tracks in the SCT/Pixel and TRT detectors. The information from all systems is then combined to form more specialised global trigger objects that become candidates for leptons, jets, photons, $E_\mathrm{T}^\mathrm{miss}$ and B-physics objects. If the event is accepted by the L2 trigger the output is appended to the event and the full event is built before the final trigger stage. The latency of the L2 trigger is ~ 10 ms per event and it has a reduction rate on the order of 100, reducing the output rate to ~ 2 kHz.

The final stage of the ATLAS trigger is the Event Filter (EF). The EF looks at the complete event using the full granularity of the detector. Offline-like reconstruction algorithms can be run at this stage e.g. vertex reconstruction and track fitting can be performed. The EF classifies the events and stores accepted events for offline analysis.

3.4 ATLAS Computing

3.4.1 The Grid

Once the LHC begins operation the total data output from the four LHC experiments will be on the order of 10 PB per year [37]. This amount of data far exceeds that of any other experiment to date. Analysis of such an enormous amount of data is a major challenge. The large amounts of data will be handled with the use of Grid computing [38]. The Grid is a worldwide network of computing sites whose resources are combined to enable storage and processing of the data from the LHC. The raw data will be archived at CERN (known as Tier-0) before being processed and distributed to large computing sites around the world known as Tier-1 centres. These centres will archive the data, provide reprocessing capacity, allow access to reprocessed versions of the data and allow analysis of the processed data by physics groups to produce derived physics datasets (DPDs)

---

[1]There is an exception to this for B-physics candidates. For these events either large RoI as used or the entire event is read-out.

on which user analysis will be performed. The DPDs will be copied to Tier-2 facilities for further analysis.

3.4.2 The Athena framework

The ATLAS collaboration have developed offline software that can process the raw data delivered by the ATLAS detector, perform reconstruction of physics objects and provide common tools to perform analysis on the processed data. The Athena framework [39] provides a modular structure to contain the algorithms that make up this ATLAS software. It also incorporates event simulation tools. Athena is written in C++ and is driven by python scripting.

Chapter 4

Event simulation

Simulated data is an intrinsic part of all modern high-energy physics experiments. It allows particle physicists to model different descriptions of the physical world and determine, if this description is realised in nature, what is likely to happen in particle collisions and how this will appear in the detector. Simulated data can therefore be used as a reference to compare real experimental data with theory and it can also be used to build analyses and make predictions for future experiments for which data is not yet available. Since at the time of writing this thesis the ATLAS detector is yet to record data from real collisions at the LHC, simulated data is a vital part of the two analyses presented in this thesis.

Production of simulated data typically involves two main steps: Monte Carlo event generation and detector simulation. The full simulation chain is demonstrated in Figure 4.1 which also demonstrates the steps that will be taken to prepare the real raw data from the experiment when data taking begins. Simulated data samples will be referred to as Monte Carlo samples throughout this thesis.

4.1   Monte Carlo Event Generation

Monte Carlo (MC) generators are programs built to simulate physics processes, based on theory with input from previous experimental results. Hadronic event generators, as used for the LHC experiments, simulate the hard-process, ISR,
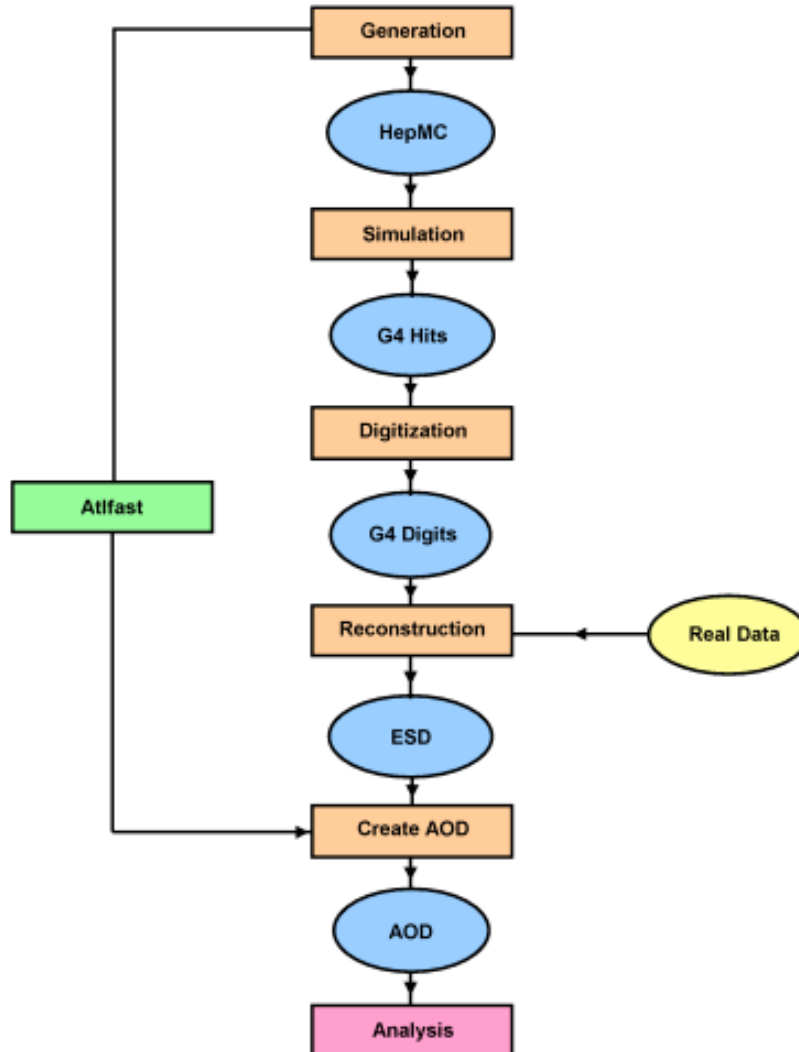
Figure 4.1: Flowchart demonstrating the steps in the preparation of both simulated and real raw data for use in physics analysis for the ATLAS experiment. Main data formats are shown in ovals, processing steps are shown in rectangles. Taken from Ref. [40].

FSR, beam remnants, hadronisation and decays. The output of the event generators contains information about the final state particles present in each simulated event including the four-vectors and position of production for each particle. It also contains information about the decay chain producing the final state particle; the parent, grandparent, great-grandparent etc. can be viewed for each final state particle, as well as the children of each of those parents.

A range of different MC generators are available for simulation of LHC events and are selected according to their suitability for a given physics process. Accurate simulations for events in hadron colliders are often achieved by combining components from different MC generators. For example, it may be best to simulate the signal process with one generator and the background processes with another. The following MC generators were used in the production of the simulated data used in this thesis:

PYTHIA   PYTHIA [41] is a general-purpose MC generator used to generate high energy physics events. For most of the processes simulated, the leading order matrix elements are used. The leading order calculation of the hard-scattering process is then supplemented with parton showering to take into account the effects of ISR and FSR, and the hadronisation of coloured particles.

HERWIG   Like PYTHIA, HERWIG [42] is a general-purpose generator. It includes a wide range of hard-scattering processes together with ISR, FSR, hadronisation, decays and underlying event simulation. The underlying event model is simulated based on a minimum-bias pp event generator. An external package, JIMMY [43], is available which uses a multiple scattering model for the underlying event. The model parameters of the underlying event are tuned to published data from the Tevatron and other experiments, as described in Ref. [44].

ALPGEN   ALPGEN [45] is designed for the generation of Standard Model processes in hadronic collisions that have final states with large jet multiplicities. It is known as a matrix element generator; it calculates the exact matrix elements for multiparton hard processes in hadronic collisions at leading order. Showering

and hadronisation can be performed by interfacing with HERWIG. In order to achieve the correct jet multiplicities it is necesary to perform matching between the jets produced by the matrix element generator and those produced by the parton showering in order that double counting doesn't occur. For this the MLM [46] matching technique is used.

MC@NLO   MC@NLO [47] includes the full NLO QCD correction in the computation of hard-scattering processes but as a result, only selected processes are simulated. The inclusion of the NLO matrix elements provides a better prediction of the rates involved. MC@NLO provides a good description of the final state kinematics for events with up to one additional QCD jet. One unusual feature of MC@NLO is the presence of events with negative weights. These are necessary in order to obtain the NLO results. Like ALPGEN, parton showering and hadronisation can be performed by interfacing the generator with HERWIG.

ISAJET   ISAJET [48] simulates hadron collisions at high energies. It is readily used in the simulation of supersymmetric events.

TAUOLA   The TAUOLA package [49] is a specialised package used to simulate the decays of τ-leptons.

4.2   Detector Simulation

Once the events have been generated, the passage of the generated particles through the detector is then simulated. There are currently two methods for simulating the ATLAS detector: a detailed simulation using the Geant 4 toolkit [50] known as full simulation (FULLSIM), and a simplified simulation known as fast simulation (ATLFAST) [51].

4.2.1   Full Simulation (FULLSIM)

The Geant 4 software uses an accurate model of the geometry and the material of the ATLAS detector in combination with detailed models of various ways in

which particles interact with matter e.g. ionisation, bremsstrahlung and multiple scattering. It tracks all stable particles through the layers of the ATLAS detector, taking into account the non-uniform magnetic field. The output from this stage is in the form of 'hits'. These hits are then converted into 'digits', which mimick the response that real data of this type would produce in the read out electronics of the experiment.

Real raw data from the ATLAS detector will come from the readout buffers in a bytestream form similar to the Geant 4 digits. The raw data will be converted into Raw Data Objects (RDOs) e.g. clusters from the pixel detector or drift circles from the MDTs. The same conversion is performed for the fully simulated events, converting the digits to RDOs. At this point, reconstruction algorithms can then be run on both the real data and the simulated data.

4.2.2 Fast Simulation (ATLFAST)

Whilst full simulation is desirable in terms of accurately modeling detector effects, it is very CPU and time intensive. For studies that require a large amount of statistics, full simulation is not feasible. ATLAS has two main fast simulation packages:

ATLFAST1   ATLFAST1 [51] smears the generated truth objects with detector resolutions in order to provide physics objects similar to those after reconstruction. It also corrects the efficiency for physics objects to be reconstructed to approximate the efficiency expected to be achieved by the reconstruction algorithms. It is ideal for physics parameter space scans and studies that do no require the level of detail provided by full simulation.

ATLFAST2   ATLFAST2 [52] includes a GEANT4 simulation of the inner detector and muon system supplemented by a fast calorimeter simulation. It is useful for supplementing full simulation studies when large statistics are needed and therefore full simulation is not feasible.

4.3   Higher Order Corrections

For many physics process it is sufficient to simulate the final state event topologies at LO and use corrections to the cross-section to approximate higher order effects. NLO (or NNLO) cross-sections can be approximated by multiplying the LO cross-section of the given process by a k-factor defined as:

$$k_{(N)NLO} \equiv \frac{\sigma_{(N)NLO}}{\sigma_{LO}} \tag{4.1}$$

.

4.4   Monte Carlo Samples Used in This Thesis

At the time of starting the work for this thesis it was believed that the start-up centre-of-mass energy of the LHC would be 14 TeV. Since then a start-up centre-of-mass energy of 10 TeV, and most recently, a centre-of-mass energy of 7 TeV has been proposed. As a result, two sets of Monte Carlo samples were used in this thesis: one set modeling a centre-of-mass energy of 14 TeV (which will be referred to as the 14 TeV MC samples) and a second set modeling a centre-of-mass energy of 10 TeV (which will be referred to as the 10 TeV MC samples). All of the MC samples were officially produced and validated by the ATLAS Collaboration.

4.4.1   14 TeV Monte Carlo Samples

The Monte Carlo samples used to model a centre-of-mass energy of 14 TeV were produced with Athena version 12.0.6 in the context of the Computing System Commissioning (CSC) studies [53]. The samples were generated with an instantaneous luminosity below 5×10^{32} and no pileup was imposed on the events. A common definition of particles masses was used among all samples. All samples were generated with a top quark mass of 175 GeV.

4.4.1.1   SUSY Benchmark Points

Two mSUGRA benchmark points where defined to model signals for SUSY (used in Chapter 6), one with a relatively small value of $\tan \beta$ and one with a large

value of $\tan\beta$:

- SU3: $m_0 = 100$ GeV, $m_{1/2} = 300$ GeV, $A_0 = -300$ GeV, $\tan\beta = 6$, $\mu > 0$.

- SU6: $m_0 = 320$ GeV, $m_{1/2} = 375$ GeV, $A_0 = 0$, $\tan\beta = 50$, $\mu > 0$.

The reasons for choosing these points will be discussed in Chapter 6. These points were chosen to be roughly consistent with the observed cold dark matter density. All SUSY particle masses were generated for each point using the ISAJET simulation package. Table 4.1 demonstrates the sparticle mass spectrum for each benchmark point. These mass spectra were then input into the HERWIG MC event generator. Table 4.2 lists the LO and NLO cross-sections of the generated samples as obtained using the PROSPINO program [54–56] (version 2.0.6) using the default settings and the CTEQ6M PDF set [57].

For both points the gluino mass is less than 1 TeV, $M(\tilde{g})/M(\tilde{\chi}_1^0) \sim 6$ and the squark and gluino masses are comparable. Therefore gluinos and squarks are strongly produced and decay via cascade decays into a number of hard jets, possible leptons and $E_{\mathrm{T}}^{\mathrm{miss}}$ as described further in Section 6.1.2. Although both points follow the mSUGRA model, this signature is relatively general among different SUSY models.

4.4.1.2 High $\tan\beta$ Grid

As well as the two benchmark points, a grid of SUSY points (a set of points in the SUSY parameter space of a given model) was generated in order to model a large number of possible SUSY signals. The grid was chosen to have a high value of $\tan\beta$:

High $\tan\beta$ mSUGRA grid This is a grid of 25×25 points with $A_0 = 0$, $\tan\beta = 50$ and $\mu < 0$. m_0 is varied from 200 GeV to 3000 GeV in steps of 200 GeV, and $m_{1/2}$ is varied from 100 GeV to 1500 GeV in steps of 100 GeV. Figure 4.2 shows the LO cross-section as calculated by HERWIG 6.510, in picobarns, for each of the points. The dashed regions are theoretically disallowed due to lack of electroweak symmetry breaking and the $\tilde{\tau}_1$ being the LSP (a charged LSP is not

Particle	SU3	SU6
$\tilde{d}_L$	636.27	870.79
$\tilde{u}_L$	631.51	866.84
$\tilde{b}_1$	575.23	716.83
$\tilde{t}_1$	424.12	641.61
$\tilde{d}_R$	610.69	840.21
$\tilde{u}_R$	611.81	842.16
$\tilde{b}_2$	610.73	779.42
$\tilde{t}_2$	650.50	797.99
$\tilde{e}_L$	230.45	411.89
$\tilde{\nu}_e$	216.96	401.89
$\tilde{\tau}_1$	149.99	181.31
$\tilde{\nu}_\tau$	216.29	358.26
$\tilde{e}_R$	155.45	351.10
$\tilde{\tau}_2$	232.17	392.58
$\tilde{g}$	717.46	894.70
$\tilde{\chi}_1^0$	117.91	149.57
$\tilde{\chi}_2^0$	218.60	287.97
$\tilde{\chi}_3^0$	463.99	477.23
$\tilde{\chi}_4^0$	480.59	492.23
$\tilde{\chi}_1^+$	218.33	288.29
$\tilde{\chi}_2^+$	480.16	492.42
h^0	114.83	116.85
H^0	512.86	388.92
A^0	511.53	386.47
H^+	518.15	401.15
t	175.00	175.00

Table 4.1: Masses in GeV of the SUSY particles for the fully simulated SUSY benchmark samples.

Signal	CSC ID	σLO (pb)	σNLO (pb)	N
SU3	005403	18.59	27.68	500 K
SU6	005404	4.48	6.07	30 K

Table 4.2: SUSY sample CSC ID, production cross section at LO and NLO, and the available number of events in the sample for the two benchmark points used in this thesis.

allowed due to cosmological arguments).

The SUSY mass spectrum was generated with ISAJET version 7.75. This was then input into HERWIG 6.510 to generate the MC events. ATLFAST1 was then used to simulate detector effects and for reconstruction. Dark matter and other existing constraints were ignored in the scan in order or provide as wide a range of signals as possible.

4.4.1.3 The Standard Model

The MC samples generated to model the SM are summarised in Table 4.3 and a brief summary of the samples follows:

Top pair production   The MC@NLO generator was used to generate the $t\bar{t}$ events. The fully hadronic decay mode was separated from the semileptonic and dileptonic decay modes. The former will be referred to as "hadronic $t\bar{t}$" in the following and the latter as "leptonic $t\bar{t}$". The cross-sections for both samples were normalised to NLO including NLL resummation of soft effects.

W/Z Boson+jets   ALPGEN was used to generate the associated production of W and Z bosons and jets. In order to increase the statistics, a filter was applied at generator level requiring four jets with $p_T > 40$ GeV, $p_T(jet_1) > 80$ GeV and $E_T^{\mathrm{miss}} > 80$ GeV. Showering and hadronisation were performed by HERWIG and multi-parton interactions were modeled by JIMMY. The overall cross-sections were normalised to NLO by applying a k-factor of 1.15 (1.27) for the W (Z) samples provided by the FEWZ [59] program.
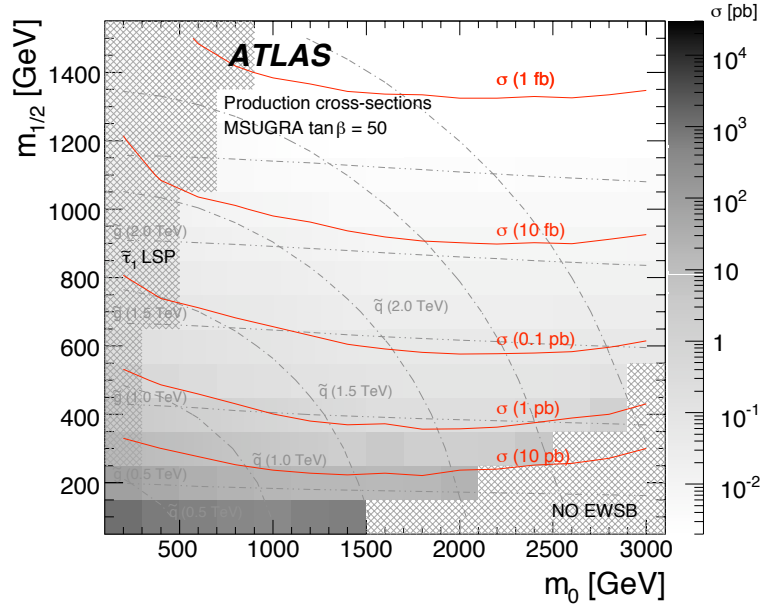
Figure 4.2: LO production cross-section for the m_0 vs $m_{1/2}$ high $\tan\beta$ grid of 25×25 points generated with ISAJET 7.75. $A_0 = 0$, $\tan\beta = 50$ and $\mu < 0$. The cross-sections are calculated by Herwig 6.510. The dashed regions are not theoretically viable due to a lack of electroweak symmetry breaking and the $\tilde{\tau}_1$ being the LSP. Lines of equal squark and gluino masses are shown, where the squark masses are taken as the mass of the lightest squark except the stop and the sbottom. Taken from Ref. [58].

Background	CSC ID	Generator	σ_{eff} [pb]	L [pb^{-1}]
$t\bar{t}$	5200_topleptonic	MC@NLO	450	971
	5204_tophadronic	MC@NLO	383	188
Multijet	8090_J4MET	PYTHIA	916	74.2
	8091_J5MET	PYTHIA	655	140
	8092_J6MET	PYTHIA	67.4	477
	8093_J7MET	PYTHIA	5.3	660
	8094_J8MET	PYTHIA	0.022	$1.92 \cdot 10^5$
W$\to e\nu$+jets	5223_Wenu2p	ALPGEN+HERWIG	0.768	977
	5224_Wenu3p	ALPGEN+HERWIG	3.90	$4.04 \cdot 10^3$
	5225_Wenu4p	ALPGEN+HERWIG	2.32	$4.27 \cdot 10^3$
	5226_Wenu5p	ALPGEN+HERWIG	0.685	$4.31 \cdot 10^3$
W$\to \mu\nu$+jets	8203_Wmunu3p	ALPGEN+HERWIG	0.799	$2.50 \cdot 10^3$
	8204_Wmunu4p	ALPGEN+HERWIG	2.13	469
	8205_Wmunu5p	ALPGEN+HERWIG	0.701	$5.71 \cdot 10^3$
W$\to \tau\nu$+jets	8208_Wtaunu2p	ALPGEN+HERWIG	0.615	$4.47 \cdot 10^3$
	8209_Wtaunu3p	ALPGEN+HERWIG	3.27	535
	8210_Wtaunu4p	ALPGEN+HERWIG	3.08	$4.55 \cdot 10^3$
	8211_Wtaunu5p	ALPGEN+HERWIG	0.935	$5.03 \cdot 10^3$
Z$\to ee$+jets	5161_Zee1p	ALPGEN+HERWIG	0.401	$3.74 \cdot 10^3$
	5162_Zee2p	ALPGEN+HERWIG	4.15	$1.46 \cdot 10^3$
	5163_Zee3p	ALPGEN+HERWIG	2.76	$7.92 \cdot 10^3$
	5164_Zee4p	ALPGEN+HERWIG	0.694	$8.64 \cdot 10^3$
	5165_Zee5p	ALPGEN+HERWIG	0.176	$1.14 \cdot 10^4$
Z$\to \mu\mu$+jets	8109_Zmumu3p	ALPGEN+HERWIG	0.240	$8.32 \cdot 10^3$
	8110_Zmumu4p	ALPGEN+HERWIG	0.527	$4.17 \cdot 10^3$
	8111_Zmumu5p	ALPGEN+HERWIG	0.170	$1.03 \cdot 10^4$
Z$\to \tau\tau$+jets	8114_Ztautau2p	ALPGEN+HERWIG	0.215	$1.74 \cdot 10^4$
	8115_Ztautau3p	ALPGEN+HERWIG	0.411	$1.70 \cdot 10^4$
	8116_Ztautau4p	ALPGEN+HERWIG	0.207	$1.93 \cdot 10^4$
	8117_Ztautau5p	ALPGEN+HERWIG	0.062	$1.62 \cdot 10^4$
Z$\to \nu\nu$+jets	5124_Znunu3p	ALPGEN+HERWIG	1.07	$1.07 \cdot 10^4$
	5125_Znunu4p	ALPGEN+HERWIG	3.06	$8.50 \cdot 10^3$
	5126_Znunu5p	ALPGEN+HERWIG	0.951	$1.21 \cdot 10^4$
Diboson	5985_WW	HERWIG	39.0	$1.26 \cdot 10^3$
	5986_ZZ	HERWIG	2.81	$2.39 \cdot 10^4$
	5987_WZ	HERWIG	14.0	$3.49 \cdot 10^3$

Table 4.3: SM samples generated with a centre-of-mass energy of 14 TeV with the corresponding ATLAS internal identification number, the generator used, the sample luminosities and the cross-sections after filter and matching efficiencies when applicable.

Multijet QCD processes   PYTHIA was used to generate multijet QCD processes. For the simulation of QCD multijet processes ALPGEN is a more appropriate choice of generator but for practical reasons, it was impossible to generate ALPGEN QCD samples with sufficiently large statistics. With PYTHIA the processes were generated in different p_T ranges and in order to increase statistics in the interesting regions of the analysis, a filter was applied at generator level requiring $p_T(jet_1) > 80$ GeV, $p_T(jet_2) > 40$ GeV and $E_T^{\mathrm{miss}} > 100$ GeV. The cross-sections were normalised to LO.

Diboson   HERWIG was used to generate the diboson processes WW, WZ and ZZ. The samples were normalised to NLO cross-sections obtained using the MCFM program [60].

4.4.2   10 TeV Monte Carlo Samples

The Monte Carlo samples used to model a centre-of-mass energy of 10 TeV were produced with Athena version 14. A common definition of particle masses was used among all samples. All samples were generated with a top quark mass of 172.5 GeV. Where possible the GEANT 4 full simulation of the ATLAS detector was used, however, when statistics were limited the samples were generated using the fast simulation package ATLFAST2 in order to generate sufficient statistics. Most of the QCD multijet samples were generated with ATLFAST2 as were the $Z \rightarrow \nu\nu$+jets samples. The electroweak MC samples are summarised in Table 4.4, the QCD multijet MC samples are summarised in Table 4.5, and a brief summary of the samples follows:

Top pair production   The MC@NLO generator was used to generate the $t\bar{t}$ events. Parton showering and fragmentation were simulated using HERWIG and Jimmy. The fully hadronic decay mode was separated from the semileptonic and dileptonic decay modes. The former will be referred to as "hadronic $t\bar{t}$" in the following and the latter as "leptonic $t\bar{t}$". Both samples were normalised to NLO including NLL resummation of soft effects.

Background	ATLAS ID	Generator	σ_{eff} [pb]	N_{events}
$t\bar{t}$	105200_topleptonic	MC@NLO	$2.17 \cdot 10^2$	$1.43 \cdot 10^6$
	105204_tophadronic	MC@NLO	$1.83 \cdot 10^2$	$6.80 \cdot 10^5$
Single t	105500_Wt	AcerMC	$1.43 \cdot 10^1$	$1.00 \cdot 10^3$
	105502_tchan	AcerMC	$4.32 \cdot 10^1$	$2.99 \cdot 10^4$
$W \rightarrow e\nu$+jets	107680_Wenu0p	ALPGEN+HERWIG	$1.24 \cdot 10^4$	$1.22 \cdot 10^6$
	107681_Wenu1p	ALPGEN+HERWIG	$2.58 \cdot 10^3$	$2.22 \cdot 10^5$
	107682_Wenu2p	ALPGEN+HERWIG	$8.25 \cdot 10^2$	$1.55 \cdot 10^5$
	107683_Wenu3p	ALPGEN+HERWIG	$2.48 \cdot 10^2$	$2.24 \cdot 10^5$
	107684_Wenu4p	ALPGEN+HERWIG	$6.84 \cdot 10^1$	$4.89 \cdot 10^4$
	107685_Wenu5p	ALPGEN+HERWIG	$2.03 \cdot 10^1$	$1.75 \cot 10^4$
$W \rightarrow \mu\nu$+jets	107690_Wmunu0p	ALPGEN+HERWIG	$1.24 \cdot 10^4$	$6.69 \cdot 10^5$
	107691_Wmunu1p	ALPGEN+HERWIG	$2.63 \cdot 10^3$	$2.62 \cdot 10^5$
	107692_Wmunu2p	ALPGEN+HERWIG	$8.32 \cdot 10^2$	$7.50 \cdot 10^5$
	107693_Wmunu3p	ALPGEN+HERWIG	$2.46 \cdot 10^2$	$2.23 \cdot 10^5$
	107694_Wmunu4p	ALPGEN+HERWIG	$6.77 \cdot 10^1$	$5.89 \cdot 10^4$
	107695_Wmunu5p	ALPGEN+HERWIG	$1.99 \cdot 10^1$	$1.75 \cdot 10^4$
$W \rightarrow \tau\nu$+jets	107700_Wtaunu0p	ALPGEN+HERWIG	$1.24 \cdot 10^4$	$1.33 \cdot 10^6$
	107701_Wtaunu1p	ALPGEN+HERWIG	$2.57 \cdot 10^3$	$1.86 \cdot 10^5$
	107702_Wtaunu2p	ALPGEN+HERWIG	$8.21 \cdot 10^2$	$7.93 \cdot 10^5$
	107703_Wtaunu3p	ALPGEN+HERWIG	$2.47 \cdot 10^2$	$1.57 \cdot 10^5$
	107704_Wtaunu4p	ALPGEN+HERWIG	$6.75 \cdot 10^1$	$5.26 \cdot 10^4$
	107705_Wtaunu5p	ALPGEN+HERWIG	$2.07 \cdot 10^1$	$1.74 \cdot 10^4$
$Z \rightarrow ee$+jets	107650_Zee0p	ALPGEN+HERWIG	$1.10 \cdot 10^3$	$2.69 \cdot 10^5$
	107651_Zee1p	ALPGEN+HERWIG	$2.52 \cdot 10^2$	$6.18 \cdot 10^4$
	107652_Zee2p	ALPGEN+HERWIG	$8.85 \cdot 10^1$	$1.37 \cdot 10^5$
	107653_Zee3p	ALPGEN+HERWIG	$2.57 \cdot 10^1$	$5.34 \cdot 10^4$
	107654_Zee4p	ALPGEN+HERWIG	$7.32 \cdot 10^0$	$1.83 \cdot 10^4$
	107656_Zee5p	ALPGEN+HERWIG	$2.11 \cdot 10^0$	$5.50 \cdot 10^3$
$Z \rightarrow \mu\mu$+jets	107660_Zmumu0p	ALPGEN+HERWIG	$1.10 \cdot 10^3$	$2.60 \cdot 10^5$
	107661_Zmumu1p	ALPGEN+HERWIG	$2.50 \cdot 10^2$	$6.17 \cdot 10^4$
	107662_Zmumu2p	ALPGEN+HERWIG	$8.46 \cdot 10^1$	$1.97 \cdot 10^5$
	107663_Zmumu3p	ALPGEN+HERWIG	$2.64 \cdot 10^1$	$6.47 \cdot 10^4$
	107664_Zmumu4p	ALPGEN+HERWIG	$7.42 \cdot 10^0$	$1.85 \cdot 10^4$
	107665_Zmumu5p	ALPGEN+HERWIG	$2.07 \cdot 10^0$	$5.47 \cdot 10^3$
$Z \rightarrow \tau\tau$+jets	107670_Ztautau0p	ALPGEN+HERWIG	$1.10 \cdot 10^3$	$2.71 \cdot 10^5$
	107671_Ztautau1p	ALPGEN+HERWIG	$2.55 \cdot 10^2$	$6.27 \cdot 10^4$
	107672_Ztautau2p	ALPGEN+HERWIG	$8.56 \cdot 10^1$	$2.10 \cdot 10^5$
	107673_Ztautau3p	ALPGEN+HERWIG	$2.57 \cdot 10^1$	$6.34 \cdot 10^4$
	107674_Ztautau4p	ALPGEN+HERWIG	$7.34 \cdot 10^0$	$1.85 \cdot 10^4$
	107675_Ztautau5p	ALPGEN+HERWIG	$2.09 \cdot 10^0$	$5.48 \cdot 10^3$
$Z \rightarrow \nu\nu$+jets	107713_Znunu3p	ALPGEN+HERWIG	$1.48 \cdot 10^2$	$3.37 \cdot 10^5$
	107713_Znunu4p	ALPGEN+HERWIG	$4.15 \cdot 10^1$	$9.95 \cdot 10^4$
	107713_Znunu5p	ALPGEN+HERWIG	$1.17 \cdot 10^2$	$2.90 \cdot 10^4$
Diboson	105921_WpWm	MC@NLO	$8.28 \cdot 10^{-1}$	$1.73 \cdot 10^4$
	105922_WpWm	MC@NLO	$8.28 \cdot 10^{-1}$	$1.74 \cdot 10^4$
	105923_WpWm	MC@NLO	$8.28 \cdot 10^{-1}$	$1.41 \cdot 10^4$
	105924_WpWm	MC@NLO	$8.28 \cdot 10^{-1}$	$1.73 \cdot 10^4$
	105925_WpWm	MC@NLO	$8.28 \cdot 10^{-1}$	$1.69 \cdot 10^4$
	105926_WpWm	MC@NLO	$8.28 \cdot 10^{-1}$	$7.04 \cdot 10^3$
	105927_WpWm	MC@NLO	$8.28 \cdot 10^{-1}$	$1.72 \cdot 10^4$
	105928_WpWm	MC@NLO	$8.28 \cdot 10^{-1}$	$1.73 \cdot 10^4$
	105929_WpWm	MC@NLO	$8.28 \cdot 10^{-1}$	$1.72 \cdot 10^4$
	105931_ZZ_llll	MC@NLO	$4.06 \cdot 10^{-2}$	$1.33 \cdot 10^4$
	105932_ZZ_llnunu	MC@NLO	$2.47 \cdot 10^{-1}$	$1.35 \cdot 10^4$
	105941_WpZ_lnull	MC@NLO	$2.65 \cdot 10^{-1}$	$1.46 \cdot 10^4$
	105942_WpZ_qqll	MC@NLO	$8.29 \cdot 10^{-1}$	$3.64 \cdot 10^3$
	105971_WmZ_lnull	MC@NLO	$1.56 \cdot 10^{-1}$	$1.13 \cdot 10^4$
	105972_WmZ_qqll	MC@NLO	$4.88 \cdot 10^{-1}$	$3.65 \cdot 10^3$

Table 4.4: Electroweak SM samples generated with a centre-of-mass energy of 10 TeV

Background	ATLAS ID	Generator	σ_{eff} [pb]	N_{events}
Heavy flavour	107365_J3Np0	ALPGEN	$4.74 \cdot 10^2$	$2.85 \cdot 10^3$
	107366_J3Np1	ALPGEN	$1.08 \cdot 10^4$	$1.08 \cdot 10^5$
	107367_J3Np2	ALPGEN	$1.07 \cdot 10^4$	$1.10 \cdot 10^4$
	108368_J3Np3	ALPGEN	$6.95 \cdot 10^3$	$6.95 \cdot 10^4$
	107310_J4Np0	ALPGEN	$1.48 \cdot 10^2$	$1.50 \cdot 10^3$
	107311_J4Np1	ALPGEN	$1.08 \cdot 10^3$	$1.10 \cdot 10^4$
	107312_J4Np2	ALPGEN	$1.43 \cdot 10^3$	$1.45 \cdot 10^4$
	107313_J4Np3	ALPGEN	$1.02 \cdot 10^3$	$1.05 \cdot 10^4$
	107314_J4Np4	ALPGEN	$7.06 \cdot 10^2$	$7.50 \cdot 10^3$
	107315_J5Np0	ALPGEN	$3.20 \cdot 10^0$	$1.00 \cdot 10^3$
	107316_J5Np1	ALPGEN	$2.52 \cdot 10^1$	$8.00 \cdot 10^3$
	107317_J5Np2	ALPGEN	$5.00 \cdot 10^1$	$1.55 \cdot 10^4$
	107318_J5Np3	ALPGEN	$5.29 \cdot 10^1$	$1.60 \cdot 10^4$
	107319_J5Np4	ALPGEN	$5.55 \cdot 10^1$	$1.70 \cdot 10^4$
Light flavour	108362_J4Np2	ALPGEN	$3.19 \cdot 10^4$	$3.08 \cdot 10^5$
	108363_J4Np3	ALPGEN	$6.55 \cdot 10^4$	$5.36 \cdot 10^5$
	108364_J4Np4	ALPGEN	$4.90 \cdot 10^4$	$4.50 \cdot 10^5$
	108365_J4Np5	ALPGEN	$2.42 \cdot 10^4$	$2.22 \cdot 10^5$
	108366_J4Np6	ALPGEN	$1.16 \cdot 10^4$	$1.06 \cdot 10^5$
	108367_J5Np2	ALPGEN	$7.50 \cdot 10^2$	$1.95 \cdot 10^5$
	108368_J5Np3	ALPGEN	$1.94 \cdot 10^3$	$5.73 \cdot 10^5$
	108369_J5Np4	ALPGEN	$2.15 \cdot 10^3$	$6.44 \cdot 10^5$
	108370_J5Np5	ALPGEN	$1.39 \cdot 10^3$	$4.18 \cdot 10^5$
	108371_J5Np6	ALPGEN	$9.73 \cdot 10^2$	$2.92 \cdot 10^5$
	108377_J3Np2	ALPGEN	$1.02 \cdot 10^5$	$1.02 \cdot 10^6$
	108379_J3Np4	ALPGEN	$3.32 \cdot 10^5$	$3.18 \cdot 10^6$
	108380_J3Np3	ALPGEN	$1.45 \cdot 10^5$	$1.43 \cdot 10^6$

Table 4.5: QCD multijet SM samples generated with a centre-of-mass energy of 10 TeV with the corresponding ATLAS internal identification number, the generator used, the cross-sections after filter and matching efficiencies when applicable and the number of events.

W/Z Boson+jets   ALPGEN+HERWIG were used to generate the associated production of W and Z bosons and jets. The MLM matching procedure was used to avoid double counting of jets. No filter was applied to the W and Z samples decaying to leptons except the MLM matching criteria. For the Z decays to neutrinos, at least one jet with $p_T > 30$ GeV was required to allow events to have a chance of being triggered. The overall cross-sections were normalised to NNLO by applying a k-factor of 1.22, provided by the FEWZ [59] program.

Multijet QCD processes   ALPGEN+HERWIG were used to generate the QCD processes. The generation was split according to the number of partons in the final state and the p_T of the leading parton. In addition, in order to increase statistics in the interesting regions of the analysis, a filter was applied at generator level to the J3 samples requiring either at least one true jet reconstructed with a cone algorithm (cone size $\Delta R = 0.4$) with $p_T > 120$ GeV and $|\eta| < 2.8$ or at least one true jet with $p_T > 60$ GeV and a minimum of two additional jets with $p_T > 25$ GeV or at least one true jet with $p_T > 70$ GeV and a minimum of one additional jets with $p_T > 25$ GeV where the minimum angle between the jets $\Delta\phi$ is 0.8. Since the heavy flavour content of the ALPGEN QCD multijet samples is limited to $g \rightarrow b\bar{b}$ processes with low p_T and small angular separation, a separate series of ALPGEN QCD $b\bar{b}$ with extra jets ($p_T(b) > 20$ GeV and $\Delta R(b\bar{b}) > 0.7$) were also considered. This introduces some double counting but it can be safely neglected. Samples were normalised to LO.

Diboson   The WW, ZZ and WZ decays to leptons were generated using MC@NLO. HERWIG/JIMMY was used to model the parton shower development. Samples were normalised to the theoretical inclusive NLO cross sections according to [61].

Single top   The leading order generator AcerMC [62] was used to generate the single top processes. Samples were normalised to NLO using the MCMF program [60].

Chapter 5

Offline Reconstruction and Identification

The raw data from the ATLAS detector will appear as a series of readout signals. The task of the offline reconstruction software is to translate this stream of readout signals into the information necessary to perform physics analysis. The clusters and tracks observed in different detector systems are combined to identify physics objects (e.g. jets, leptons, photons) and to measure their properties (e.g. momentum, position, charge) as accurately as possible. The reconstruction of these objects is performed by dedicated algorithms within the Athena framework.

The offline reconstruction relevant to objects used in this thesis will be briefly described below with particular emphasis given to the reconstruction of the tau lepton, which is the main focus of this thesis.

5.1   Clusters

Clusters are grouped energy deposits in the electromagnetic and hadronic calorimeters. Two methods are currently used to reconstruct these clusters within the ATLAS Collaboration, producing two types of clusters: Calorimeter Towers ("CaloTowers") [63] and Topological Clusters ("TopoClusters") [63]. CaloTowers are the sums of the energies of cells in the calorimeters in projective towers of size $\Delta\eta \times \Delta\phi = 0.1 \times 0.1$. TopoClusters are formed from clusters of cells in the

calorimeter with a significant signal. An algorithm is used that takes cells with a significance greater than 4σ (where σ is the standard deviation of the fluctuation due to noise) as seeds and adds neighbouring cells whose significance is greater than 2σ until no cells in the neighbourhood of the cluster are found to have a significant energy.

5.2 Electrons

An electron passing through the detector will leave a track in the Inner Detector and an energy deposit in the EM Calorimeter. Electrons are reconstructed by searching for EM calorimeter clusters and matching an inner detector track to them. A "sliding window" algorithm, which forms rectangular clusters with a fixed size and positions them so as to maximise the amount of energy within the cluster, is used to find and reconstruct the EM clusters [64]. The matching track is required to be in a $\Delta\eta \times \Delta\phi$ window of 0.05×0.10 such that the momentum of the track p and the clutser energy E obey $p/E < 10$. If a matching track is found the reconstruction algorithm checks for the presence of an associated conversion. If no such conversion is found an electron candidate is formed.

Hadronic jets form the main background to electron identification. For each electron candidate the reconstruction algorithm, eGamma [64], uses discriminating variables (e.g. shower shape and track quality cuts) to separate the electrons from the hadronic jets.

5.3 Muons

A muon passing through the detector will leave its signature in all subsystems. Accurate muon identification and measurement is obtained by combining the information from each subsystem in the reconstruction algorithm. Muon identification begins with a single track in the muon spectrometer. The track is then extrapolated towards the inner detector to check that it points towards the interaction point. A search is then performed for matching tracks in the Inner

Detector.

There are currently two main collections of algorithms for identification and reconstruction of muons. The Staco collection [65] includes the MUONBOY, STACO and MuTag algorithms. The MUID collection [66, 67] includes the MOORE, MuIdCombined and MuGirl algorithms. Muons identified by the muon spectrometer alone are known as 'standalone' muons. These muons are reconstructed using the MUONBOY and the MOORE algorithms. The majority of muons reconstructed by ATLAS are known as 'combined'. These muons are reconstructed by combining the information from the Inner Detector with the information from the muon spectrometer. The identification of combined muons is limited to $|\eta| < 2.5$ but the resolution is increased for $p_\mathrm{T} < 100$ GeV. The STACO algorithm reconstructs combined muons by statistically merging the tracks and assessing the success of the matching. A correction is made for the energy lost by the muon as it traverses the calorimeter (~ 3 GeV). The MuIdCombined algorithm performs a global refit of all hits associated to the two tracks. Muons that have tracks in the Inner Detector but only isolated segment hits in the muon spectrometer are known as 'tagged'. These are reconstructed by the MuTag and MuGirl algorithms.

5.4 Jets

When quarks or gluons hadronise they form jets of hadrons. These jets will leave tracks in the Inner Detector since they contain charged particles (either the hadrons themselves or their decay products), and energy deposits in the electromagnetic and hadronic calorimeters. In this thesis, and for many analyses in ATLAS, a seeded-jet cone algorithm [63] is used to reconstruct the jets. The cone algorithm uses high-p_T particles ($p_\mathrm{T} > 1$ GeV) as seeds for the jets. All objects around the seed in a particular cone radius ΔR are summed together and an energy weighted central value is taken. This then becomes the axis and the process is repeated moving the centre of the cone until the cone axis does not change, at which point the cone is considered stable and is called a jet.

During this process it is possible that cones may overlap. In order to reconcile these situations a process called "split-merge" is performed whereby if the energy shared between two overlapping cones is more than 50% of the less energetic jet, the jets are merged. If the share of the energy is less than 50% the jets are split into two separate jets. This prevents situations where single particles belong to more than one jet.

5.5 Missing Transverse Momentum ($E_\mathrm{T}^\mathrm{miss}$)

The goal of $E_\mathrm{T}^\mathrm{miss}$ reconstruction is to identify $E_\mathrm{T}^\mathrm{miss}$ in the calorimeter by cancelling the summed transverse momentum. If there is a high p_T muon in the event the $E_\mathrm{T}^\mathrm{miss}$ from the muon system must be calculated separately and added to that in the calorimeter since most of the muon energy would escape detection by the calorimeters. A common algorithm used for the reconstruction of $E_\mathrm{T}^\mathrm{miss}$ by the ATLAS Collaboration is the refined calibration of the $E_\mathrm{T}^\mathrm{miss}$ known as RefMETFinal [68] . RefMETFinal calculates the $E_\mathrm{T}^\mathrm{miss}$ using the calorimeter cells with calibration weights derived separately for cells associated to different objects (jets, electrons, photons and taus, and non-associated clusters due to the soft part of the event). The association to physics objects improves the $E_\mathrm{T}^\mathrm{miss}$ reconstruction since the calibration of identified physics objects will be known more accurately than a global calibration.

5.6 Reconstruction and Identification of Tau Leptons

Tau leptons are the most difficult lepton species to identify and reconstruct. It is not possible to distinguish between the leptons from leptonic tau decays and other prompt leptons in the detector, therefore only hadronic decay modes can be identified. Even then the hadronic decay modes suffer from a large background from QCD jets. The ATLAS Collaboration have developed dedicated algorithms to identify hadronically decaying tau leptons, separating them from the large QCD

background using a combination of calorimeter clusters and Inner Detector tracks.

Historically, two offline algorithms have been created by the ATLAS Collaboration for the reconstruction of taus: a calorimetry-based algorithm (tauRec) and a track-based algorithm (tau1p3p) [69]. Over the time period in which the work for this thesis has been performed, the tau reconstruction algorithms have undergone development in preparation for the LHC startup. The descriptions of the algorithms below refer to those implemented in Athena version 12, which was used to reconstruct the 14 TeV MC samples used for the majority of this thesis. Following the descriptions of the two algorithms an effort will be made to describe the major changes to the algorithms, implemented in Athena version 14, which was used to reconstruct the 10 TeV MC samples.

5.6.1 The Calorimetry-Based Algorithm (tauRec)

The calorimetry-based algorithm takes clusters from the calorimeter, formed using a sliding-window algorithm, as seeds for the tau reconstruction. The sliding-window algorithm operates on CaloTowers. The reconstructed cluster consists of 5×5 core CaloTowers. The core CaloTowers are used to calculate the energy of the cluster. Only clusters with $E_\mathrm{T} > 15$ GeV are accepted as seeds to the tau reconstruction. All cells within $\Delta R < 0.4$ of the barycenter of the cluster are calibrated with a H1-style energy calibration [70].

The reconstruction algorithm uses the cells forming the seed cluster to calculate a series of variables using the full granularity of the calorimeters, that can be used to discriminate between real tau leptons and fake candidates from QCD jets. The following variables are used:

- **Electromagnetic radius:** The EM radius is given by:

$$R_{em} = \frac{\sum_{i=1}^{n} E_{\mathrm{T},i} \sqrt{(\eta_i - \eta_\mathrm{cluster})^2 + (\phi_i - \phi_\mathrm{cluster})^2}}{\sum_{i=1}^{n} E_{\mathrm{T},i}} \quad (5.1)$$

  where $E_{\mathrm{T},i}$ is the transverse energy of the ith out of n electromagnetic calorimeter cells inside the cluster within $\Delta R < 0.4$. This variable uses

the small transverse shower profile of the tau lepton to discriminate against QCD jets. However its discriminating power is reduced at high E_T when tau jets and QCD jets become boosted and thus more collimated.

- **Isolation in the calorimeter:** Tau jets are well collimated therefore a tight isolation criteria can be used. The isolation fraction is defined as:

$$\Delta E_T^{12} = \frac{\sum_i E_{T,i}}{\sum_j E_{T,j}} \qquad (5.2)$$

where the indices i and j run over the EM calorimeter cells in a cone of $0.1 < \Delta R < 0.2$ and $\Delta R < 0.4$ respectively, around the cluster. $E_{T,i}$ and $E_{T,j}$ represent the transverse energies of the cells. Similar to the EM radius, the discrimination becomes smaller for higher E_T. Its performance will also be degraded in a more active environment e.g. $t\bar{t}$ production. The isolation criteria depends on the specific samples.

- **Number of associated tracks:** As was described in Section 1.1.2, hadronic tau-decays are typically associated with one ($\sim 77\%$) or three ($\sim 23\%$) charged tracks. The number of tracks with $p_T > 2$ GeV inside a cone of $\Delta R < 0.3$ from the cluster centre is counted. Despite their 1-prong and 3-prong decays, a significant fraction of zero, two and four tracks can be found due to the track reconstruction efficiencies and quality requirements placed on the tracks. Tau jet candidates are required to have between 1 and 3 associated tracks.

- **Charge:** The charge of the tau jet is defined as the sum of the charge of all associated tracks.

- **Number of hits in the η-strip layer:** Cells in the η-strip layer within $\Delta R < 0.4$ around the cluster centre count as a hit if they have an $E_T > 200$ MeV. QCD jets, particularly at high E_T, tend to show more hits than tau jets.

- **Transverse energy width in the η-strip layer:** The width is defined as:

$$\Delta\eta = \sqrt{\frac{\sum_{i=1}^{n} E_{\mathrm{T},i}^{\mathrm{strip}}(\eta_i - \eta_{\mathrm{cluster}})^2}{\sum_{i=1}^{n} E_{\mathrm{T},i}^{\mathrm{strip}}}} \tag{5.3}$$

  The width in the calorimeter is a powerful discriminator at low E_{T}. Its performance is diminished with rising E_{T} when QCD jets become boosted.

- **Lifetime signed pseudo impact parameter significance:** The impact parameter d_0 is defined as the smallest distance of a track to the beam axis $(0,0)$ in the (x, y) plane. From this a quantity called the "lifetime signed pseudo impact parameter" is constructed as follows:

$$\sigma_{IP} = d_0/\sigma_{d_0} * \mathrm{sign}(\sin(\psi_{cl} - \psi_{tr})) \tag{5.4}$$

  where σ_{d_0} is the error on d_0 as defined by the track fitting and ψ_{cl} and ψ_{tr} are the angles in the (x, y) plane at the cluster and at the point of the closest approach for the track respectively. σ_{IP} is constructed such that it has a positive sign if the decay happens in the flight direction of the track. A bias towards positive values is therefore expected for tracks with true lifetimes.

- **E_T/p_T of the leading track:** The leading track in a hadronic tau jet is expected to take a high fraction of the overall energy. QCD jets are expected to have a more uniform distribution of energy across the tracks and are also expected to have more neutral particles. $E_{\mathrm{T}}/p_{\mathrm{T}}$, where E_{T} is the calibrated transverse energy measured in the calorimeter and p_{T} is the transverse momentum of the leading track as measured in the Inner Detector, aims to exploit this feature for discrimination.

The above discriminating variables are used to build a one-dimensional likelihood function. Figure 5.1 shows an example of the distribution of this likelihood function for a sample of real tau jets and QCD background. By placing a cut on this likelihood, a significant fraction of the QCD background can be eliminated.
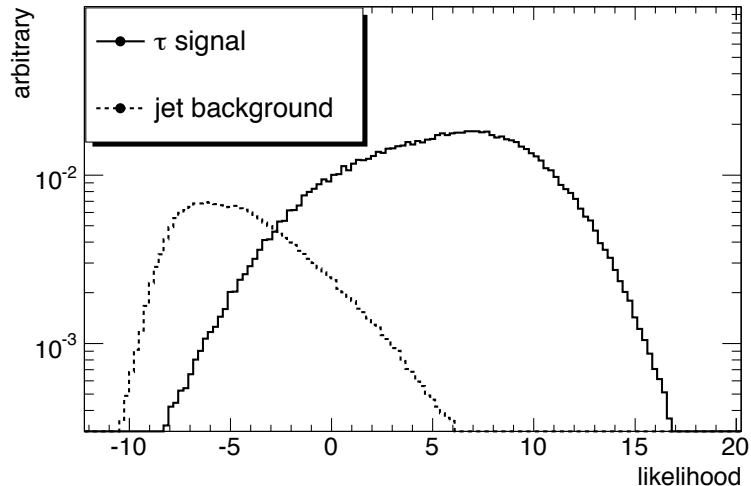
Figure 5.1: An example likelihood (LLH) distribution for real tau jets (solid) and QCD jets (dashed). Taken from Ref. [69].

5.6.2 The Track-Based Algorithm (tau1p3p)

The track-based algorithm (tau1p3p) is composed of two algorithms: tau1p for reconstructing 1-prong decays and tau3p for reconstructing 3-prong decays. Both algorithms use tracks, required to pass a series of quality cuts[1], with $p_T > 9$ GeV as seeds. For the 1-prong mode, one qualified track is required with no nearby qualified tracks in a cone of radius $\Delta R_{core} < 0.2$. For the 3-prong mode, exactly two or three nearby tracks are required, with the most energetic track chosen to be the leading track. Two tracks are included to recover three-prong candidates whose third track does not meet the quality criteria. The position of a candidate in (η, ϕ) is defined by the position of the perigee of the leading track (for the 1-prong mode) or the barycentre of the track system weighted with p_T (for the 3-prong mode).

An energy flow algorithm is used to define the energy of the tau candidate using

---

[1]The quality cuts involve requiring a minimal number of hits in the silicon and straw detectors, a threshold on the value of the impact parmeter and a threshold on the value of χ^2 of the fit for the trajectory reconstruction.

only tracks and the energy in the EM calorimeter [69]. This energy flow approach gives good performance for real tau jets but significantly underestimates the nominal energy of fake tau jets since a core cone of $\Delta R_{core} < 0.2$ is too narrow to efficiently collect the energy of a QCD jet. Also, the hadronic calorimeter doesn't contribute to the energy flow so a significant part of the neutral hadronic energy of a QCD jet is omitted. This means that QCD jets will appear to have lower p_{T} values, allowing rejection with a fixed p_{T} cut.

Similar to the calorimetry-based algorithm, discriminating variables are used to help reject QCD jets. These include variables such as the EM Radius, the number of tracks in an isolation cone of $0.2 < \Delta R_{iso} < 0.4$, the invariant mass of the track system (in the case of 3-prong candidates), amongst others. Instead of a likelihood, the variables are used to construct probability densities in a PDE-RS (Probability Density Estimation based on Range Searching) [69] to select real taus and reject background from QCD jets.

5.6.3 Recent Developments

Several changes to the algorithms have been made in the past year. These changes are described in detail in Ref. [71]. Most notably for the calorimetry-based algorithm, topological clusters (TopoClusters) are now used rather than the sliding window reconstruction on CaloTowers. This has led to a significant improvement in the tau reconstruction efficiency at low p_{T}.

Another major development is that the calorimetry-based algorithm and the track-based algorithm have now been merged into a single algorithm in order to gain the advantages of both of the methods. Now, hadronically decaying taus are reconstructed with one or both of two possible seeds: a good quality track ("track-seeded") and/or a topologically clustered jet (TopoJet) ("calo-seeded"). The "track-seeded" approach selects a track with $p_{\mathrm{T}} > 6$ GeV passing some quality criteria. The algorithm then associates other tracks to the seed within a cone of $\Delta R < 0.2$. The tracks are also required to satisfy some quality criteria. If the tau candidate has a total of two tracks, the track criteria are loosened in order

to see if a third track would qualify. The overall charge of the reconstructed three-track candidate must be ± 1.

For the calo-seeded candidate the TopoJet is formed by running a cone-algorithm of radius $\Delta R = 0.4$ over topological clusters. The TopoJet is then required to have $E_\mathrm{T} > 10$ GeV and $|\eta| < 2.5$. Tracks are then associated to the seed if they are within a cone of radius $\Delta R < 0.3$ and pass some minimum quality criteria.

Matching is performed between the track-seeds and the calo-seeds in a cone of radius $\Delta R < 0.2$. If they overlap only one candidate is built.

The track-based algorithm is now run first and if it successfully finds a tau candidate the nearest TopoCluster within $\Delta R < 0.1$ is searched for and the calorimetry-based algorithm is run. The merging of the two algorithms has significantly improved the rejection of background from QCD jets. These new features and updates are implemented in Athena version 14.

The ATLAS Tau Performance Group have also implemented a cut based approach to tau identification, which they believe is "safe" for early data taking [72]. This approach only uses the variables that are expected to be well understood in the early data taking phase. There are two approaches to this: a calorimeter-based approach, which uses only calorimeter variables, and a combined track and calorimeter approach. For each of these approaches three thresholds have been defined: tight, medium and loose. These thresholds correspond to efficiencies of approximately 0.3, 0.5 and 0.7 for candidates reconstructed with the correct track multiplicity matched to true hadronically decaying taus with $E_\mathrm{T} > 10$ GeV and $|\eta| < 2.5$.

Calorimeter-based approach

The calorimeter based approach uses the calo-seed. Four variables are used that are considered safe by calorimeter experts and are not highly correlated. This approach will be particularly useful if there is a problem with the tracker in early

data taking. The EM radius R_{em} as defined in Equation 5.1, the isolation in the calorimeter defined in Equation 5.2 and the transverse energy width in the η-strip layer defined in Equation 5.3 are used, along with the ratio of the EM energy and the total energy. The ratio of the EM energy and the total energy is defined as:

$$\frac{E_{\mathrm{T}}^{\mathrm{EM}}}{E_{\mathrm{T}}^{\mathrm{total}}} = \frac{\sum_i E_{\mathrm{T},i}^{\mathrm{EM}}}{\sum_i E_{\mathrm{T},i}^{\mathrm{EM}} + \sum_j E_{\mathrm{T},j}^{\mathrm{Had}}} \qquad (5.5)$$

The sum runs over all cells in a cone of radius $\Delta R < 0.4$ associated to the tau candidates. $E_{\mathrm{T},i}^{\mathrm{EM}}$ and $E_{\mathrm{T},j}^{\mathrm{Had}}$ are the transverse energies in the EM calorimeter and the hadronic calorimeter respectively. The energies are calibrated using the H1 style calibration.

Combined track and calorimeter based approach

The combined track and calorimeter based approach uses tau candidates seeded using both the calorimeter and tracking variables. It applies selection criteria to the same four variables as the calorimeter based approach but also uses the following variables that involve the tracking:

- **Width of track momenta**: The width of the track momenta $W_{\mathrm{track}}^{\tau}$ is the variance of the tracks in (η, ϕ)-space, weighted with their transverse momenta. For multiple track candidates the width is defined as:

$$W_{\mathrm{track}}^{\tau} = \frac{\sum (\Delta \eta^{\mathrm{track}})^2 \cdot p_{\mathrm{T}}^{\mathrm{track}}}{\sum p_{\mathrm{T}}^{\mathrm{track}}} - \frac{(\sum \Delta \eta^{\mathrm{track}} \cdot p_{\mathrm{T}}^{\mathrm{track}})^2}{(\sum p_{\mathrm{T}}^{\mathrm{track}})^2} \qquad (5.6)$$

  where $\Delta \eta^{\mathrm{track}}$ is the distance between the track and the tau candidate in η. The summation is performed over all tracks associated to the tau candidate.

- $E_{\mathrm{T}}/p_{\mathrm{T}}$ **of the leading track**: This is defined as:

$$\frac{E_{\mathrm{T}}^{\mathrm{total}}}{p_{\mathrm{T}}^{\mathrm{total}}} = \frac{\sum_i E_{\mathrm{T},i}^{\mathrm{calib}}(\mathrm{EM}) + E_{\mathrm{T},i}^{\mathrm{calib}}(\mathrm{Had})}{\sum_{j=1}^{n} p_{\mathrm{T},j}^{\mathrm{track}}}. \qquad (5.7)$$

  The sum in the denominator runs over the transverse momenta $p_{\mathrm{T}}^{\mathrm{track}}$ of all tracks associated to the tau candidates. $E_{\mathrm{T},i}^{\mathrm{calib}}(\mathrm{EM})$ and $E_{\mathrm{T},i}^{\mathrm{calib}}(\mathrm{Had})$ are

the calibrated transverse energies of the cells associated to the tau candidate in the EM and hadronic calorimeters respectively.

- **Fraction of EM energy and sum of total p_T of tracks**:

  This is defined as:

  $$\frac{E_T^{EM}}{p_T^{total}} = \frac{\sum_i E_{T,i}^{EM}}{\sum_{j=1}^n p_{T,j}^{track}}. \tag{5.8}$$

  The numerator is the sum of the transverse energy in all EM calorimeter cells associated to the tau candidate in a cone of $\Delta R < 0.4$, where $E_{T,i}^{EM}$ is the transverse energy after H1 style calibration in cell i. The denominator is the sum of the transverse momenta p_T^{track} of all tracks associated to the tau candidate.

- **Fraction of hadronic energy and sum of total p_T of tracks**: This is defined the same as the fraction of EM energy and sum of total p_T of tracks, except it runs over the hadronic calorimeter cells instead of the EM calorimeter cells. Again a H1 style calibration is applied.

- **Fraction of sum of total p_T of tracks and total energy**: This is defined as:

  $$\frac{p_T^{total}}{E_T^{total}} = \frac{\sum_{k=1}^n p_{T\,k}^{track}}{\sum_i E_{T,i}^{EM} + \sum_j E_{T,j}^{Had}}. \tag{5.9}$$

  The numerator is the sum of the transverse momenta p_T^{track} of the tracks associated to the tau candidates. The denominator contains the sum over all cells associated to the tau candidate in a cone of radius $\Delta R < 0.4$ where $E_{T,i}^{EM}$ and $E_{T,j}^{Had}$ are the transverse cell energies in the EM calorimeter and hadronic calorimeter respectively. Again H1 style calibration is used.

The combined calorimeter and track based approach is expected to perform better since the increased number of variables provide more information on which to base a decision about the tau candidate.

Muon and Electron Vetoes

As well as the above changes, vetoes against muons and electrons have been added to the tau algorithm package in order to reduce the number of electrons and muons wrongly reconstructed as hadronically decaying taus:

Muon Veto A cut-based approach is taken with the muon veto, requiring the energy deposited in the calorimeter by the tau candidate has $E_\mathrm{T} > 5$ GeV [73, 74]. Less than 1% of true hadronic tau decays are lost by this for a mistagging of the isolated muons of 3.3%.

Electron Veto A cut-based approach is also taken for the electrons. Cuts are placed on the ratio of the transverse energy deposited in the EM calorimeter and the track transverse momentum, and on the ratio of high threshold hits to low threshold hits in the TRT for the track. These variables are used since they tend to be higher for electrons than for charged hadrons. The electron veto suppresses electrons from $W \to e\nu$ events by a factor of 60, while retaining 95% efficiency for tau leptons in $W \to \tau^{had}\nu$ [69, 73].

5.7 Object Selection and Overlap Removal Used in This Thesis

The object selection described below was used throughout this thesis. Since the reconstruction algorithms are run independently, they can produce overlapping objects, e.g. a calorimeter cluster could be identified as a jet by the jet finding algorithm and also as an electron by the electron finding algorithm. The cuts used to remove this overlap (overlap removal) are also described below.

5.7.1 Jets

The seeded cone algorithm with a cone size of 0.4 was used to reconstruct jets. The jet algorithm is run on CaloTowers. Jets were selected that had $p_\mathrm{T} > 20$ GeV and $|\eta| < 2.5$. If an electron (passing the object selection described below) and a jet were found within a cone of $\Delta R < 0.2$ then the jet was removed.

5.7.2 Missing Transverse Energy

A refined calibration of the E_T^{miss} known as RefMETFinal was used in this thesis (as described in Section 5.5).

5.7.3 Electrons

The eGamma algorithm was used for the electron identification and reconstruction, using the "medium" purity cuts as recommended by the Electron Performance Group of the ATLAS Collaboration [64]. The transverse isolation energy in a cone of $\Delta R < 0.2$ around the electron, computed using the calorimetric information, was required to be smaller than 10 GeV in order to select isolated electrons. Electrons meeting these requirements were selected if they had $p_T > 10$ GeV and $|\eta| < 2.5$.

In the 14 TeV MC samples the transverse isolation energy in a cone $\Delta R < 0.2$ around the electron was incorrectly calculated, but a significant bias was introduced by this problem only in the region $1.37 < |\eta| < 1.52$ of the detector. Besides the problem with the isolation variable, the electron identification and measurement are degraded in this region due to the large amount of material in front of the calorimeter and the crack between the barrel and extended barrel of the calorimeters [31]. Therefore, for both the 14 TeV and 10 TeV samples, events with an electron reconstructed in this region were rejected.

If an electron was found within a distance $0.2 < \Delta R < 0.4$ of a jet the electron was removed since it is most likely associated with the decay of a particle within the jet.

Performance

A measure of the performance of an algorithm used to identify a physics object is the identification efficiency (also called the reconstruction efficiency). For a physics object of type X, the identification efficiency is defined as the fraction of real objects of type X that are reconstructed as objects of type X. Figure 5.2

shows the electron efficiency as a function of the true p_T (left) and the true η (right) for leptonically decaying $t\bar{t}$-pairs (T1) and an example SUSY signal (SU3), using the 14 TeV MC samples. The T1 and SU3 samples were chosen to show the efficiency in a busy environment (since both of these processes can involve several jets and a number of leptons). As a function of p_T the electron efficiency increases to a plateau around 40 GeV. Above 40 GeV the efficiency is around 70%. As a function of η the performance mirrors the geometry of the detector, showing an efficiency of around 80% in the barrel region (below $|\eta| = 1.4$). The efficiency drops to approximately 60% in the end-cap region and drops even further near the cracks ($|\eta| = 1.45$). A drop in efficiency can also been seen for the half-barrel transition at $\eta = 0$. Both samples show a similar behaviour in efficiency.
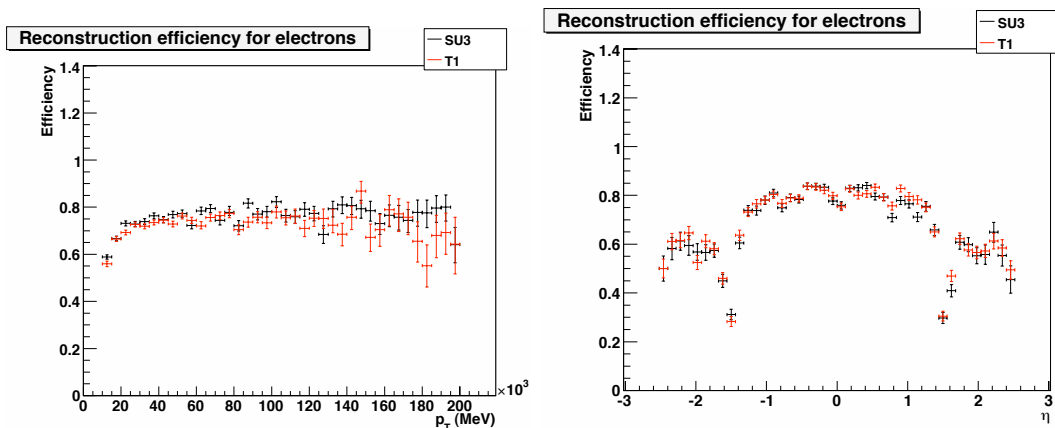
Figure 5.2: The identification efficiency of isolated electrons as a function of p_T (left) and η (right) for leptonically decaying $t\bar{t}$-pairs (T1) and an example SUSY signal (SU3) using the 14 TeV MC Samples. Taken from Ref. [58].

Figure 5.3 shows the electron efficiency as a function of p_T (left) and η (right) for leptonically decaying $t\bar{t}$, $Z \to ee$ and $W \to e\nu$ events using the 10 TeV MC samples. The efficiency is defined here as the fraction of true electrons with $p_T > 20$ GeV and $|\eta| < 2.5$ reconstructed as electrons with $p_T > 30$ GeV and $|\eta| < 2.5$. The reason for this choice will be explained in Chapter 7. Again the electron efficiency rises to a plateau in the distribution of efficiency as a

function of p_T. The plateau occurs around 50 GeV with an efficiency of $\sim 80\%$. The efficiency as a function of η again reflects the geometry of the detector. It appears slightly lower than the efficiency as a function of p_T with an efficiency of $\sim 60\%$. This is an artifact of the particular phase space definitions used for the efficiency here. Due to the p_T cut placed on the electrons. If a true electron with a p_T of 20 GeV is reconstructed with a p_T of 21 GeV it doesn't enter the η distribution since the p_T of the reconstructed electron is required to be greater than 30 GeV.
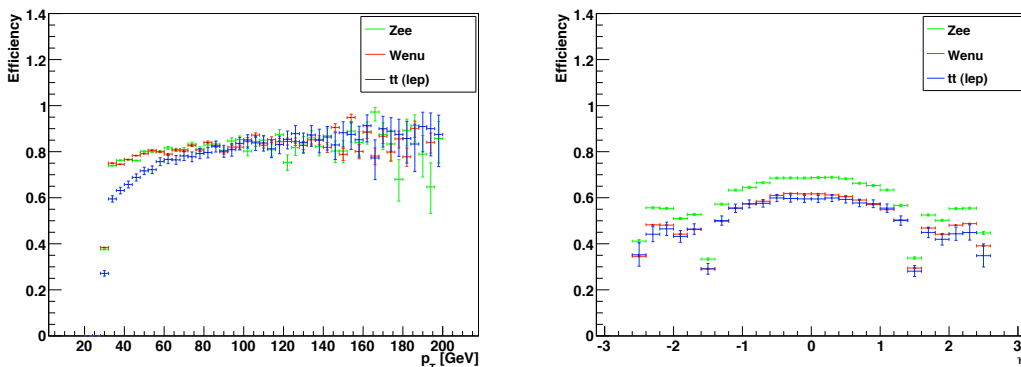
Figure 5.3: The identification efficiency of isolated electrons as a function of p_T (left) and η (right) for leptonically decaying $t\bar{t}$, $Z \rightarrow ee$ and $W \rightarrow e\nu$ events using the 10 TeV MC Samples. True electrons are required to have $p_T > 20$ GeV and $|\eta| < 2.5$, reconstructed electrons are required to have $p_T > 30$ GeV and $|\eta| < 2.5$.

5.7.4 Muons

The standard STACO algorithm was used to reconstruct muons. The algorithm performs a statistical combination of a track reconstructed in the Muon Spectrometer with its corresponding track in the Inner Detector. A reasonable quality of combination was guaranteed with a loose requirement that the tracks should match with $\chi^2 < 100$. If more than one track in the Inner Detector matched a track from the Muon Spectrometer, only the one with best match (smallest ΔR) was kept. In addition, the total calorimeter energy deposited in a cone of

$\Delta R < 0.2$ around the muon was required to be less than 10 GeV. Muons meeting these requirements were selected if they had $p_T > 10$ GeV and $|\eta| < 2.5$.

If a muon was found within a distance $\Delta R < 0.4$ of a jet it was discarded since it is likely to have been produced by the decay of a particle inside the jet.

Performance

Figure 5.4 shows the reconstruction efficiency of the muons as a function of p_{T} (top) and η (bottom) for the example SUSY sample (SU3) (left) and the leptonically decaying $t\bar{t}$ (T1) (right). The plots were produced using the 14 TeV MC samples. It can be seen that the muon reconstruction performs very well. The distributions are mostly flat with an efficiency of around 90% for both samples. The detector geometry is reflected in the η distributions, similar to the η distributions for the electrons, though the reductions in efficiency are not as severe.

Figure 5.5 shows the muon efficiency for leptonically decaying $t\bar{t}$, $Z \to \mu\mu$ and $W \to \mu\nu$ events as a function of p_{T} (left) and η (right) using the 10 TeV MC samples. The efficiency is defined here as the fraction of true muons with $p_{\mathrm{T}} > 20$ GeV and $|\eta| < 2.5$ reconstructed as muons with $p_{\mathrm{T}} > 30$ GeV and $|\eta| < 2.5$. The reason for this choice will be explained in Section 7. Again the efficiency distribution is mostly flat as a function of p_{T} with an efficiency of $\sim 90\%$. The distribution in η is also mostly flat except for the drops in efficiency reflecting the detector geometry. The efficiency is slightly lower in η ($\sim 70\%$). As explained above for the electrons, this is an artifact of the particular phase space definitions used for the efficiency here. Due to the p_{T} cut placed on the muons. If a true muon with a p_{T} of 20 GeV is reconstructed with a p_{T} of 21 GeV it doesn't enter the η distribution since the p_{T} of the reconstructed muon is required to be greater than 30 GeV.

5.7.5 Taus

Due to the developments in the tau algorithm over the period of time taken to perform the studies for this thesis, different definitions were taken for the tau
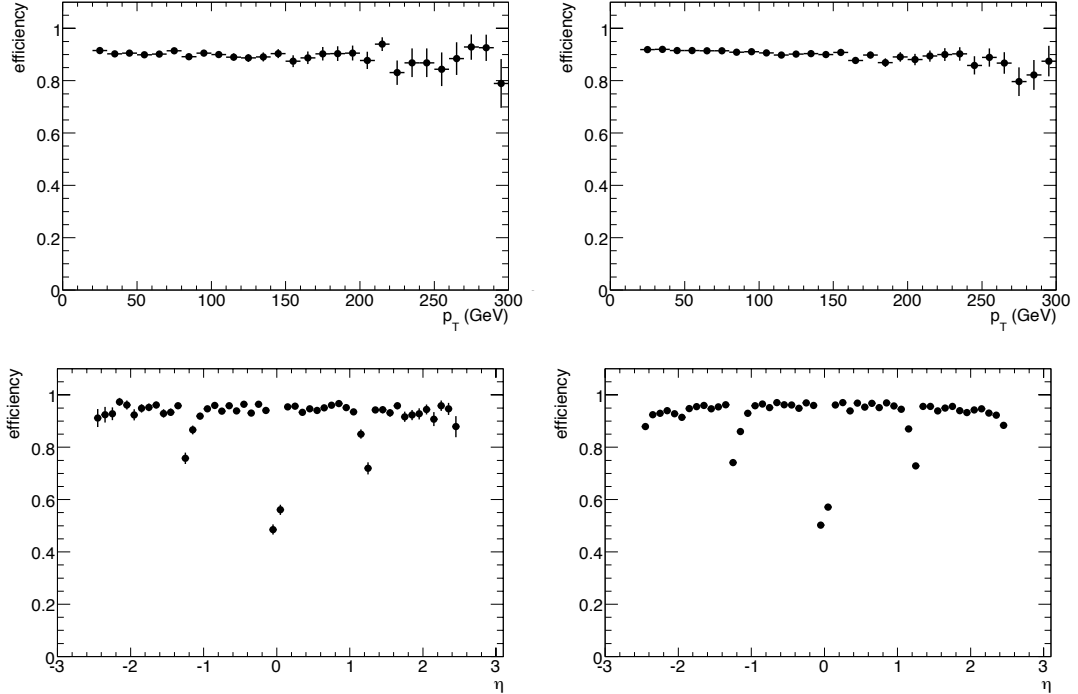
Figure 5.4: The identification efficiency of muons as defined in the text as a function of p_T (top) and η (bottom) for the SU3 SUSY sample (left) and the T1 leptonic top sample (right). Muon $p_T > 20$ GeV was required. The plots were produced using the 14 TeV MC samples. Taken from Ref. [58].

when using the 14 TeV and 10 TeV MC samples. The 14 TeV MC samples were reconstructed with Athena version 12.0.6, which contained the older tau algorithms. The 10 TeV MC samples were reconstructed with Athena version 14.5.1 containing the improved tau algorithms.

5.7.5.1 Taus in the 14 TeV Monte Carlo Samples

The "TauRec" algorithm was used to reconstruct taus with a likelihood discriminant of 4 as recommended by the ATLAS Tau Performance Group [69]. Taus meeting these requirements were selected if they had $p_T > 20$ GeV and $|\eta| < 2.5$.
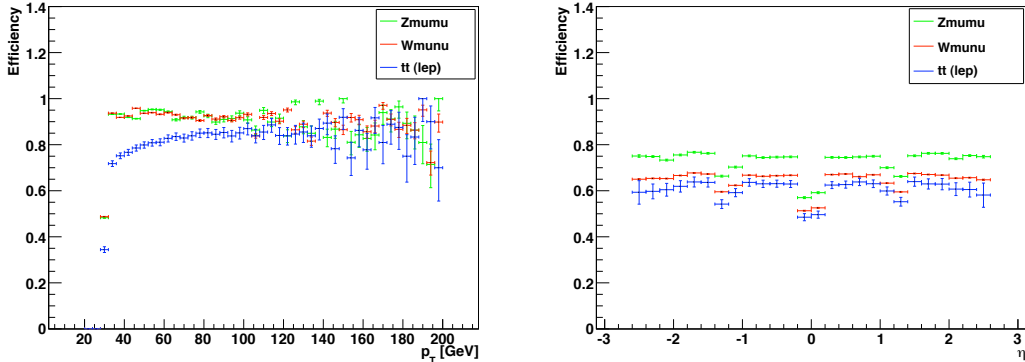
Figure 5.5: The identification efficiency of muons as a function of p_T (left) and η (right) for leptonically decaying $t\bar{t}$, $Z \to \mu\mu$ and $W \to \mu\nu$ events using the 10 TeV MC samples. True muons are required to have $p_T > 20$ GeV and $|\eta| < 2.5$, reconstructed muons are required to have $p_T > 30$ GeV and $|\eta| < 2.5$.

Performance

Figure 5.6 shows the reconstruction efficiency of the taus as a function of visible p_T (left) and η for two example SUSY signals (SU3 and SU6) and the processes $Z \to \tau\tau$, $W \to \tau_{had}\nu$ and leptonically decaying $t\bar{t}$ pairs. The SUSY signals and the leptonically decaying top sample provide examples of busy environments where several jets and a number of leptons can be present, whereas $Z \to \tau\tau$, $W \to \tau_{had}\nu$ provide examples of relatively clean environments. It can be seen that there is a strong dependence on p_T with a sharp increase in efficiency at lower p_T, a peak around 40-60 GeV and then a moderate fall with increasing statistical uncertainties. The distribution is approximately flat in η to within a few percent and again the detector geometry is reflected in the distribution.

For the different samples the overall behaviour is similar except for a small increase in efficiency at high η for $Z \to \tau\tau$, $W \to \tau_{had}\nu$ mainly due to the samples having a higher contribution of real taus with intermediate p_T values in this region compared to the other samples. The cleaner samples ($Z \to \tau\tau$, $W \to \tau_{had}\nu$) have higher efficiencies overall compared to the busier samples (SU3, SU6, and $t\bar{t}$). This is because it is more difficult to reconstruct a tau in a busier environ-

86
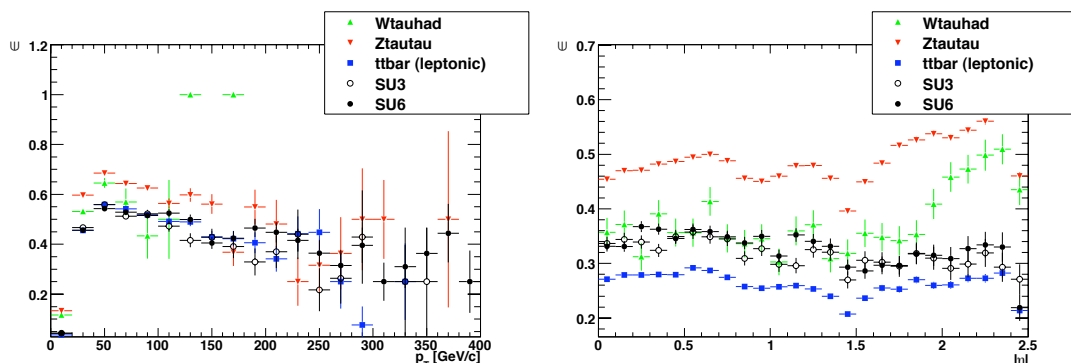
Figure 5.6: The reconstruction efficiency of the tau as a function of the visible p_T (left) and $|\eta|$ (right) for two example SUSY signals (SU3 and SU6) and the processes $Z \to \tau\tau$, $W \to \tau_{had}\nu$ and leptonically decaying $t\bar{t}$-pairs. The 14 TeV MC samples were used. Taken from Ref. [58].

ment where more QCD jets are present providing a higher background to the tau reconstruction. Figure 5.7 shows the mean efficiencies of the taus after asking that they have $p_T > 40$ GeV, for the different samples. This reiterates the dependence of the efficiency on the complexity of the environment.
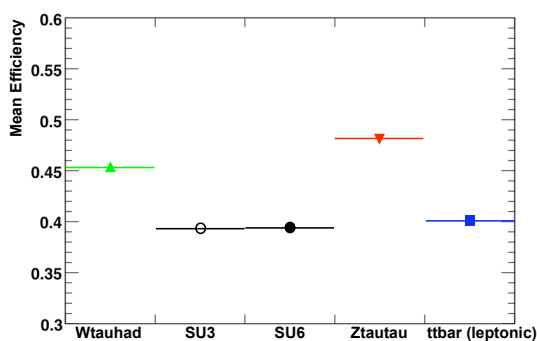
Figure 5.7: The mean reconstruction efficiency of the tau for two example SUSY signals (SU3 and SU6) and the processes $Z \to \tau\tau$, $W \to \tau_{had}\nu$ and leptonically decaying $t\bar{t}$-pairs. Taus were required to have $p_T > 40$ GeV. The 14 TeV MC samples were used.

Another useful quantity for measuring the performance of an algorithm is the

purity. In this case the purity is defined as the fraction of reconstructed taus that are matched to true taus. Figure 5.8 shows the purity of the taus as a function of p_T (left) and η (right). Again there is a dependence on the complexity of the environment. Cleaner processes have a higher purity (around 90%) whereas busier environments have lower purities. The purity of the leptonic top sample is low compared to the other busy samples (SU3 and SU6). This is due to the fraction of real taus in the sample being lower, since $t\bar{t}$ decays to muon and electron final states are included. Reconstructed taus from these events will be fake and will thus lower the purity.
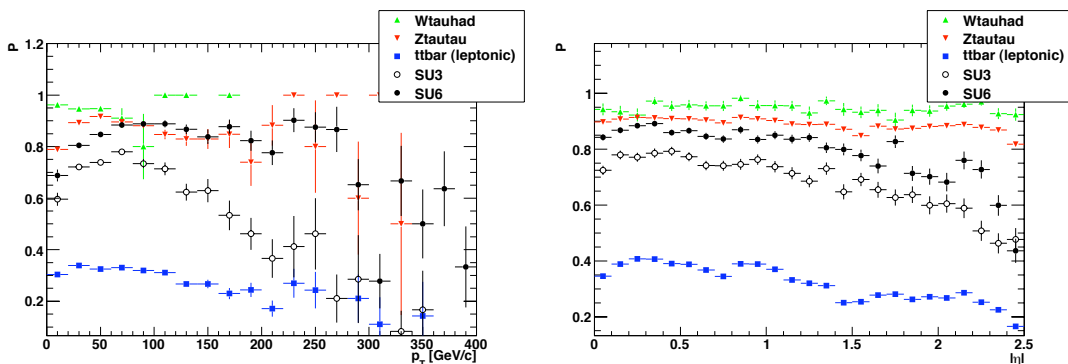
Figure 5.8: The purity of the taus as a function of the visible p_T (left) and η (right) for two example SUSY signals (SU3 and SU6) and the processes $Z \rightarrow \tau\tau$, $W \rightarrow \tau_{had}\nu$ and leptonically decaying $t\bar{t}$-pairs. The 14 TeV MC samples were used. Taken from Ref. [58].

5.7.5.2   Taus in the 10 TeV Monte Carlo Samples

The new algorithm combining tauRec and tau1p3p was used to reconstruct taus in the 10 TeV Monte Carlo Samples. Both the medium and tight safe cuts defined by the ATLAS Tau Performance Group were investigated (see Chapter 8). The number of tracks was required to be one or three. The tau charge was required to be one. Taus meeting these requirements were selected if they had $p_T > 20$ GeV and $|\eta| < 2.5$. In order to reduce the number of fake taus from misreconstructed electrons and muons, the electron and muon vetos designed by the Tau Performance Groups were also investigated (see Chapter 8).
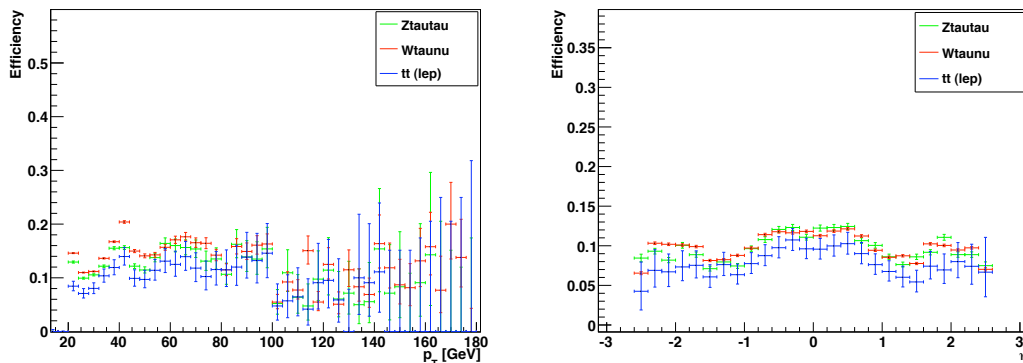
Figure 5.9: The identification efficiency of taus as a function of p_T (left) and η (right) for leptonically decaying $t\bar{t}$, $Z\rightarrow \tau\tau$ and $W \rightarrow \tau\nu$ events using the 10 TeV MC samples. True taus are required to have $p_T > 15$ GeV and $|\eta| < 2.5$, reconstructed taus are required to have $p_T > 20$ GeV and $|\eta| < 2.5$. The tight safe cuts were used for the taus.

Figure 5.9 shows the tau efficiency for leptonically decaying $t\bar{t}$, $Z\rightarrow \tau\tau$ and $W \rightarrow \tau\nu$ events as a function of p_T (left) and η (right) using the 10 TeV MC samples. The efficiency is defined here as the fraction of true hadronically decaying taus with $p_T > 15$ GeV and $|\eta| < 2.5$ reconstructed as taus with $p_T > 20$ GeV and $|\eta| < 2.5$ and the tight safe cuts are used. It can be seen that, as in the 14 TeV MC samples, the efficiency for the busier $t\bar{t}$ sample is lower than the efficiencies of the clean samples ($Z \rightarrow \tau\tau$ and $W \rightarrow \tau\nu$). The bumps in the distribution of the efficiency as a function of p_T are an artifact of the optimization of the algorithm which is performed in bins of p_T. The efficiency is lower than what was seen in the 14 TeV samples. This is a result of the tight safe cuts, which are quite harsh.

5.7.5.3 Overlap Removal

The same tau overlap removal was used for both sets of MC data. If a tau was found within $\Delta R < 0.4$ of an electron it was removed since the electron identification efficiency is higher than the tau identification efficiency and so the object is more likely to be an electron. Also, since hadronically decaying taus are reconstructed as jets, when a calorimeter jet was found within $\Delta R < 0.4$ of a

reconstructed tau, then the jet was removed. If a tau was found within $\Delta R < 0.4$ of a muon, the muon was removed.

5.7.6 Corrections for ATLFAST1

Due to its very simplified detector simulation ATLFAST1 tends to reconstruct objects more efficiently than the full simulation. A number of corrections were made to the efficiencies of different physics objects in order to ensure that the performance of the reconstruction of the physics objects in ATLFAST1 samples correctly matched the performance observed using full simulation samples.

5.7.6.1 Electron Correction

Figure 5.10 shows a comparison of the reconstruction efficiency of electrons in full simulation and ATLFAST1 samples, as a function of p_{T} for the SU3 SUSY signal (left) and as a function of η for the process $Z \to ee$ (right) using the 14 TeV MC samples. It also shows the ATLFAST1 sample once the electron correction has been applied. It can be seen that this more accurately follows the performance of the full simulation.
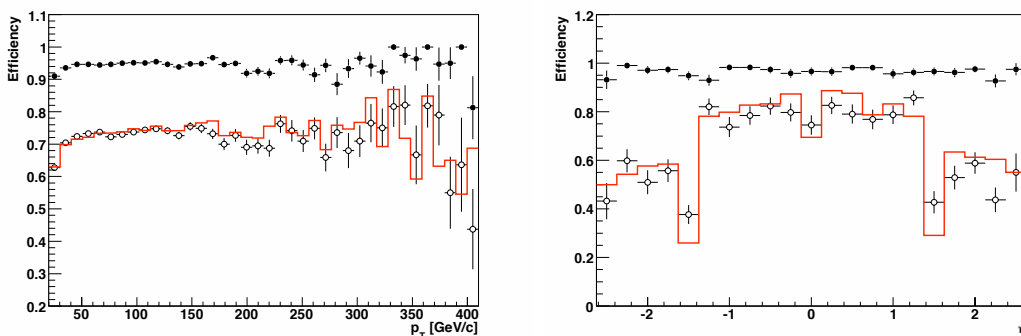
Figure 5.10: Efficiencies for electrons as a function of p_{T} for the SU3 sample (left) and η for the process $Z \to ee$ (right) – red line: FULLSIM; black dots: uncorrected ATLFAST; open dots: corrected ATLFAST. The 14 TeV MC samples were used. Taken from Ref. [75].

The efficiency correction is described in detail in Ref. [75, 76]. Briefly, the efficiency was corrected using the following correction factor:

$$f_{\text{corr}}(p_{\text{T}}, \eta) = \frac{\varepsilon_{\text{FULL}}(p_{\text{T}}, \eta)}{\varepsilon_{\text{FAST}}(p_{\text{T}}, \eta)} \tag{5.10}$$

where $\varepsilon_{\text{FULL}}$ and $\varepsilon_{\text{FAST}}$ are the efficiencies of the uncorrected fast and full simulation respectively. A random number x was generated between 0 and 1 for every electron. If $x > f_{\text{corr}}(p_{\text{T}}, \eta)$ and $f_{\text{corr}}(p_{\text{T}}, \eta) < 1$ the electron was removed.

The p_{T} spectrum of the electrons was corrected using the relative resolution:

$$\frac{p_{\text{TFAST}} - p_{\text{TFULL}}}{p_{\text{TFULL}}} \tag{5.11}$$

where p_{TFAST} and p_{TFULL} are the p_{T} of the ATLFAST1 object and the corresponding object in full simulation respectively. Spectra of the relative resolution were constructed in bins of p_{T} and η. PDFs for the final p_{T} correction were obtained by normalizing the spectra to 1. The correction was then applied by generating a random number b according to the PDFs. The p_{T} of the corrected object is recalculated as $p_{\text{Tcorr}} = (1 + b)p_{\text{T}}$.

5.7.6.2 Jet Correction

During the simulation using ATLFAST1, the merging-splitting algorithm that prevents overlap between jets was turned off. As a result, one truth jet can be reconstructed as several jets sharing the energy of the truth jet. To correct this, ATLFAST1 jets that were matched to the same truth jet were merged by adding their four vectors. Figure 5.11 shows the reconstruction efficiency of the jets as a function of p_{T} and η using full simulation and using the corrected ATLFAST1. It can be seen that this merging is sufficient to obtain good agreement between the ATLFAST1 jets and the jets in full simulation.

5.7.6.3 Tau Correction

The tau finding efficiency in ATLFAST1 was found to be 30% higher compared to full simulation, reasonably independent of p_{T} and η. To correct this in the
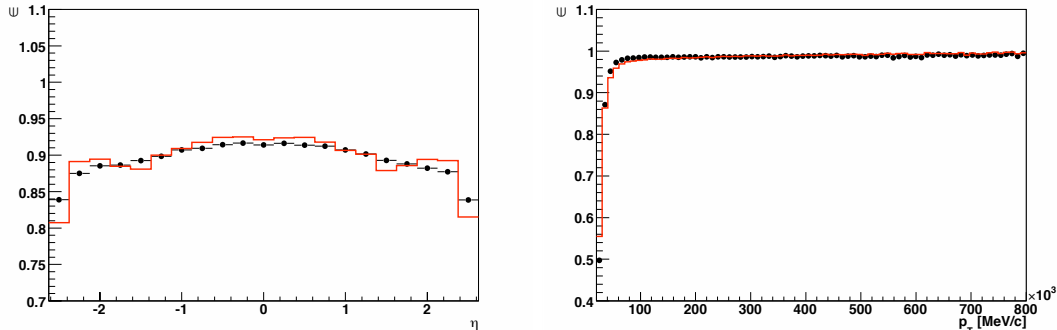
Figure 5.11: Efficiencies for jets from the SU3 sample as a function of p$_T$ (left) and η (right) - red line: FULLSIM; black dots: corrected ATLFAST (only merged). The 14 TeV MC samples were used. Taken from Ref. [58].

ATLFAST1 samples, for every reconstructed tau with $p_{\mathrm{T}} > 40$ GeV that was matched to a true tau, a random number x was generated between 0 and 1 and if x was found to be less than 0.3 the tau was discarded. Since overlap removal with jets had been performed, care was taken to re-include the jets that were previously found to be overlapping with a tau that was then removed by this correction. Figure 5.12 shows the reconstruction efficiency of the taus as a function of η for the SUSY point SU6, for full simulation and for the corrected ATLFAST1. It can be seen that this correction is sufficient to obtain good agreement between the ATLFAST1 taus and the taus in full simulation.
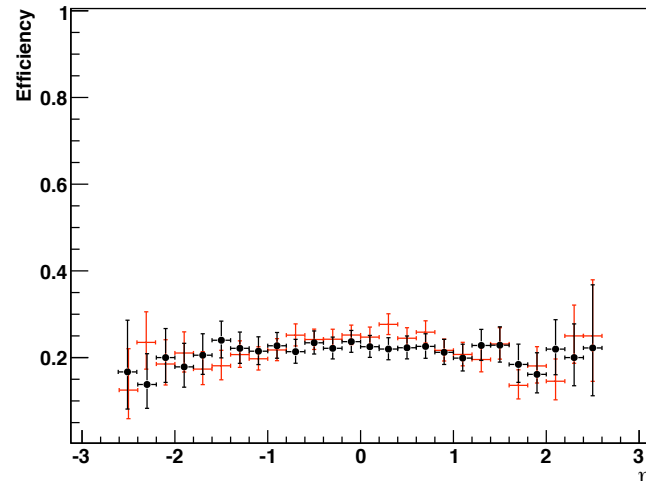
Figure 5.12: Efficiencies for taus from the SU6 sample as a function of η - red points: full simulation; black dots: corrected ATLFAST1. The 14 TeV MC samples were used.

Chapter 6

Inclusive Search For Supersymmetry Using Taus

The work for this chapter was carried out as part of the ATLAS Collaboration Computing System Commissioning (CSC) studies [53] studies and is published in Ref. [75]. A more detailed account is also given in the ATLAS internal note Ref. [58].

6.1 Introduction

6.1.1 Production of Supersymmetric Particles at the LHC

If R-parity is conserved supersymmetric particles will be produced in pairs in parton collisions at the LHC. Charginos, neutralinos and sleptons will be produced via the weak interaction from quark-antiquark annihilation as shown in Figure 6.1, whilst squark and gluinos will be produced via the strong interaction from gluon-gluon and quark-gluon fusion as demonstrated in Figure 6.2 as well as from quark-antiquark annihilation and quark-quark scattering as demonstrated in Figure 6.3.

The production cross-sections of these processes depend on the PDFs at the energy scale (Q^2) of the hadron collider and the mass spectrum of the sparticles.
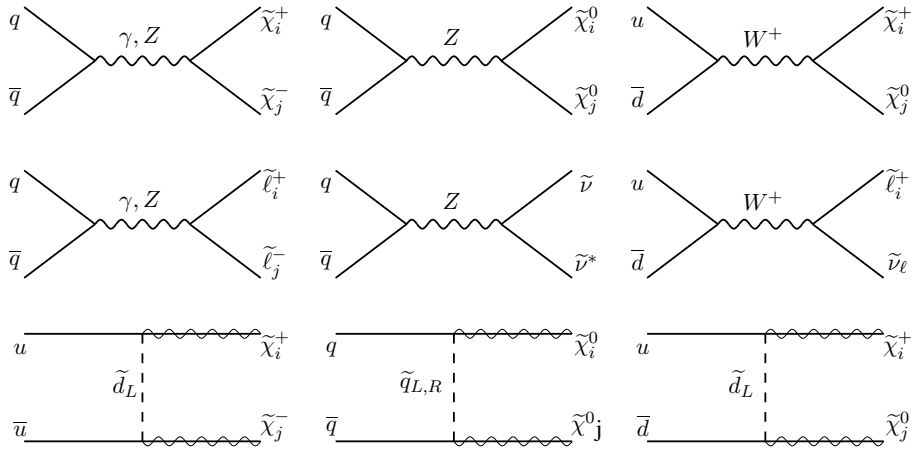
Figure 6.1: LO feynman diagrams for the electroweak production of sparticles from quark-antiquark annihilation at the LHC. Taken from Ref. [4].
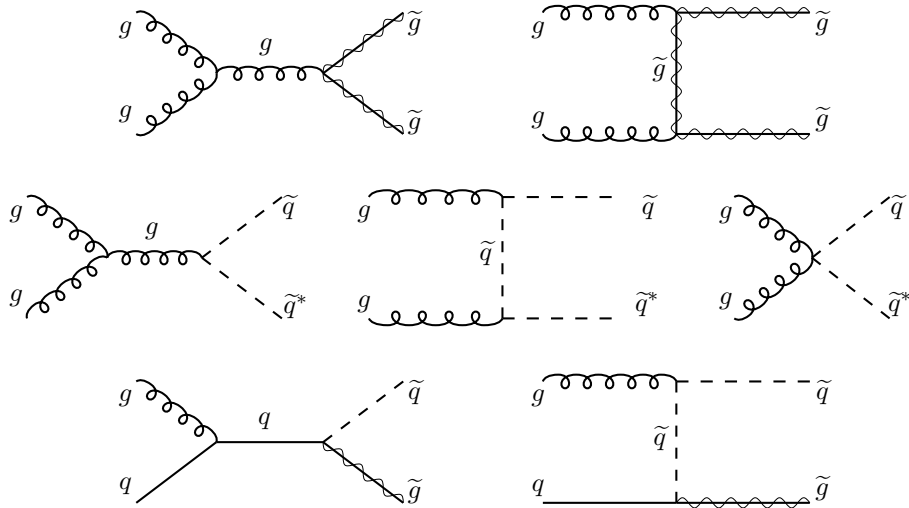
Figure 6.2: LO feynman diagrams for the production of squarks and gluinos from gluon-gluon and quark-gluon fusion at the LHC. Taken from Ref. [4].
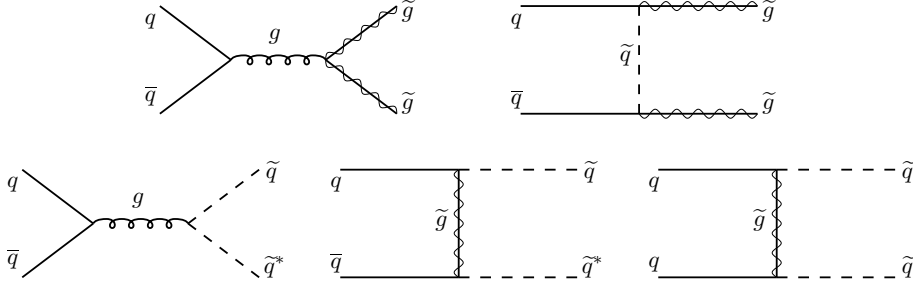
Figure 6.3: LO feynman diagrams for the production of squarks and gluinos from quark-antiquark annihilation and quark-quark scattering at the LHC. Taken from Ref. [4].

If their mass is in the TeV range, squarks and gluinos will dominate the SUSY production at the LHC.

6.1.2 Cascade Decays of Squarks and Gluinos

If it is kinematically allowed, the dominant decay of squarks will be via $\tilde{q} \to q\tilde{g}$. Otherwise squarks will decay into neutralinos and charginos via $\tilde{q} \to q\tilde{\chi}_i^0$ and $\tilde{q} \to q'\tilde{\chi}_i^\pm$ respectively [4]. Direct decays of the squark to the LSP $\tilde{q} \to q\tilde{\chi}_1^0$ are kinematically favoured. Such decays may be dominant for right-handed squarks but left-handed squarks may favour decays to heavier charginos and neutralinos. In this case the chargino or neutralino will in turn decay, and its daughters decay until a final state containing the LSP is reached. This results in decay chains known as cascade decays.

Gluino decay can only proceed via squarks, either on-shell or virtual. If the gluino is heavier than the squarks the two-body decay $\tilde{g} \to q\tilde{q}$ will dominate. If instead the squarks are heavier than the gluino, the gluino will decay through off-shell squarks $\tilde{g} \to qq\tilde{\chi}_i^0$ and $\tilde{g} \to qq'\tilde{\chi}_i^\pm$ [4]. The squarks, neutralinos and charginos in these final states will decay as described above leading to cascade decays. Figure 6.4 demonstrates some of the possible gluino cascade decays ending with a neutralino LSP.
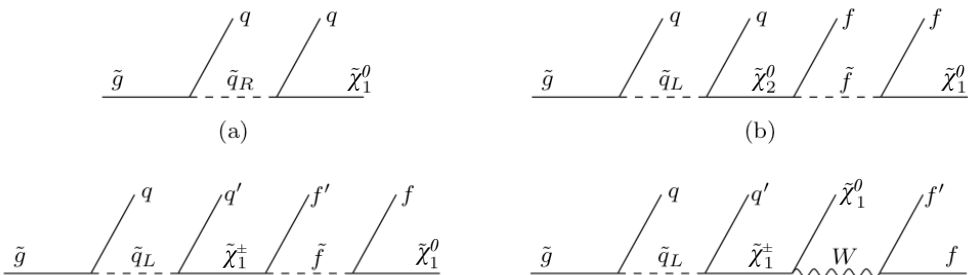
Figure 6.4: Some examples of the possible gluino cascade decays to a neutralino LSP. The squarks in the diagrams may be either on-shell or off-shell depending on the mass spectrum of the SUSY model. Taken from Ref. [4].

6.1.3 The Search Strategy of the ATLAS Collaboration

As can be inferred from Figure 6.4, cascade decays of squarks and gluinos lead to events with a number of high p_T jets, a number of leptons, and large E_T^{miss} as a result of the LSPs escaping detection. The search strategy of the ATLAS Collaboration focuses on these signatures. Two approaches are taken:

- **Inclusive searches**: The inclusive search strategy used by ATLAS concentrates on this signature of high p_T jets, a number of leptons and large E_T^{miss}, and looks for an excess of events with respect to the Standard Model.

- **Exclusive searches**: Once a sample of events has been found where SUSY is present, the exclusive searches isolate specific processes in an attempt to measure sparticle masses and subsequently determine which particular SUSY model is realised in nature.

This thesis will concentrate on the inclusive search strategy. This strategy is twofold. First a number of specific SUSY benchmark points are selected with a particular choice of parameters. Fully simulated Monte Carlo samples are produced for these signals and for the SM backgrounds. Using these benchmark points, inclusive search channels are defined and their performance studied to determine how best to reconstruct these events and separate the SUSY signal from the SM Backgrounds.

Second, since there is no reason to believe that these benchmark points are representative of the particular SUSY model realised in nature, thousands of points in the SUSY parameter space, for several different models, are generated using a fast paramterisation of the ATLAS detector. Using the insight gained by studying the benchmark points, scans are then made of the performance of each inclusive search channel at each of these points. The goal is to verify that the inclusive channels defined using the benchmark points provide sensitivity to a wide range of SUSY models and thus develop a general search strategy covering as wide a range of models as possible.

Detailed studies have been carried out for a broad spectrum of channels including channels with different jet multiplicites (1, 2, 3, 4 jets) and different lepton multiplicities (0, 1, 2, 3 leptons). These studies are detailed in Ref. [58, 75].

6.1.4 Motivation for Inclusive Searches Involving Taus

At the time of starting the work for this thesis the only lepton channels considered in the inclusive searches by the ATLAS Collaboration were those involving electrons and muons. This chapter looks at the potential of extending the lepton channels to include taus.

There are two reasons for trying to extend the lepton channels to include taus. The first is simply an effort to extend the number of channels that are available to look for SUSY, increasing the sensitivity of the ATLAS Collaboration's search for SUSY. The second reason is that in both gauge-mediated and gravity-mediated SUSY models one readily finds regions of parameter space where tau final states are enhanced over final states with electrons or muons, providing a possible indication of new physics [74, 77].

The dominance of the tau in these regions of parameter space comes from the fact that it is the heaviest lepton and thus has the largest leptonic Yukawa coupling. The large Yukawa coupling has two important consequences in mSUGRA models. The first is that due to the renormalisation group equations, the lighter $\tilde{\tau}_1$ is the

lightest slepton. If the tau Yukawa coupling is large the renormalization group effects will drive $\tilde{\tau}_R$ below $\tilde{l}_R$. The $\tilde{\tau}$ mass matrix can also have a large mixing proportional to the Yukawa coupling [77]:

$$\lambda_\tau \simeq \frac{m_\tau \tan\beta}{v} \tag{6.1}$$

where $v = 174$ GeV, driving the lightest eigenvalue down, resulting in $m_{\tilde{\tau}_1} \ll m_{\tilde{l}_R}$. This is enhanced in regions of parameter space with large $\tan\beta$.

On-shell decays to $\tilde{\tau}_1$ will be more likely than to $\tilde{l}_R$ if the sleptons are lighter than $\tilde{\chi}_1^\pm$ and $\tilde{\chi}_2^0$, increasing the production of staus and thus taus (from the decay of the staus) with respect to the other leptons in cascade decays of squarks and gluinos [77].

The second consequence, is that substantial mixing introduces a large $\tilde{\tau}_L$ component to $\tilde{\tau}_1$ unlike $\tilde{e}_1$ and $\tilde{\mu}_1$, which are predominantly $\tilde{e}_R$ and $\tilde{\mu}_R$ respectively [77]. As a result the $\tilde{\tau}_1$ couples more effectively to $\tilde{\chi}_1^\pm$ and $\tilde{\chi}_2^0$ than the mostly R-type $\tilde{e}_1$ and $\tilde{\mu}_1$, since $\tilde{\chi}_1^\pm$ and $\tilde{\chi}_2^0$ are mostly $SU(2)_L$ gauginos in mSUGRA models. Interactions with Higgsinos are also enabled due to the large tau Yukawa coupling, which are negligible for the $\tilde{e}$ and $\tilde{\mu}$.

6.2   Experimental Setup

6.2.1   Monte Carlo Samples

The Monte Carlo samples used in this study were produced with Athena release 12.0.6 in the context of the Computing System Commissioning (CSC) studies [53]. The samples were produced with a centre-of-mass energy of 14 TeV and are detailed in Section 4.4.1.

6.2.2   Trigger

Due to the rich topology expected in SUSY events and the strong cuts in this analysis (see Section 6.3) the trigger efficiency is expected to be high. The same

triggers will be used as in the ATLAS inclusive SUSY search that looks for a final state of at least four jets and $E_\mathrm{T}^\mathrm{miss}$ (known as the 0-lepton mode). As part of the CSC studies [75], the trigger efficency was studied for the 0-lepton mode using a complete simulation of all three trigger levels. The trigger thresholds defined for 2×10^{33} cm^{-2}s^{-1} in the High Level Trigger TDR [78] were adopted. A combined jets and $E_\mathrm{T}^\mathrm{miss}$ trigger was studied, known as $j70\_xE70$. $E_\mathrm{T}^\mathrm{miss} > 70$ GeV accompanied by a jet with $p_\mathrm{T} > 70$ GeV is required by this trigger. The trigger is not prescaled. Table 6.1 shows the trigger efficiencies using this trigger for the 0-lepton analysis for the SU3 and SU6 SUSY benchmark points (defined in Section 4.4.1.1). The trigger considered here is quite basic, more complex triggers combining different objects can also be implemented. But even with this basic trigger, the trigger efficiency for the tau analysis is expected to be above 95%.

Trigger	SU3	SU6
Jets+$E_\mathrm{T}^\mathrm{miss}$	99.5	99.6

Table 6.1: Average event trigger efficiency (in %) for events passing the combined jets and $E_\mathrm{T}^\mathrm{miss}$ trigger (described in the text) for the 0-lepton analysis. Numbers taken from Ref. [75]

6.2.3 Object Selection and Overlap Removal

The object selection and overlap removal used in this analysis are detailed in Section 5.7.

6.2.4 Global Event Variables

The following event variables were used in this analysis:

Effective Mass The effective mass M_{eff} is a variable commonly used in SUSY searches to discriminate SUSY events from SM events. It is a measure of the

total activity in an event and is defined as:

$$M_{eff} \equiv \sum_{i=1} p_{\mathrm{T}}^{jet,i} + \sum_{j=1} p_{\mathrm{T}}^{lep,j} + E_{\mathrm{T}}^{\mathrm{miss}} \tag{6.2}$$

where the number of jets and leptons can be specified according to its use. M_{eff} has the property that for SUSY events, the distribution peaks at a value strongly correlated with the mass of the pair of SUSY particles produced in the proton-proton interaction. It can therefore be used to quantify the mass-scale of SUSY events [58].

Transverse Mass   The transverse mass M_{T} is defined as the invariant mass of the lepton and the $E_{\mathrm{T}}^{\mathrm{miss}}$ in the transverse plane:

$$M_T = \sqrt{2 \times p_{\mathrm{T}}^{lep} \times E_{\mathrm{T}}^{\mathrm{miss}} \times (1 - \Delta\phi(lep, E_{\mathrm{T}}^{\mathrm{miss}}))}. \tag{6.3}$$

It is a particularly useful variable for suppressing background from W events. For a W boson decay the $E_{\mathrm{T}}^{\mathrm{miss}}$ is due to one neutrino and both the neutrino and lepton come from the decay of the W. The transverse distribution for these events shows a characteristic edge near to the mass of the W boson.

6.3   Event Selection

6.3.1   Inclusive four-jet final states

The signature for this analysis is a number of high p_{T} jets, $E_{\mathrm{T}}^{\mathrm{miss}}$ and a number of taus from the cascade decays of squarks and gluinos. The aim of this analysis is to search for events with such a final state in the data and then remove those events that are from SM backgrounds, isolating the SUSY signal.

SM backgrounds come from those physics processes that produce or fake the signature being searched for. The main backgrounds that dominate this analysis are:

- **QCD multijets**: QCD jet reconstruction may introduce fake E_T^{miss} to the event due to the limitations of the calorimeter and the algorithm used for reconstruction, which cannot be fully corrected for. In addition, heavy flavour jets may decay semileptonically, and both light and heavy flavour jets may be misidentified as taus leading to events that appear to have taus, high p_T jets and E_T^{miss}.

- $t\bar{t}$ **pairs**: If a $t\bar{t}$ pair decays semileptonically, it will produce a number of high p_T jets, E_T^{miss} and a number of leptons (as described in Section 1.1.3) thus producing the same signature as the SUSY signal being searched for.

- W+**jets**: W decay to a tau in association with jets will also produce the same signature as the signal.

In order to introduce an inclusive analysis using taus and allow comparisons to the search analyses already employed by the ATLAS Collaboration, an effort was made to use the same baseline selection as these analyses (outlined in Ref. [79]). Some cuts particularly useful to this analysis were then included on top of this baseline. The following event selection cuts were applied in order to select the SUSY signal and isolate it from the SM backgrounds:

- Cut 1: At least four jets with the hardest jet having $p_T > 100$ GeV and the next three jets having $p_T > 50$ GeV.

- Cut 2: $E_T^{miss} > 100$ GeV

- Cut 3: $\Delta\phi(j_i, E_T^{miss}) > 0.2$ for each of the three leading jets j_i, $i = 1, 2, 3$.

- Cut 4: No isolated leptons

- Cut 5: At least one tau $p_T > 40$ GeV

- Cut 6: $E_T^{miss} > 0.2 M_{eff}$

- Cut 7: $M_T > 100$ GeV

where M_{eff} is defined in this case as the sum of the p_T of the four hardest jets, the hardest tau and the E_T^{miss}.

To model the possible SUSY signal two benchmark points, SU3 and SU6, were chosen. These points are described in Section 4.4.1.1. Since the presence of taus in supersymmetry scenarios is highly correlated with $\tan\beta$, SU3 ($\tan\beta = 6$) was chosen to represent a low $\tan\beta$ scenario and SU6 ($\tan\beta = 50$) was chosen to represent a high $\tan\beta$ scenario. The specific details of the points are not important here as the aim is to produce an analysis that is suitable for a wide range of possible SUSY signals, not one that is optimised to one particular point.

The resulting cutflow for 1 fb^{-1} of integrated luminosity is given in Table 6.2. Figure 6.5 shows the effect of the cuts on the distribution of the effective mass when successively applied.

Sample	Events	Cut1-2	Cut3	Cut4	Cut5	Cut6	Cut7
SU3	27318	8867	8024	6541	635	482	259
SU6	5987	2312	2088	1625	259	204	119
Top	820358	11787	9799	6604	544	326	45
QCD	1337767	24686	5252	5245	14	0	0
Z+jets	14420	1535	1298	1257	18	10	2
W+jets	18720	3511	2943	2186	141	77	3
Di-boson	54710	20	17	9	1	0	0
SM	2245975	41538	19309	15301	717	413	51

Table 6.2: The number of events surviving the selection cuts for the inclusive tau analysis, as defined in the text. Entries are normalised to 1 fb^{-1} .

Cuts 1, 2 and 5 define the signature that is being searched for whilst the other cuts aim to reduce the SM background from events with a similar signature. Cuts 1 and 2 were applied first so that an unbiased comparison of the samples could be made, since some of the samples already had some generator level cuts applied, as described in Section 4.4.1.3. The resulting M_{eff} distribution is shown in Figure

6.5(a). From this figure it can be seen that after these cuts the main background comes from QCD multijet production. This can be reduced by applying cut 3. This cut removes events where the $E_\mathrm{T}^\mathrm{miss}$ is close to one of the three hardest jets and is thus likely to come from mismeasurement of the jets. Figure 6.5(b) shows the reduction in the QCD multijet background after applying this cut.

Cuts 4 and 5 aim to select the events with taus, eliminating the events with other isolated leptons. In order to ensure maximum efficiency for tau reconstruction, $p_\mathrm{T} > 40$ GeV is required (see Figure 5.6 in Section 5.7.5 for plots of the efficiency of the taus as a function of p_T). It can be seen from Figure 6.5(d) that this requirement dramatically reduces the QCD multijet background as well as reducing the other backgrounds. After this cut the main background comes from $t\bar{t}$.

Cut 6 requires that the $E_\mathrm{T}^\mathrm{miss}$ in the event is greater than 20% of M_{eff} so that events with hard jets but low $E_\mathrm{T}^\mathrm{miss}$ do not enter the final selection. Figure 6.5(e) shows that this cut is effective at reducing all of the SM backgrounds.

In order to further reduce events where the tau comes from the decay of a W boson, the transverse mass M_T was used. Figure 6.6 shows the M_T distribution for the different samples. From this figure it can be seen that below 100 GeV the SM background dominates, whereas above 100 GeV the SUSY signal is more dominant. This cut is particularly effective at removing W+jet events and top events but it also has an effect on the Z+jets events.

Figure 6.7 shows the percentage of real events where the tau is matched to a true tau after the last three cuts for each of the samples. It can be seen that the cut on M_T significantly reduces the number of events with real taus in the backgrounds whilst preserving the signal events.

Figure 6.8 shows the composition of the $t\bar{t}$ background; the main background to this analysis after all cuts. The number of events where the tau in the event is real and where the tau is fake coming from either a misreconstructed electron, muon or jet is shown. As well as reducing the background from $t\bar{t}$ events, it can be seen that

(a) After cuts 1-2

(b) After cut 3

(c) After cut 4

(d) After cut 5

(e) After cut 6

(f) After cut 7
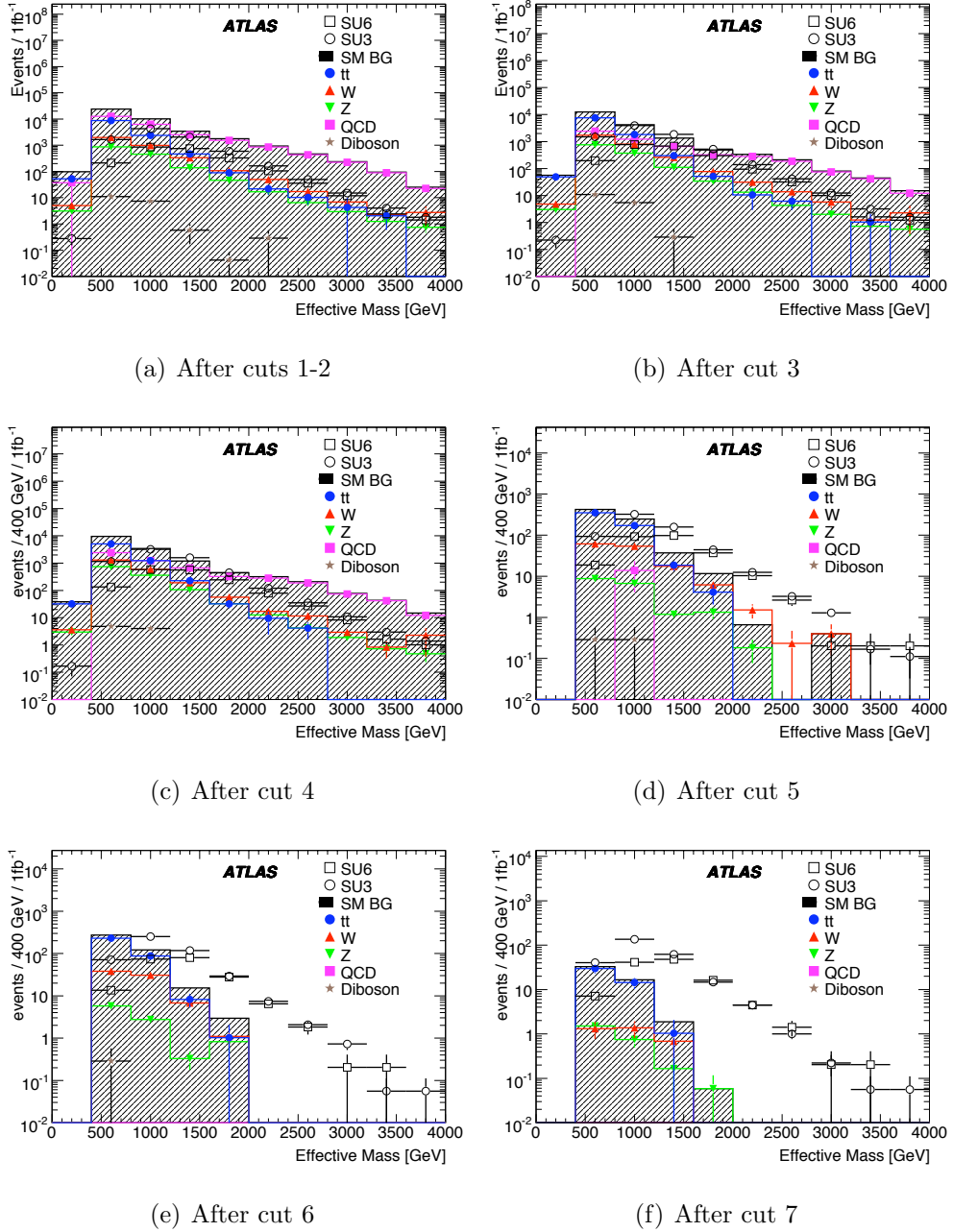
Figure 6.5: The effect of the event selection cuts of the tau analysis on the distribution of M_{eff}. All plots show the SUSY signals (open circle and square), sum of Standard Model backgrounds (histogram), and a breakdown of the background types (see legend). The cuts are described in the text. All numbers are normalized to 1fb^{-1}. The error bars reflect the statistical uncertainties of the Monte Carlo samples.

105
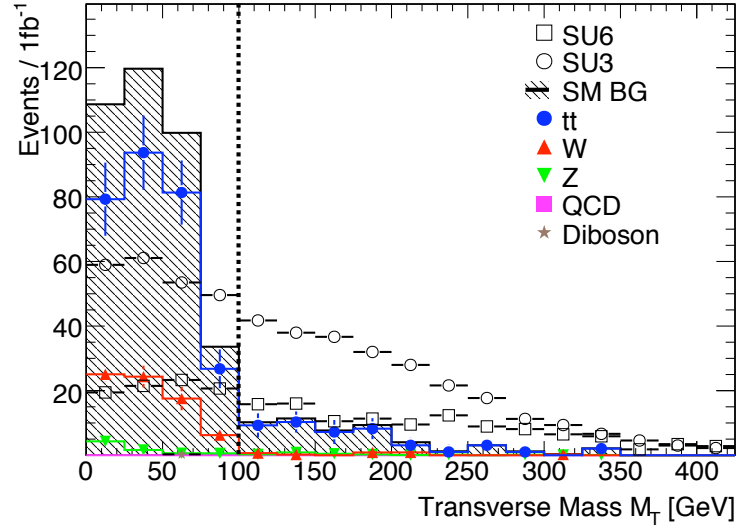
Figure 6.6: The transverse mass after cut 6 (as defined in the text). The benchmark signals are shown (open circle and square) and the SM backgrounds (see legend). All numbers are normalized to 1fb^{-1} . The error bars reflect the statistical uncertainties of the Monte Carlo samples.
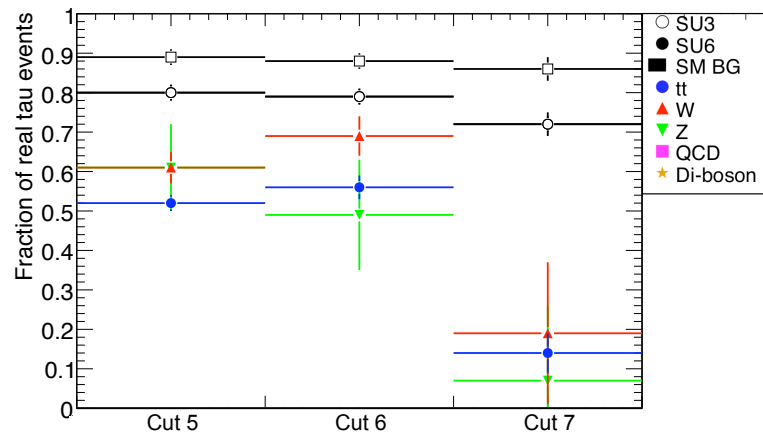
Figure 6.7: The percentage of events with a tau matched to a true tau after each of the last three cuts. The benchmark signals are shown (open circle and square) and the SM backgrounds (see legend). All numbers are normalized to 1fb^{-1} . The error bars reflect the statistical uncertainties of the Monte Carlo samples.

the last three cuts also reduced the number of events where a tau is faked by the misreconstruction of an electron, muon or jet. After all the event selection cuts, the majority of events that remain have fake taus coming approximately 21% from electrons and 18% from jets. The 21% coming from electrons could be reduced significantly by applying an electron-tau separation tool. This would significantly reduce the background from $t\bar{t}$ events. Unfortunately in Athena version 12 no such tool was available. This is something that should be investigated further in future studies using Athena version 14 and higher.
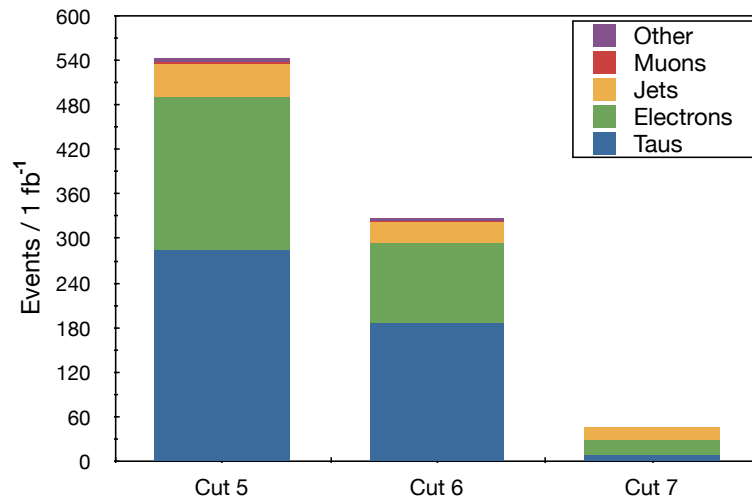
Figure 6.8: Composition of the background from $t\bar{t}$ events after the last three event selection cuts. The number of events where the tau is real and where the tau is fake coming from either a misreconstructed electron, muon or jet is shown. All numbers are for 1 fb^{-1} of integrated luminosity.

Figure 6.9 shows the final M_{eff} distribution after all event selection cuts have been applied. An excess of signal above the SM background is clearly visible for both benchmark points.

6.3.2 Inclusive three-jet and two-jet final states

At the time of beginning the work on inclusive searches using tau final states, most SUSY searches developed by the ATLAS Collaboration to look at final
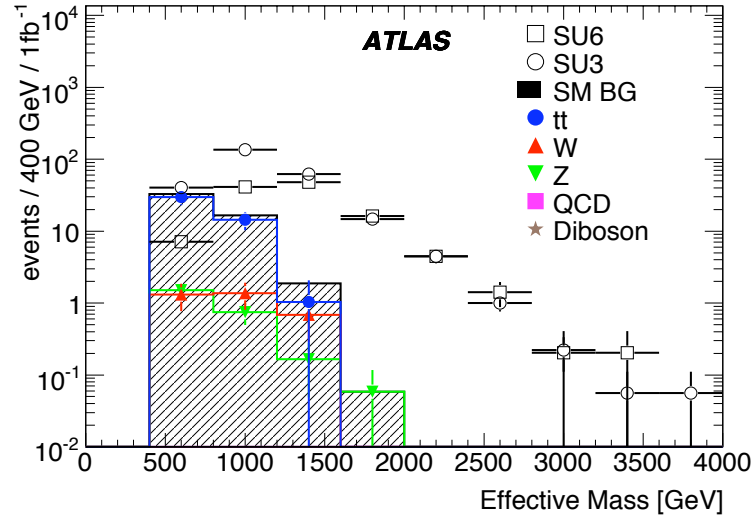
Figure 6.9: Final M_{eff} distribution after all event selection cuts have been applied. The distributions are normalised to 1 fb^{-1} of integrated luminosity.

states with jets focused on events with more than four jets in the final state. One of the reasons why these high multiplicity states are favoured is because the requirement of a high jet multiplicity strongly reduces the backgrounds from QCD multijet processes and W/Z+jets processes. However, even though the lower jet multiplicity signatures have higher backgrounds, they may be favoured in some SUSY models. Also, because their topologies are less complex these lower multiplicity signatures should be reconstructed more cleanly in the detector, which may be an advantage in the early data taking phases of the experiment. As a result, tau final states with ≥ 2 jets and ≥ 3 jets have been studied.

Note that for the three- and two-jet analyses PYTHIA samples were used for the W/Z backgrounds since as a result of the ALPGEN generator filters, samples were not available with jet multiplicities as low as 2. Table 6.3 summarises these samples.

Sample	CSC ID	$\sigma_{eff}[pb]$	N$_{events}$
$Z \rightarrow ee$	008194	46.2	$5.0 \cdot 10^3$
$Z \rightarrow \mu\mu$	008195	9.60	$5.0 \cdot 10^3$
$Z \rightarrow \tau\tau$	008191	4.50	$5.0 \cdot 10^3$
$Z \rightarrow \nu\nu$	008190	41.33	$3.5 \cdot 10^4$
$W \rightarrow e\nu$	008270	49.05	$5.0 \cdot 10^4$
$W \rightarrow \mu\nu$	008271	28.64	$3.0 \cdot 10^4$
$W \rightarrow \tau\nu$	008272	55.91	$5.5 \cdot 10^4$

Table 6.3: The CSC ID, the effective cross σ_{eff} section taking into account the event filter efficiency, and the number of events for the PYTHIA W/Z boson samples used for the 3-jet and 2-jet analyses since suitable ALPGEN samples were unavailable.

6.3.2.1 Inclusive three-jet final states

The following event selection was used for the inclusive three-jet final states analysis:

- Cut 1: At least three jets with the hardest jet having $p_T > 150$ GeV and the next two jets having $p_T > 100$ GeV.

- Cut 2: $E_T^{\mathrm{miss}} > 100$ GeV

- Cut 3: $\Delta\phi(j_i, E_T^{\mathrm{miss}}) > 0.2$ for each of the three leading jets j_i, $i = 1, 2, 3$.

- Cut 4: No isolated leptons

- Cut 5: At lease one tau $p_T > 40$ GeV

- Cut 6: $E_T^{\mathrm{miss}} > 0.25 M_{eff}$

- Cut 7: $M_T > 100$ GeV

Here M_{eff} is defined as the sum of the p_T of the three hardest jets, the hardest tau and the E_T^{miss}. Harsher cuts were used for the jets and for the E_T^{miss} to cope with increased QCD background. The resulting cutflow for 1 fb^{-1} of integrated luminosity is provided in Table 6.4. It can be seen that, as expected, the QCD

background is higher after the jets cut than in the 4-jet analysis. This is not a problem as the QCD background, although higher initially, is completely reduced by the combination of cuts 4, 5 and 6 as in the 4-jet analysis. It can also be seen that the the other backgrounds are reduced as a result of the harsher p_T and E_T^{miss} cuts. After all cuts the total SM background is 75% less than in the 4-jet analysis. Unfortunately the signals from the benchmark points are also reduced with this selection. The signal from SU3 is reduced by 36% whereas the signal from SU6 is reduced by 23%.

Sample	Events	Cut1-2	Cut3	Cut4	Cut5	Cut6	Cut7
SU3	27318	8169	6626	5460	519	309	166
SU6	5987	2249	1871	1475	232	153	92
Top	820358	5822	4105	2815	209	60	11
QCD	1337767	32562	4547	4526	7	0	0
Z+jets	14420	912	691	665	14	2	1
W+jets	18720	2288	1669	1204	119	30	1
Di-boson	54710	14	7	5	0	0	0
SM	2245975	41598	11020	9216	350	92	13

Table 6.4: The number of events surviving the selection cuts for the 3-jet inclusive tau analysis, as defined in the text. Entries are normalised to 1 fb^{-1} .

Figure 6.10 shows the final M_{eff} distribution after all event selection cuts have been applied. Although the signals from the benchmark points were reduced by the 3-jet event selection both signals can be seen above the SM background. The true potential of the analysis can be established from the scans over the SUSY parameter space since the benchmark points give just two examples of possible SUSY signals and it could be that other points in the SUSY parameter space are more visible to the 3-jet analysis than the 4-jet analysis.

6.3.2.2 Inclusive two-jet final states

The following event selection was used for the inclusive two-jet final states analysis:
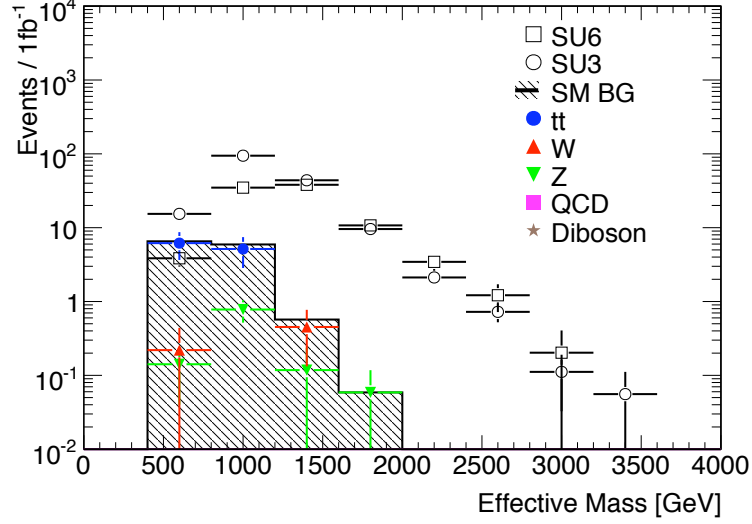
Figure 6.10: Final M_{eff} distribution after all event selection cuts have been applied for the 3-jet analysis. The distributions are normalised to 1 fb^{-1} of integrated luminosity.

- Cut 1: At least two jets with the hardest jet having $p_T > 150$ GeV and the next jet having $p_T > 100$ GeV.

- Cut 2: $E_T^{miss} > 100$ GeV

- Cut 3: $\Delta\phi(j_i, E_T^{miss}) > 0.2$ for each of the two leading jets j_i, $i = 1, 2$.

- Cut 4: No isolated leptons

- Cut 5: At lease one tau $p_T > 40$ GeV

- Cut 6: $E_T^{miss} > 0.3 M_{eff}$

- Cut 7: $M_T > 100$ GeV

Here M_{eff} is defined as the sum of the p_T of the two hardest jets, the hardest tau and the E_T^{miss}. The E_T^{miss} cut (Cut 6) was harshened again in order to cope with the extra QCD background that comes from asking for a lower jet multiplicity. The resulting cutflow for 1 fb^{-1} of integrated luminosity is provided in Table 6.5. It can be seen that the QCD background after the first cut is even higher

than for the 3-jet analysis due to the lower jet multiplicity but again this is not a problem since cuts 4, 5 and 6 completely reduce the QCD background. However, the other backgrounds are also higher. After all cuts the total SM background is almost triple that for the for the 3-jet analysis but it is still 29% lower than the SM background for the 4-jet analysis.

Sample	Events	Cut1-2	Cut3	Cut4	Cut5	Cut6	Cut7
SU3	27318	18537	12893	10532	1073	648	351
SU6	5987	4446	3225	2533	416	267	160
Top	820358	17350	11855	7679	706	183	29
QCD	1337767	101594	12914	12893	63	0	0
Z+jets	14420	2195	1664	1597	43	9	4
W+jets	18720	6005	4188	2981	309	85	3
Di-boson	54710	135	37	20	1	0	0
SM	2245975	127280	30657	25169	1123	277	36

Table 6.5: The number of events surviving the selection cuts for the 2-jet inclusive tau analysis, as defined in the text. Entries are normalised to 1 fb^{-1} .

Figure 6.11 shows the final M_{eff} distribution after all event selection cuts have been applied. Again, the signals for both benchmark points can be seen clearly above the SM background.

6.3.3 Uncertainties

SUSY searches will inevitably be subject to uncertainties due to an imperfect understanding of the behaviour of the detector e.g. uncertainties will be present in the jet energy scale, the calibration of E_T^{miss} and the lepton energy scales and identification efficiencies. In order to accurately asses the discovery potential of a search the systematic uncertainties of the SM background must be considered. Measurement of the SM background and its uncertainties using a combination of MC and data-driven methods has been extensively studied in Ref. [80, 81].
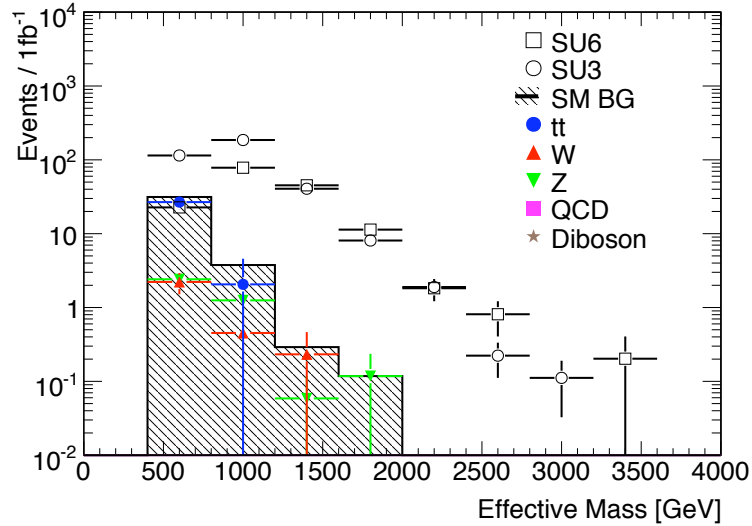
Figure 6.11: Final M_{eff} distribution after all event selection cuts have been applied for the 2-jet analysis. The distributions are normalised to 1 fb^{-1} of integrated luminosity.

Taking recommendations from these studies the systematic uncertainties in this analysis were assumed to be:

- 20% for the $t\bar{t}$, W+jets, Z+jets and diboson samples

- 50% for the QCD multijets samples.

An additional uncertainty of 10% and 30% was associated to the tau reconstruction efficiency and rejection respectively, since uncertainties in the tau reconstruction algorithms may be important. As an approximation the systematic uncertainties were assumed to be uncorrelated and independent of any variable, as such they were combined in quadrature. The limited MC statistics were also taken into account.

Table 6.6 shows the number of expected events for the dominant background contributions to the 4-jet, 3-jet and 2-jet analyses after all cuts, the statistical uncertainty, the systematic uncertainty and in parenthesis the systematic uncertainty taking into account the systematic uncertainty from the tau reconstrucion.

The same numbers for the total SM background are also shown. The numbers correspond to 1 fb^{-1} of integrated luminosity.

Sample	Expected events 1 fb^{-1}		
	4-jets	3-jets	2-jets
$t\bar{t}$	$45.1 \pm 8.1 \pm 9.1(10.0)$	$11.3 \pm 3.4 \pm 2.3(2.5)$	$28.8\pm6.0 \pm 5.8(6.3)$
Z+jets	$2.5 \pm 0.5 \pm 0.5$ (1.2)	$1.1 \pm 0.3 \pm 0.2(0.5)$	$3.8\pm0.6 \pm 0.8(1.8)$
W+jets	$3.4 \pm 0.9 \pm 0.7$ (1.1)	$0.7 \pm 0.4 \pm 0.1(0.2)$	$2.9\pm0.8 \pm 0.6(0.9)$
SM	$51.1 \pm 8.2\pm9.1$ (10.0)	$13.1\pm3.5 \pm 2.3(2.5)$	$35.6\pm6.1 \pm 5.8(6.3)$

Table 6.6: Main background contributions for the 4-jets, 3-jets and 2-jets tau analysis after all cuts including statistical (second number given) and systematic uncertainties (third number given). The number in parenthesis indicates the total systematic uncertainty when the uncertainty from the tau recontruction is included. All numbers are for 1 fb^{-1} of integrated luminosity.

6.3.4 Performance

A measure of how well the analysis performs is given by the statistical significance. For this analysis the significance is a measure of the probability that the excess of events with respect to the SM, produced by the SUSY signal, could have occurred by a statistical fluctuation.

A simplified definition of the significance is given by:

$$\mathcal{S} = \frac{S}{\sqrt{B}}. \tag{6.4}$$

where S is the number of signal events and B is the number of background events. This definition does not take into account the uncertainties on the background estimation. In order to include them, the probability that the number of background events N_b randomly fluctuates to produce the measured value N_{data} is taken to be a convolution of a Poisson probability density function (PDF) (which accounts for the statistical uncertainties) and a Gaussian PDF $G(b; N_b, \delta N_b)$ with

a mean N_b and width δN_b (which accounts for the non-negligible systematic uncertainties):

$$p = A \int_0^\infty db\, G(b; N_b, \delta N_b) \sum_{i=N_{data}}^\infty \frac{e^{-b}b^i}{i!} \tag{6.5}$$

where A is a normalization factor:

$$A = \frac{1}{\int_0^\infty db\, G(b; N_b, \delta N_b) \sum_{i=0}^\infty \frac{e^{-b}b^i}{i!}}$$

The probability p can be represented in terms of the number of "standard-deviations" Z_n using:

$$Z_n(p) = \text{erf}^{-1}(1 - 2p) \cdot \sqrt{2} \tag{6.7}$$

Table 6.7 shows the number of signal events S, the number of SM background events B after all event selection cuts, together with $S/\sqrt{B}$ (the estimation of the statistical significance) and Z_n (the significance taking into account the statistical and systematic uncertainties), for both benchmark points.

Sample	4-jets		3-jets		2-jets	
	SU3	SU6	SU3	SU6	SU3	SU6
S	259	119	166	92	351	160
B	51	51	13	13	36	36
S/B	5.1	2.3	12.8	7.1	9.8	4.4
$S/\sqrt{B}$	36.3	16.7	46.0	25.5	58.5	26.7
Z_n	> 6	> 6	> 6	> 6	> 6	> 6

Table 6.7: Number of signal events S, background events B, the significance $S/\sqrt{B}$ and the significance considering the uncertainties Z_n. All numbers are for 1fb^{-1} of integrated luminosity.

It can be seen that inclusive searches with tau final states are promising for both high and low $\tan\beta$ scenarios for all three jet multiplicities with each one

reaching a significance above 6 [1]. Remembering that the cross-section for the SU6 benchmark point is approximately four times lower than for SU3, it is clear that the tau channels are especially important for high $\tan\beta$ scenarios.

6.4 Scans in Regions of High $\tan\beta$

As described in Section 6.1.3, the ATLAS search strategy uses the benchmark points to define an analysis as above. The analysis is then run on a scan of hundreds of points in the SUSY parameter space of different models in order to verify that the analysis defined provides sensitivity to a wide range of SUSY signals. A grid of SUSY points was selected for this analysis with $\tan\beta = 50$ used to represent a high $\tan\beta$ scenario since decays to taus are enhanced for $\tan\beta >> 1$ [77]. The grid is described in detail in Section 4.4.1.2. The exact details of the grid are not important here as the aim is not to determine the exact limit or exclusion value, instead the aim is to test whether the analysis proposed provides sensitivity to a wide range of points in the high $\tan\beta$ scenario.

Due to the complexity of computing the NLO cross-sections and time pressures, the collaboration decided to normalise the signal cross-sections to LO values. Since NLO corrections generally increase cross-sections the resulting reach estimates are conservative. The NLO cross-sections were used for the background processes.

6.4.1 Optimisation

Further optimisation was performed for the points in the SUSY signal grid so that the best significance could be achieved for each point. Figure 6.12 demonstrates this procedure. The individual points in the SUSY grid present different possible SUSY signals and therefore each one has a different M_{eff} distribution. The M_{eff} distribution of each point was scanned with an algorithm to find the

---

[1]Due to numerical problems with the error function (erf), the calculation of Z_n doesn't work for significances higher than 6 and so significances higher than 6 are indicated as such in the table without giving a specific value for the significance.

largest achievable significance Z_n for each point. The algorithm uses a set of n cuts with $M_{eff} > X_n$ GeV. Each value of X_n corresponds to the value of M_{eff} at the edge of the bin n where the width of each bin is 400 GeV.

Looking at many different cut trials it becomes more likely that statistical fluctuations can be misinterpreted as new physics if the number of trials is not taken into consideration. This is known in statistics as 'the problem of multiple comparisons'. To account for this the probability values from the scans were corrected for multiple comparisons following the Monte Carlo method procedure used in the CSC studies [75]. This involves generating millions of hypothetical M_{eff} distributions, generating a random number of events in each bin according to a Poisson distribution of the expected number of events in that bin of the histogram. The result is a large set of M_{eff} distributions, each one representing a possible outcome. The scan algorithm used to determine the cut in M_{eff} that gives the highest significance was then run on each of the hypothetical histograms. The fraction F of histograms giving a significance larger than Z_n is calculated for each value of Z_n. F is the corrected probability for finding a deviation with a significance $\max(Z_n)$ in data. F is converted into the "corrected Z_n" using:

$$\text{corrected } Z_n(p) = erf^{-1}(1 - 2F) \cdot \sqrt{2} \qquad (6.8)$$

6.4.1.1 Discovery Reach and Comparison With Other Channels

The most promising ATLAS inclusive channels have been the 0-lepton and 1-lepton modes [75]. These channels search for the following signatures:

0-lepton mode   The standard 0-lepton mode looks for events with at least four jets, E_T^{miss} and no isolated leptons.

1-lepton mode   The standard 1-lepton mode looks for events with at least four jets, E_T^{miss} and exactly one isolated electron or muon.
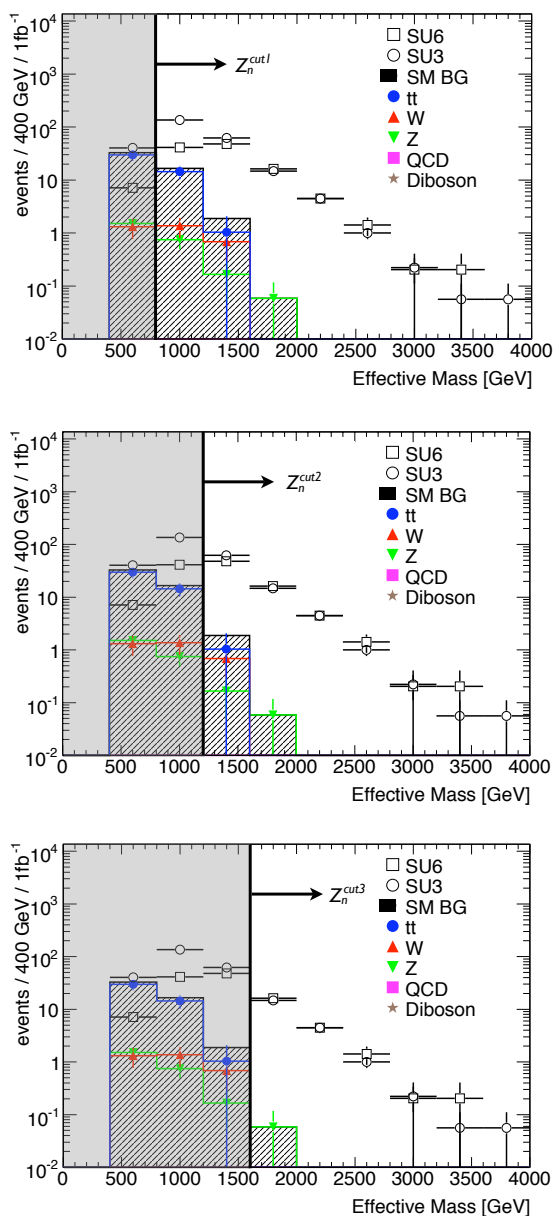
Figure 6.12: Demonstration of the procedure used to optimize the significance for each SUSY point in the SUSY grids. The lower bound on M_{eff} is varied for each point until the best significance is achieved.

Figure 6.13 shows the M_{eff} distributions after all event selection cuts for the 0-lepton mode (top) and the 1-lepton mode (bottom). The individual SM background contributions are shown relative the SU3 benchmark point (left) and the total SM background is shown relative to a number of benchmark points (as defined in [75]) including SU6 (right).
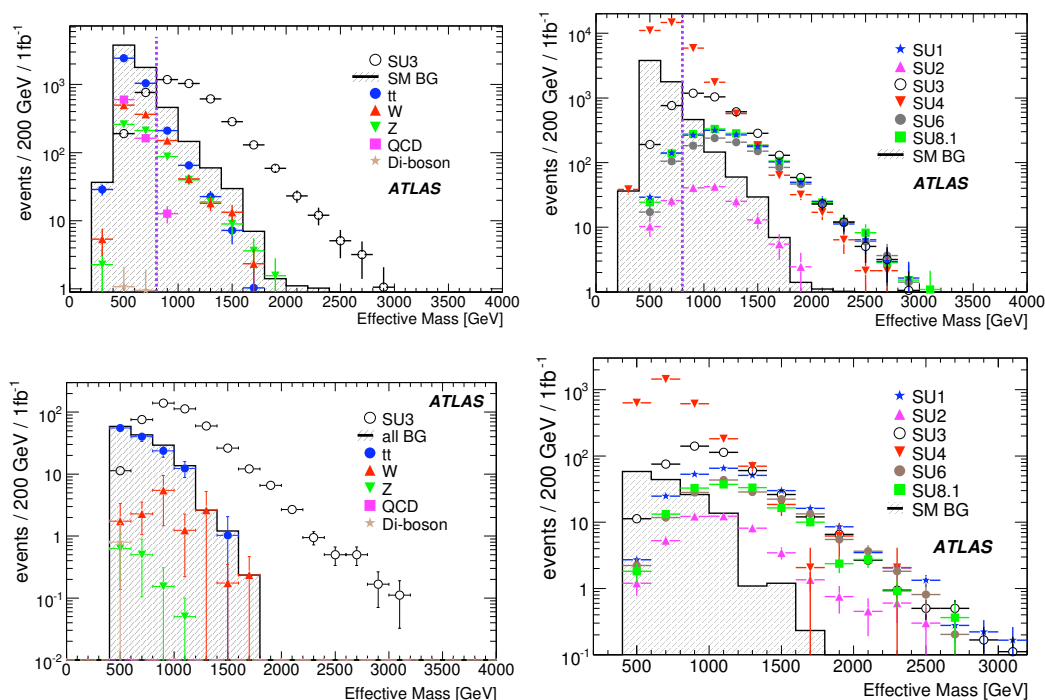
Figure 6.13: The M_{eff} distributions for the 0-lepton mode (top) and 1-lepton mode (bottom) for 1fb^{-1} of integrated luminosity. The individual contributions of the SM backgrounds are shown in comparison to the signal from the SU3 benchmark point (left), and the total SM background is shown relative to the signals from various benchmark points (as defined in [75]), shown here to demonstrate the SU6 benchmark point (right). Taken from Ref. [75].

The curves for all three channels are very similar. Looking at the small differences, the 0-lepton mode offers the greaterst yield of signal events compared to the 1-lepton and tau channels but the SM backgrounds are higher particularly at low M_{eff}. The requirement of a lepton in the 1-lepton channel and the require-

ment of a tau in the tau-channel completely reduces the SM background from QCD multijet processes but this background is still present in the 0-lepton mode. This background will need to be understood for this channel. In this respect the 1-lepton and tau channels are more robust. It can be seen that the tau-channel looks very competitive with the 1-lepton channel for the benchmark points SU3 and SU6.

A better idea of how the performance of these channels compare can be obtained by considering many possible SUSY signals i.e. using the scan over grids of points in the SUSY parameter space. This will show if the analyses only perform well for a select number of points or perform well for most points and where in the SUSY parameter space each analysis performs best. It will also give an idea of the reach of these analyses.

Figure 6.14 (top) shows the 5σ discovery reach obtained for the 0-lepton, 1-lepton and tau (4-jets) analyses when these analyses are run on the points in the high $\tan\beta$ grid. The mass contours for gluinos and squarks are also shown. It can be seen that the 0-lepton mode has the best estimated reach even at high $\tan\beta$. For the smaller squark and gluino masses the reach is close to 1.5 TeV. The reach for the 1-lepton mode is less but as previously discussed, this analysis is more robust against QCD backgrounds. Despite the enhancement of tau decays for $\tan\beta \gg 1$, the reach for the tau channel is slightly worse than for the 1-lepton channel. This reflects the lower efficiency and purity for tau reconstruction. The reason for the better performance in the 1-lepton channel compared to the tau channel could also come from the enhancement of decays to taus since 35% of taus decay leptonically to electrons and muons. Since these electrons and muons are indistinguishable from electrons and muons from other processes they will provide a signal for the 1-lepton channel. This may also be true for the 0-lepton channel since it does not exclude taus and thus an enhancement of taus may increase the signal for this channel.

Figure 6.14 (bottom) shows a comparison of the 5σ discovery reach for the 4-jets, 3-jets and 2-jets inclusive tau analyses. It can be seen that the reach of the 3-jets
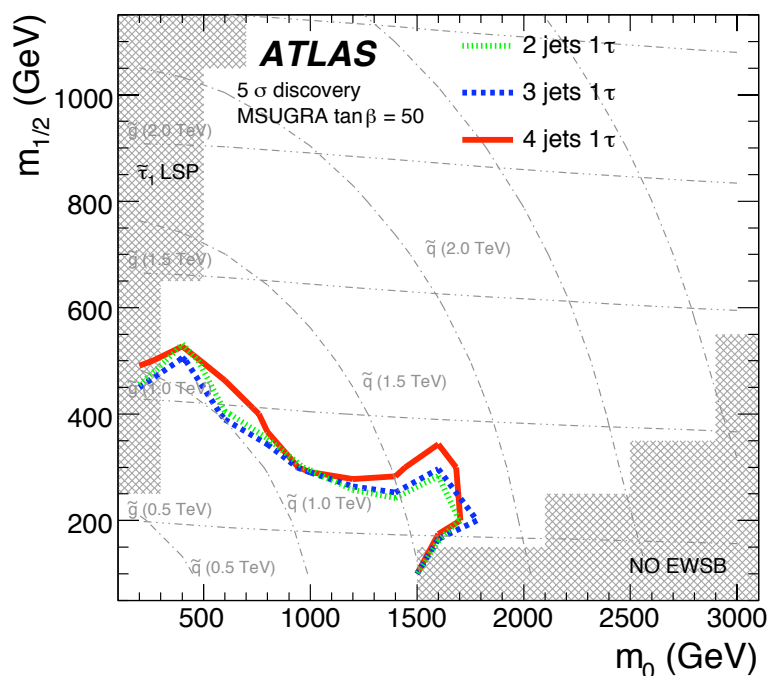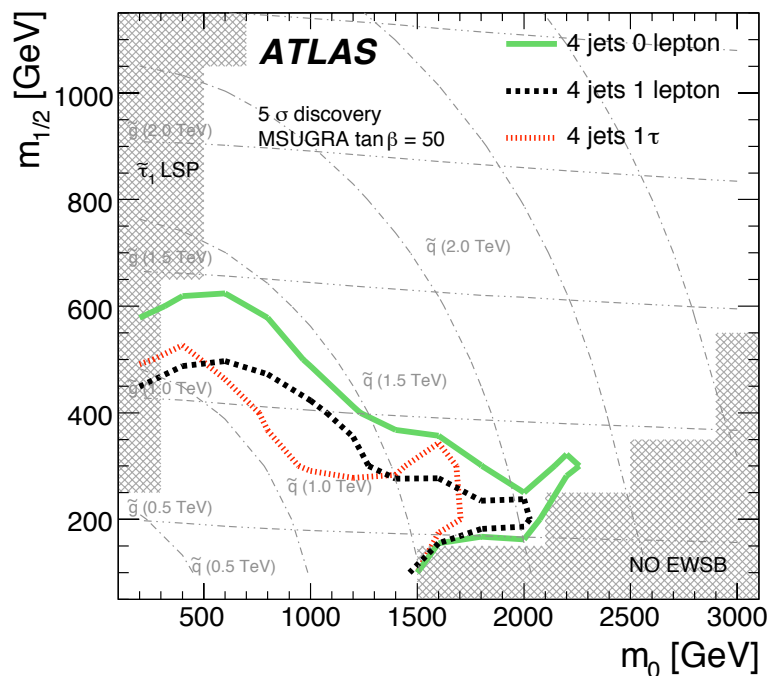
Figure 6.14: The 5σ reach contours for the 0-lepton, 1-lepton and tau analyses with at least 4-jets in the final state (top), and the different jet multiplicity tau analyses (bottom), for mSUGRA as a function of m_0 and $m_{1/2}$. $\tan\beta = 50$. The horizontal and curved grey lines indicate the gluino and squark masses respectively in steps of 500 GeV.

analysis is slightly better than the 4-jets analysis, whilst the reach of the 2-jets analysis is roughly the same as the 4-jets analysis.

6.5 Conclusions

A new inclusive search mode has been developed to search for SUSY with the ATLAS detector. The mode focuses on the signature of taus, jets and $E_{\mathrm{T}}^{\mathrm{miss}}$. Analyses with different jet multiplicities (4, 3 and 2-jets) have been studied. The requirement of the tau significantly reduces the abundant QCD multijet background making the mode potentially more robust than other modes already in use that focus only on jets and $E_{\mathrm{T}}^{\mathrm{miss}}$ as the signature.

The discovery reach for this new search mode, for R-parity conserving mSUGRA models, has been studied for a centre-of-mass energy of 14 TeV and an integrated luminosity of $1\mathrm{fb}^{-1}$. It has been shown that the tau mode is competitive with other inclusive search modes used by the ATLAS Collaboration, particularly for regions of the SUSY parameter space with high $\tan\beta$ where tau decays are enhanced. It has been shown that models with high $\tan\beta$ and squark and gluino masses less than $\mathcal{O}(1\ \mathrm{TeV})$ are within the 5σ discovery reach.

Chapter 7

Measuring the tau identification efficiency using $t\bar{t}$ events in early data

The studies detailed in this chapter were published in an ATLAS internal note, Ref: [82].

7.1 Introduction

Tau leptons play an important role in the physics expected at the LHC both in Standard Model and beyond the Standard Model processes. They will provide an excellent probe in searches for new phenomena, as was shown in the previous chapter. For any analysis involving taus it will be important to understand how well the tau identification algorithms are performing so that the number of taus observed by the ATLAS detector can be fully understood. As described in Section 5.7.3, a measure of the performance of an algorithm used to identify a physics object is the identification efficiency. For a physics object of type X, the identification efficiency is defined as the fraction of real objects of type X that are reconstructed as objects of type X.

Two main methods have been developed within the ATLAS Collaboration so far to measure the identification efficiencies of taus. These involve the reconstruction

of the electroweak boson decays: $Z \to \tau\tau$ and $W \to \tau\nu$. The results of these methods are collected in Ref. [69]. However, these methods suffer from high QCD backgrounds and poor trigger efficiencies and so a method that improves both of these aspects is desired. In addition, the tau identification efficiency depends on the environment in which the tau is identified, as was demonstrated in Figure 5.6. Tau decays in events with a clean environment e.g. $Z \to \tau\tau$ will present higher identification efficiencies than those in busier events with high jet multiplicities e.g. $t\bar{t}$ decay or supersymmetric decays. The current methods used to measure the tau identification efficiency use relatively clean environments but many of the analyses that will be performed by the ATLAS Collaboration involve busy environments, e.g. cascade decays of squarks and gluinos produce busy environments with a number of jets and a number of leptons and these signatures form the basis of the ATLAS inclusive searches for SUSY (see Chapter 6). The current methods to measure the tau identification efficiency are not ideal for these analyses since the identification efficiency will be measured higher than it actually is. It is therefore desirable to have a method that addresses the identification in these challenging environments. For these reasons one of the main goals of this thesis was to develop a new method to measure the tau identification efficiency in early data.

$t\bar{t}$ decays offer a busy environment in which to measure the tau identification efficiency. As described in Section 1.1.3, by classifying the $t\bar{t}$ decays according to the decays of the W-bosons three channels are defined:

- **Fully hadronic channel**: both W-bosons decay to quark pairs – resulting in a signature with a number of high p_T jets.

- **Semileptonic channel**: one W-boson decays to a quark pair and the other to a lepton-neutrino pair – resulting in a signature of high p_T jets, E_T^{miss} from the neutrinos and a lepton.

- **Dilepton channel**: both W-bosons decay to lepton-neutrino pairs – resulting in a signature of at least 2 high p_T b-jets, E_T^{miss} from the neutrinos and leptons.

As discussed in Section 1.1.3 and demonstrated in Figure 1.2, the cross-section for production of $t\bar{t}$ pairs at the LHC will be of the order of 100 times larger than that at the Tevatron. With a cross-section of 833 pb for a centre-of-mass energy of 14 TeV and a cross-section of 401 pb for a centre-of-mass energy of 10 TeV, millions of $t\bar{t}$-pairs will be produced every year [12]. This abundance of events makes $t\bar{t}$ decays ideal for measuring the tau identification efficiency in early data.

The fact that the top quark is a complex object with high jet multiplicities and intrinsic missing transverse energy provides handles for triggering and for reducing backgrounds. The method presented here to measure the tau identification efficiency using $t\bar{t}$ events offers good control of multijet QCD background and does not rely on the tau trigger. It also does not rely on b-tagging to reconstruct the top quark, making it an ideal method for early data.

The analysis presented in this chapter was first developed when it was believed that the start-up centre-of-mass energy of the LHC would be 14 TeV. As described in Section 4.4, since then a start-up centre-of-mass energy of 10 TeV followed by 7 TeV has been proposed. This chapter will present the general method for this analysis and the performance of the method for 14 TeV. Chapter 8 will provide an update of the performance of the method for a centre-of-mass energy of 10 TeV.

7.2 The Method

The tau identification efficiency can be measured by comparing the number of events in two semileptonic $t\bar{t}$ decay channels; a channel where one tau identification is required i.e. the leptonically decaying W-boson decays to a tau-neutrino pair (the τ-channel), and one where no tau identification is required i.e. the leptonically decaying W-boson decays to an elecron- or muon-neutrino pair (the l-channel). The difference in the number of events measured in each of these two channels will be dominated by the differences in the lepton identification algorithm efficiencies. Therefore, if the identification efficiency of the lepton l (where $l = e, \mu$) is known, by comparing the number of events in each channel the tau identification efficiency can be deduced. In this thesis the μ-channel will be used

as the comparison channel, but the e-channel could also have been used.

The number of events expected in the τ-channel N^τ_{exp} can be expressed as follows:

$$N^\tau_{exp.} = \sigma(t\bar{t}) \times L \times B^\tau \times \varepsilon^\tau_{cuts} \times \varepsilon^\tau_{ID} = N^\tau_{meas.} - N^\tau_{bkg} \tag{7.1}$$

where $\sigma(t\bar{t})$ is the $t\bar{t}$ production cross-section, L is the integrated luminosity, B^τ is the branching ratio for a $t\bar{t}$-pair to decay semileptonically to a tau that then decays hadronically, ε^τ_{cuts} is the efficiency of the event selection cuts used to isolate the τ-channel events from data and ε^τ_{ID} is the tau identification efficiency. The number of expected events can also be expressed as the number of events measured when applying the event selection cuts used to select τ-channel events from the data N^τ_{meas}, minus the number of background events N^τ_{bkg} i.e. non-signal events that pass the event selection cuts.

Similarly for the comparison lepton channel:

$$N^l_{exp.} = N^l_{meas.} - N^l_{bkg} = \sigma(t\bar{t}) \times L \times B^l \times \varepsilon^l_{cuts} \times \varepsilon^l_{ID} \tag{7.2}$$

where B^l is the branching ratio for a $t\bar{t}$-pair to decay semilpetonically to the lepton l (this includes semileptonic decays to a tau which then decays leptonically to l since leptonically decaying taus are indistinguishable from electrons and muons in the detector), ε_{cuts} is the efficiency of the event selection cuts used to isolate the l-channel events from data and ε^l_{ID} is the identification efficiency of the lepton l.

From the ratio of these two equations an expression for the τ-identification efficiency can be obtained that depends only on the number of expected events in each channel, the respective branching ratios, the efficiency of the event selection cuts and the identification efficiency of the lepton l:

$$\varepsilon^\tau_{ID} = \frac{N^\tau_{exp.}}{N^l_{exp.}} \times \frac{B^l}{B^\tau} \times \frac{\varepsilon^l_{cuts}}{\varepsilon^\tau_{cuts}} \times \varepsilon^l_{ID} \tag{7.3}$$

Figure 7.1 shows a schematic of the semilpetonic $t\bar{t}$ decay. The decay to a tau is shown on the left and the decay to other leptons is shown on the right. Comparing

the decays it can be seen that they are identical apart from the lepton flavour and the decay of the tau. If the kinematics are the same i.e. the $t\bar{t}$ pairs have the same initial boost and so the leptons have the same momentum, it can be expected that the hadronic top quark decay to jets will be identical in the τ-channel and the l-channel, despite the different leptons in the decay of the other top quark. There is no reason to believe that the top quark decay to jets is affected by what lepton the other top quark decays to. This is a great advantage of this method, which can be seen when considering the uncertainties. In early data there will be uncertainties for channels with jets due to, for example, the unknown jet energy scale. Because this analysis compares two channels where the jets are expected to be identical (if the kinematics are approximately the same in each channel) the uncertainties involving the jets will be the same in each channel and will thus cancel when the ratio of the channels is taken. This allows the use of channels with jets, which are easier to trigger than channels with only tau leptons, but without the uncertainties brought by the jets.
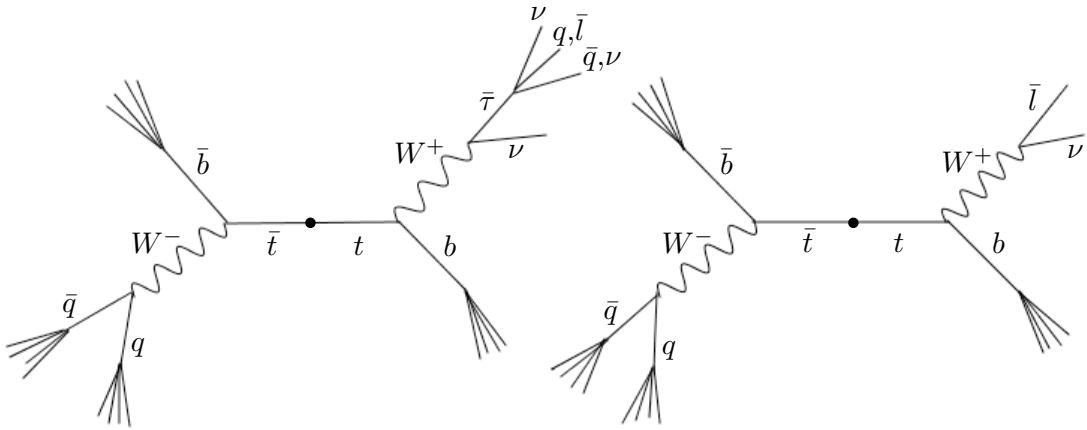
Figure 7.1: Schematic of the semileptonic $t\bar{t}$ decay to a tau final state (left) and to an electron/muon final state (right). $l = e, \mu$

The full uncertainty on the method can be expressed using propagation of errors

as:

$$\left(\frac{\delta\varepsilon_{ID}^{\tau}}{\varepsilon_{ID}^{\tau}}\right)^2 = \left(\frac{\delta N_{exp.}^{\tau}}{N_{exp.}^{\tau}}\right)^2 + \left(\frac{\delta N_{exp.}^{l}}{N_{exp.}^{l}}\right)^2 + \left(\frac{\delta B^l}{B^l}\right)^2 + \left(\frac{\delta B^\tau}{B^\tau}\right)^2 + \left(\frac{\delta(\varepsilon_{cuts}^l/\varepsilon_{cuts}^\tau)}{(\varepsilon_{cuts}^l/\varepsilon_{cuts}^\tau)}\right)^2 + \left(\frac{\delta\varepsilon_{ID}^l}{\varepsilon_{ID}^l}\right)^2$$

(7.4)

The branching ratios for top quark decays are known very precisely and thus the uncertainties on these will be negligible compared to the other terms. The identification efficiency of the electron/muon is also expected to be known precisely (on the order of 1% with 100 pb^{-1} of integrated luminosity [53]) and so can also be safely neglected. Since $N_{exp.} = N_{meas.} - N_{bkg}$, Equation 7.4 can be re-written as:

$$\left(\frac{\delta\varepsilon_{ID}^{\tau}}{\varepsilon_{ID}^{\tau}}\right)^2 = \frac{((\delta N_{meas.}^{\tau})^2 + (\delta N_{bkg}^{\tau})^2)}{(N_{meas.}^{\tau} - N_{bkg}^{\tau})^2} + \frac{((\delta N_{meas.}^{l})^2 + (\delta N_{bkg}^{l})^2)}{(N_{meas.}^{l} - N_{bkg}^{l})^2} + \left(\frac{\delta(\varepsilon_{cuts}^l/\varepsilon_{cuts}^\tau)}{(\varepsilon_{cuts}^l/\varepsilon_{cuts}^\tau)}\right)^2$$

(7.5)

7.3 Experimental Setup

7.3.1 Monte Carlo Samples

The Monte Carlo samples used in this study were produced with Athena version 12.0.6 in the context of the Computing System Commissioning (CSC) studies [53], produced to model a centre of mass energy of 14 TeV. All samples are based on a full simulation of the ATLAS detector using the GEANT4 program. The mass of the top quark was taken to be 175 GeV. The samples are described in Section 4.4.1.

7.3.2 Trigger

Due to the rich final state topology expected in $t\bar{t}$ events and the strong cuts used in this analysis (see Section 7.4) the trigger efficiency is expected to be high. The same multijet and E_T^{miss} triggers could be used as in the inclusive SUSY searches performed by the ATLAS Collaboration. Studies have been performed

that calculated the trigger efficiency for events with a number of high p_{T} jets and $E_{\mathrm{T}}^{\mathrm{miss}}$ and these studies have concluded that a trigger efficiency greater than 95% is expected (see Section 6.2.2). The trigger menus will be reviewed before starting collisions at 14 TeV and the trigger efficiencies will need to be reassessed once the new menus are available, but triggering is not expected to be a problem for this analysis. As a result a trigger efficiency of 100% was assumed in this study.

7.3.3 Object Selection and Overlap Removal

The object selection and overlap removal used in this analysis are detailed in Section 5.7.

7.4 Isolating the $t\bar{t}$ events from data

For the measurement of the tau identification efficiency two samples of events are required: a sample of τ-channel events and a sample of the comparison l-channel events (where $l = e$ or μ). In this thesis the μ-channel is used. These $t\bar{t}$ events must be extracted from the mixture of events in data. To do this, event selection cuts are applied to the data, with the aim to extract the signal events based on their signature.

7.4.1 Isolating the τ-channel events

The semileptonic $t\bar{t}$ decay is characterised by a number of high p_{T} jets, from the hadronically decaying W boson and from the b-jets, as well as $E_{\mathrm{T}}^{\mathrm{miss}}$ and a lepton from the leptonically decaying W boson. So for the τ-channel a signature of at least four jets, $E_{\mathrm{T}}^{\mathrm{miss}}$ and a τ is expected. The main backgrounds to this signature are:

- $t\bar{t}$ **pairs**: Semileptonic $t\bar{t}$ decays to electrons and muons can produce a similar final state signature at reconstruction level. For example, an electron or muon can be misreconstructed as a tau or they can be lost and one of the jets misreconstructed as a tau. Dileptonic $t\bar{t}$ pairs can also produce a

similar final state, especially dileptonic final states involving taus where the second lepton is lost.

- **QCD multijets**: QCD jet reconstruction may introduce fake $E_\mathrm{T}^\mathrm{miss}$ to the event due to the limitations of the calorimeter and the algorithm used for reconstruction, which cannot be fully corrected for. In addition, heavy flavour jets may decay semileptonically, and light flavour jets may be misidentified as taus.

- W**+jets**: Since the taus from the $t\bar{t}$ decay actually come from the decay of an intermediate W boson, W boson decay is going to look very similar to the signal events, when the W boson is produced in association with jets.

The following event selection cuts were used to isolate the τ-channel events from SM backgrounds:

- Cut 1 (Jets Cut): At least four jets with the hardest jet having $p_\mathrm{T} > 80$ GeV and the next three jets having $p_\mathrm{T} > 50$ GeV.

- Cut 2 ($E_\mathrm{T}^\mathrm{miss}$ Cut): $E_\mathrm{T}^\mathrm{miss} > 100$ GeV.

- Cut 3 ($\Delta\phi$ Cut): $\Delta\phi(\mathrm{j}_i, E_\mathrm{T}^\mathrm{miss}) > 0.2$ for each of the three leading jets j_i, $i = 1, 2, 3$.

- Cut 4 (ID Cut): At lease one τ with $p_\mathrm{T} > X$ GeV and $|\eta| < 2.5$ (where $X = 20, 40$ GeV).

- Cut 5 (M_T Cut): $M_\mathrm{T} < 100$ GeV.

where the transverse mass M_T is defined as the invariant mass of the hardest tau and the $E_\mathrm{T}^\mathrm{miss}$ in the transverse plane.

The jets cut, the $E_\mathrm{T}^\mathrm{miss}$ cut and the ID cut select the 'jets plus $E_\mathrm{T}^\mathrm{miss}$ plus tau' signature. The other cuts aim to reduce the background from other SM processes. The jets and $E_\mathrm{T}^\mathrm{miss}$ cuts were applied first since a number of the Monte Carlo samples used for this study already had generator level cuts applied to the number and p_T of the jets and the $E_\mathrm{T}^\mathrm{miss}$ (as detailed in Section 4.4.1.3), so having

these cuts applied first allows an unbiased comparison of the samples. The $\Delta\phi$ cut imposes an angular distance between the MET and each of the three leading jets to reduce the background from mismeasured jets. The M_T cut ensures that the E_T^{miss} comes from $W \to \tau\nu$ decays, such decays should satisfy $M_T < m_W$.

The method proposed in Section 7.2 can be used to measure the τ identification efficiency for taus with different phase space (different p_T and η). To demonstrate this, two p_T scenarios are considered:

- Low p_T scenario: Tau is required to have $p_T > 20$ GeV and $|\eta| < 2.5$.

- High p_T scenario: Tau is required to have $p_T > 40$ GeV and $|\eta| < 2.5$.

Table 7.1 (Table 7.2) shows the resulting cutflow for the low (high) p_T scenario. It can be seen that the $\Delta\phi$ cut and the ID cut allow good control of the background from QCD multijets. This is further illustrated in Figure 7.2, which shows the shape of the QCD background before the ID cut when the mass of the hadronically decaying t-quark (M_{jjj}) is reconstructed (see Section 7.4.3 for details on the reconstruction). This shows that the QCD multijet background peaks away from the top mass peak. The remaining background comes mostly from W+jet events, with a small contribution from Z+jet and QCD multijet events.

Sample	Events	Jets + E_T^{miss}	$\Delta\phi$	ID	M_T
Top leptonic	440841	12159.4	10379.3	1109.9	922.5
Top hadronic	379517	452.7	202.4	0	0
QCD	1635207.6	29615.6	6883.3	34.9	32.8
Z+jets	14420.5	1588.2	1346.9	36.6	29.0
W+jets	18720.2	3603.2	3029.7	254.6	235.6
Di-boson	54709.6	21 .2	18.2	0.9	0.9
SM Background	2102574.8	35280.9	11480.5	327.0	298.3

Table 7.1: Number of events surviving the selection cuts defined in the text for the low p_T scenario τ-channel. "Top Leptonic" includes all $t\bar{t}$ events with a leptonic decay e.g. dileptonic $t\bar{t}$ events, not just the τ-channel signal events.
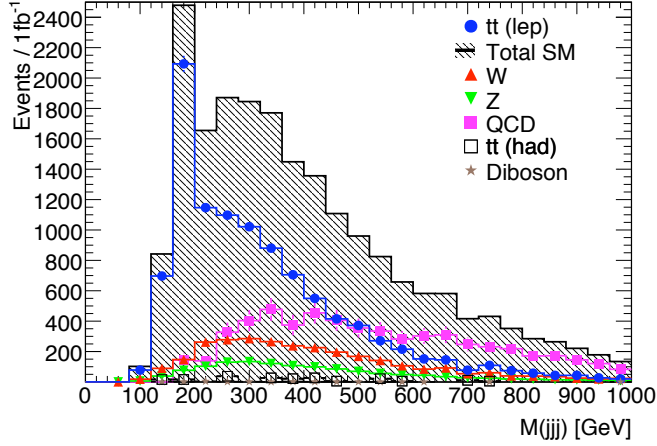
Figure 7.2: Reconstructed top quark mass (M_{jjj}) where the top quark is reconstructed using the minimum ΔR method described in Section 7.4.3 for the τ-channel for 1 fb^{-1} of integrated luminosity. Only the jets cut, $E_{\mathrm{T}}^{\mathrm{miss}}$ cut and $\Delta\phi$ cut are applied.

Sample	Events	Jets + $E_{\mathrm{T}}^{\mathrm{miss}}$	$\Delta\phi$	ID	M_T
Top leptonic	440841	12159.4	10379.3	626.0	521.0
Top hadronic	379517	452.7	202.4	0	0
QCD	1635207.6	29615.6	6883.3	25.7	23.6
Z+jets	14420.5	1588.2	1346.9	21.3	17.7
W+jets	18720.2	3603.2	3029.7	149.7	139.6
Di-boson	54709.6	21 .2	18.2	0.6	0.6
SM Background	2102574.8	35280.9	11480.5	197.3	181.6

Table 7.2: Number of expected events for 1 fb^{-1} after all the selection cuts defined in the text for the high p_{T} scenario τ-channel. "Top Leptonic" includes all $t\bar{t}$ events with a leptonic decay e.g. dileptonic $t\bar{t}$ events, not just the τ-channel signal events.

7.4.2 Isolating the μ-channel events

The μ-channel is characterised by at least four high p_{T} jets, $E_{\mathrm{T}}^{\mathrm{miss}}$ and a muon. The channel suffers from the same backgrounds as the τ-channel. The following event selection cuts were used to isolate the μ-channel events from SM backgrounds:

- Cut 1 (Jets Cut): At least four jets with the hardest jet having $p_T > 80$ GeV and the next three jets having $p_T > 50$ GeV.

- Cut 2 (E_T^{miss} Cut): $E_T^{\text{miss}} > 100$ GeV.

- Cut 3 ($\Delta\phi$ Cut): $\Delta\phi(j_i, E_T^{\text{miss}}) > 0.2$ for each of the three leading jets j_i, $i = 1, 2, 3$.

- Cut 4 (ID Cut): At lease one μ with $p_T > X$ GeV and $|\eta| < 2.5$ (where $X = 30, 50$ GeV).

- Cut 5 (M_T Cut): $M_T < 100$ GeV.

where the transverse mass M_T is defined as the invariant mass of the hardest muon and the E_T^{miss} in the transverse plane.

The same event selection cuts were used except that the ID cut requires a muon rather than a tau. $p_T > 30$ GeV and $p_T > 50$ GeV were chosen for the low p_T and high p_T scenario respectively. The reason for this choice will be explained in the Section 7.5.2. Table 7.3 (Table 7.4) shows the resulting cutflow for the low p_T (high p_T) scenario. Like the τ-channel it can be seen that the $\Delta\phi$ cut and ID cut perform well at controlling the QCD multijet background, which is completely removed for the μ-channel. The remaining background that dominates is again W+jets.

Sample	Events	Cut1-2	Cut3	Cut4	Cut5
Top leptonic	440841	12159.4	10379.3	1602.0	1383.8
Top hadronic	379517	452.7	202.4	0	0
QCD	1635207.6	29615.6	6883.3	0	0
Z+jets	14420.5	1588.2	1346.9	22.5	20.0
W+jets	18720.2	3603.2	3029.7	344.8	322.1
Di-boson	54709.6	21.2	18.2	4.4	3.6
SM Background	2102574.8	35280.9	11480.5	371.7	345.7

Table 7.3: Number of expected events for 1 fb^{-1} after all the selection cuts defined in the text for the low p_T scenario μ-channel. "Top Leptonic" includes all $t\bar{t}$ events with a leptonic decay e.g. dileptonic $t\bar{t}$ events, not just the μ-channel signal events.

Sample	Events	Cut1-2	Cut3	Cut4	Cut5
Top leptonic	440841	12159.4	10379.3	1120.2	957.5
Top hadronic	379517	452.7	202.4	0	0
QCD	1635207.6	29615.6	6883.3	0	0
Z+jets	14420.5	1588.2	1346.9	14.9	12.9
W+jets	18720.2	3603.2	3029.7	233.3	212.0
Di-boson	54709.6	21.2	18.2	2.5	1.7
SM Background	2102574.8	35280.9	11480.5	250.8	226.7

Table 7.4: Number of expected events for 1 fb^{-1} after all the selection cuts defined in the text for the high p_{T} scenario μ-channel. "Top Leptonic" includes all $t\bar{t}$ events with a leptonic decay e.g. dileptonic $t\bar{t}$ events, not just the μ-channel signal events.

7.4.3 Reconstructing the hadronically decaying t-quark

The background events that remain for both the τ-channel and μ-channel after the event selection cuts are those that naturally have the same signature as the respective channel e.g. $W \rightarrow \tau\nu$+jets for the τ-channel or $W \rightarrow \mu\nu$+jets for the μ-channel, or those that are able to fake the signature e.g. $Z \rightarrow \tau\tau$+jets where one of the taus is lost, or QCD multijet events where one of the jets is misreconstructed as a τ and jet mismeasurement presents itself as $E_{\mathrm{T}}^{\mathrm{miss}}$ in the event. Because these events are so similar to the signal they are difficult to reduce further. However, there is one characteristic of the signal for both channels that most of the backgrounds do not share: objects in the final state originate from the decay of top quarks, therefore their invariant mass should be the same as the top quark mass. If the jets from the decay of the hadronically decaying top quark (t_{had}) can be identified, t_{had} can be fully reconstructed and thus a cut can be placed on its mass to remove the remaining background events. In order to do this the three jets from the decay of t_{had} must be identified. To avoid dependence on b-tagging at the beginning of data-taking, methods for reconstructing t_{had} using only the kinematics of the decay to select the correct jets were investigated. The two methods that performed best are described below.

The Highest Vector-Summed p_{T} Method

Due to the high energy of the collisions producing the $t\bar{t}$-pair and their subsequent decay, the decay products of the top quarks are expected to be boosted along the direction that the top quarks are traveling. The first method investigated for reconstructing t_{had} utilises this by selecting the three jets that have the highest vector-summed p_{T}[1]. Figure 7.3 shows the resulting M_{jjj} distribution for both the low p_{T} and high p_{T} scenarios. In both cases a peak can be seen in the M_{jjj} distribution around the expected top quark mass of 175 GeV.

The Minimum ΔR method

The second method for reconstructing t_{had} also uses the assumption that the jets coming from this decay will be boosted and thus looks for the three jets closest together. As a measure of closeness ΔR between the jets is used. The three jets with the minimum ΔR between them are reconstructed as t_{had}. Figure 7.4 shows the resulting M_{jjj} distribution for both the low p_{T} and high p_{T} scenarios. Again, as expected, in both cases a peak can be seen in the M_{jjj} distribution around the expected top quark mass.

It can be seen from Figures 7.3 and 7.4 that these methods of reconstructing t_{had} perform well at separating the $t\bar{t}$ signal from the SM backgrounds. The signal peaks on the left around the top quark mass whereas the backgrounds are pushed to the right. Figure 7.5 shows a comparison between the two methods. On the y-axis is M_{jjj} for the highest vector-summed p_{T} method, on the x-axis is M_{jjj} for the minimum ΔR method. From this figure it can be seen that the minimum ΔR method performs better as it picks up events lost to this high mass tail with the highest vector-summed p_{T} method. The minimum ΔR method will be used for reconstructing t_{had} throughout the rest of this thesis.

To take advantage of the separation of signal and background produced by reconstructing t_{had}, a cut can be placed on M_{jjj} to reject the separated background

---

[1]The vector-summed p_{T} of the jets is the p_{T} of the resulting four-vector created by summing the four-vectors of the jets.
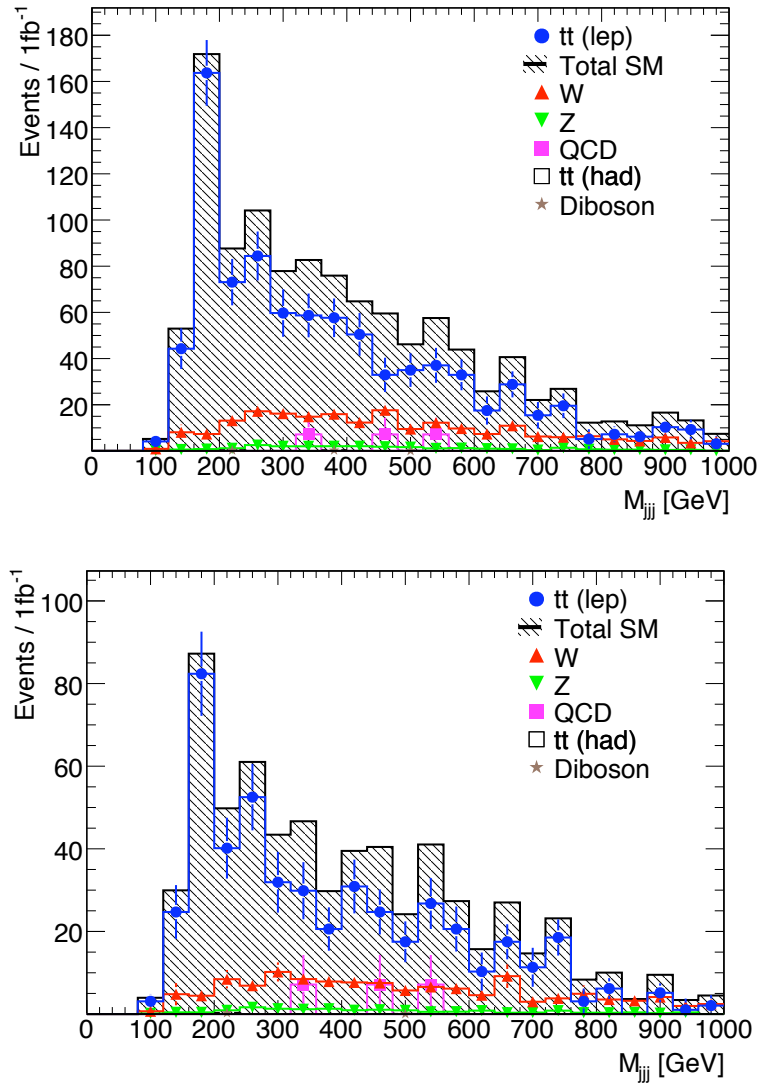
Figure 7.3: Reconstructed t-quark mass (M_{jjj}) distributions where the t-quark is reconstructed using the highest vector summed p_T method for the τ-channel for 1 fb^{-1} of integrated luminosity. Top: low p_T scenario, bottom: high p_T scenario.
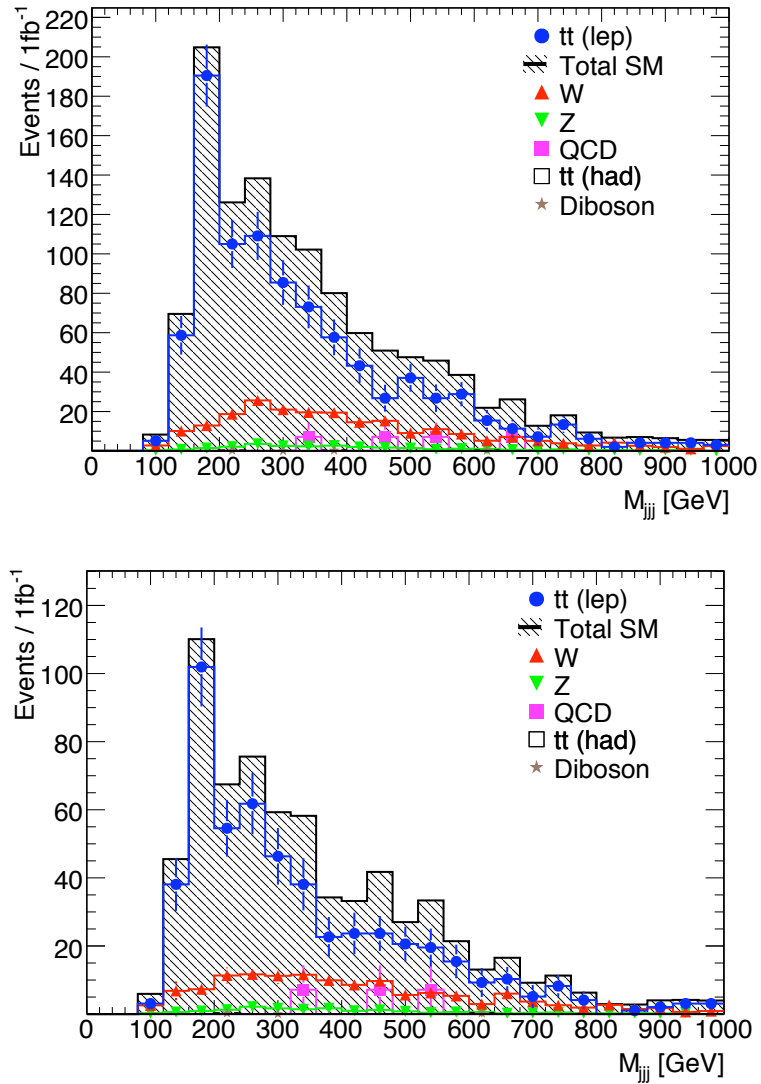
Figure 7.4: Reconstructed t-quark mass (M_{jjj}) distributions where the t-quark is reconstructed using the minimum ΔR method for the τ-channel for 1 fb^{-1} of integrated luminosity. Top: low p_{T} scenario, bottom: high p_{T} scenario.
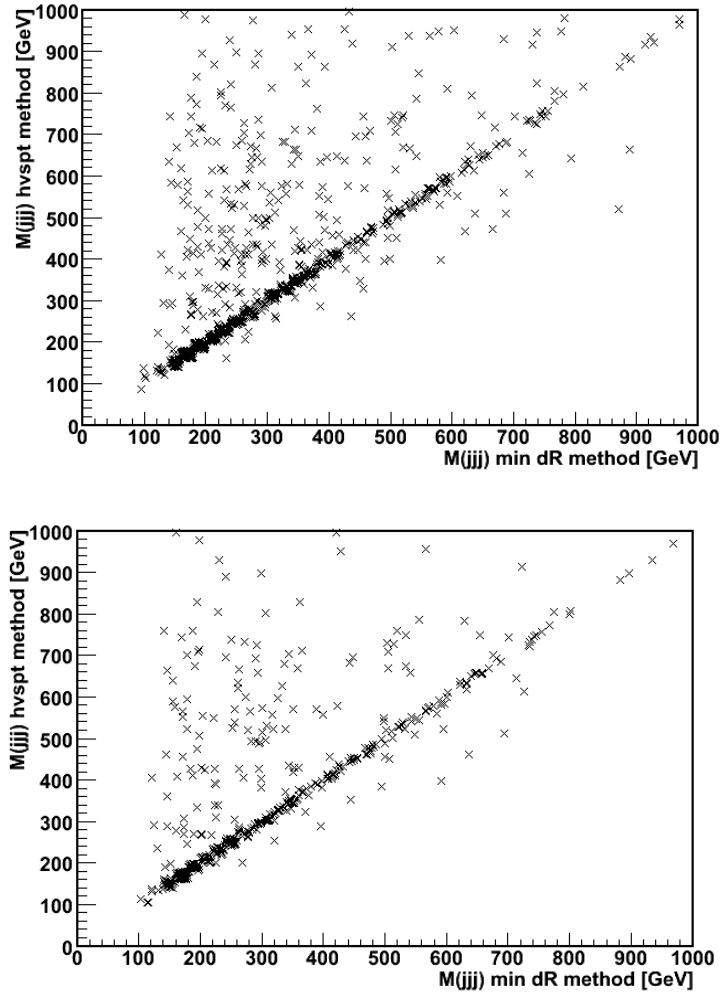
Figure 7.5: Comparison of the two methods used to reconstruct hadronically decaying t-quark for the τ-channel. On the y-axis is M_{jjj} reconstructed using the highest vector summed p_T method and on the x-axis M_{jjj} reconstructed using the minimum ΔR method. Top: low p_T scenario, bottom: high p_T scenario.

events. Figure 7.6 shows the reconstructed top quark mass peak for the low p_T scenario τ-channel and the effect on the signal-to-background ratio (S/B) of varying the size of the window of the cut placed on M_{jjj} around this peak. A tighter mass cut gives a better signal to background ratio since it rejects more of the SM background, but it can also significantly reduce the number of signal events. For this study a compromise must be made between having a good signal to background ratio to reject as much of the remaining Standard Model background as possible and having enough statistics to perform the tau identification measurement. For the purpose of this study, in order to have a reasonable S/B ratio but enough statistics, a cut of 120 GeV $< M_{jjj} <$ 240 GeV was selected. It is clear that this cut can be optimized in future studies. In the end the mass window chosen should be the one that gives the lowest uncertainty on the tau identification efficiency.

Table 7.5 shows the number of signal events (S) and the number of background events (B) along with the signal-to-background ratio (S/B) for both the τ- and μ-channels in this mass window. Note that here "signal" refers to the number of leptonic $t\bar{t}$ events surviving the event selection. This contains real τ-channel (μ-channel) signal events but also contamination from other leptonic events such as e-channel events and dileptonic events. This will be addressed in Section 7.5.1.

Channel	S	B	S/B	$S/\sqrt{B}$
τ-channel, low p_T	354.2	46.3	7.6	52.0
τ-channel, high p_T	194.6	28.5	6.8	36.5
μ-channel, low p_T	565.2	60.5	9.3	72.7
μ-channel, high p_T	383.0	37.0	10.3	63.0

Table 7.5: Signal (S) and SM background (B) after mass window cut for τ- and μ-channels for both p_T scenarios. Events are normalised to 1fb^{-1} . Note that here "signal" refers to the number of leptonic $t\bar{t}$ events surviving the event selection
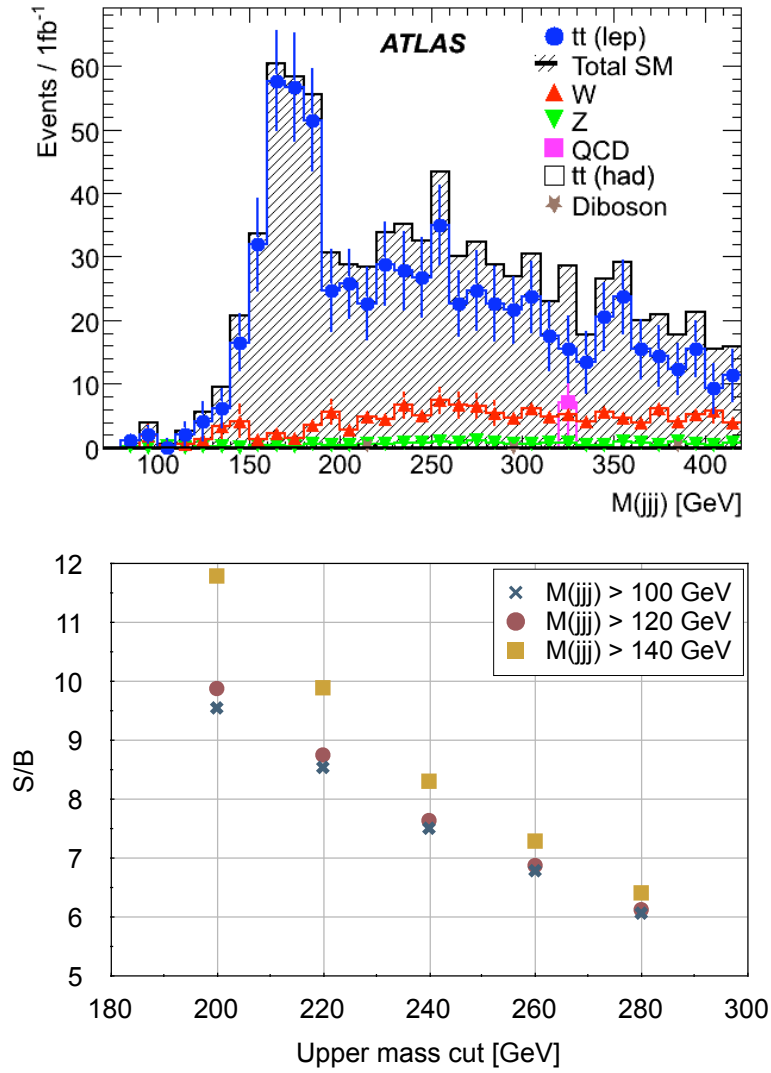
Figure 7.6: Mass window cut selection. Top: The peak in the M(jjj) distribution for the low p_T scenario τ-channel for 1 fb^{-1} . Bottom: The variation of signal to background ratio (S/B) for the low p_T scenario τ-channel when the upper mass cut is varied while the lower mass cut is fixed to: 100 GeV, 120 GeV and 140 GeV.

7.5 The Method in Practice

Equation 7.3 contains terms that can be measured directly from data, for example, the branching ratios are well known from previous experiments and the muon identification efficiency will be measured in early data, but it also contains terms that require additional information from the Monte Carlo simulations. These terms are described in detail below.

7.5.1 Measuring the number of expected events for each channel, N_{exp}

$N_{exp.}$ is the number of real signal events in the isolated sample once background events from other physics processes have been removed. In this study the Monte Carlo data is used to model the background events and then these events are subtracted from the corresponding channel samples. In future work it is hoped that data-driven methods can be employed to model the backgrounds.

Table 7.6 shows the number of expected events, the number of measured events and the number of background events for the τ-channel for the low p_T and high p_T scenarios.

Events	Low p_T scenario	High p_T scenario
N_{exp}^{τ}	202.8	112.2
N_{meas}^{τ}	397.4	222.1
N_{bkg}^{τ}	194.6	109.8

Table 7.6: The number of expected events, the number of measured events and the number of background events for the τ-channel are shown for the low p_T scenario and high p_T scenarios for 1 fb^{-1} of integrated luminosity.

As already mentioned, any physical process that produces or fakes a signature of a tau, at least four jets and $E_\mathrm{T}^\mathrm{miss}$ has the potential to be a background for the τ-channel. It is also possible that real τ-channel events become a background e.g. if the tau is lost but one of the jets is misreconstructed as a tau. These events

are real τ-channel events but they are unwanted since the tau surviving the event selection is not real. Backgrounds in the τ-channel can be classified as follows:

- N_{bkgSM}^{τ}: Background from other Standard model processes that produce or fake the same signature as the signal e.g. W+jets, Z+jets and dileptonic $t\bar{t}$.

- N_{bkgPS}^{τ}: Real τ-channel events where the reconstructed τ is in the phase space defined on reconstruction level i.e. $p_\mathrm{T} > 20$ GeV and $|\eta| < 2.5$ for the low p_T scenario and $p_\mathrm{T} > 40$ GeV and $|\eta| < 2.5$ for the high p_T scenario, but comes from a true τ that is outside the phase space defined for the signal on truth level i.e. $p_\mathrm{T} > 15$ GeV and $|\eta| < 2.5$ for the low p_T scenario and $p_\mathrm{T} > 30$ GeV and $|\eta| < 2.5$ for the high p_T scenario.

- $N_{bkgTauFake}^{\tau}$: Real τ-channel events where the true τ is not reconstructed, and the reconstructed τ seen is fake i.e. is a misreconstructed jet or electron. The true τ is in the correct phase space defined for the signal so if it had been reconstructed this event would be classed as signal.

- $N_{bkgPSTauFake}^{\tau}$: The events are the same as those in $N_{bkgTauFake}$ except the true τ is outside the phase space defined for the signal. So even if the true τ had been reconstructed this event would still not be classed as signal because the τ is outside the defined phase space for signal.

- $N_{bkgJetFakeTauFake}^{\tau}$: These events are the same as in $N_{bkgFakeTau}$ except one of the four hardest jets is also fake and is actually the τ.

Table 7.7 summarises the number of events for each type of background for the τ-channel for both the low p_T and high p_T scenarios. Table 7.8 shows the composition of N_{bkgSM} for the τ-channel. It can be seen that the largest background comes from misreconstruction of semileptonic $t\bar{t}$ decays to an e-final state. For the low p_T scenario (high p_T scenario) 97% (98%) of this background is due to the electron being misreconstructed as a tau. The rest is due to a jet being misreconstructed as a tau and the electron being lost. It should be possible to remove the events where an electron is misreconstructed as a tau with an electron-tau

separation tool. This would significantly reduce the background to the τ-channel. Unfortunately, no such tool was available in Athena version 12 but an electron veto in Athena version 14 will be used in the update of the analysis using the 10 TeV MC samples (see Chapter 8).

Background	Low p_T scenario	High p_T scenario
N^τ_{bkgSM}	187.4	103.7
N^τ_{bkgPS}	1.0	1.0
$N^\tau_{bkgTauFake}$	1.0	1.0
$N^\tau_{bkgPSTauFake}$	4.1	2.1
$N^\tau_{bkgJetFakeTauFake}$	1.0	2.1
N^τ_{bkg} (Total)	194.6	109.8

Table 7.7: Breakdown of the background in the τ-channel for the low p_T and high p_T scenarios for 1 fb^{-1} of integrated luminosity.

SM Background	Low p_T scenario	High p_T scenario
Semileptonic $t\bar{t}$ to e-final state	112.2	61.8
Semileptonic $t\bar{t}$ to μ-final state	15.4	4.1
Hadronic $t\bar{t}$	0	0
Dileptonic $t\bar{t}$	13.4	9.3
QCD multijet	0	0
Z+jets	4.3	2.7
W+jets	41.7	25.5
Diboson	0.3	0.3

Table 7.8: The breakdown of N_{bkgSM} for the τ-channel. The number of events for each type of background is shown for the low p_T and high p_T scenarios for 1 fb^{-1} of integrated luminosity.

Table 7.9 shows the number of expected events, the number of measured events and the number of background events for the μ-channel for the low p_T and high

p_T scenarios. For the μ-channel the background comes solely from other SM processes that produce or fake the same signature as the signal e.g. W+jets, Z+jets and dileptonic $t\bar{t}$. Since the muon has a very low chance of being misreconstructed compared to the tau, there are no backgrounds from real signal events that have been misreconstructed as there are for the τ-channel. Table 7.10 summarises the composition of the SM background for the μ-channel. All backgrounds are small in comparison to the τ-channel again due to the fact that a muon is less likely to be misreconstructed.

Events	Low p_T scenario	High p_T scenario
N^μ_{exp}	538.5	364.5
N^μ_{meas}	625.7	420.0
N^μ_{bkg}	87.3	55.5

Table 7.9: The number of expected events, the number of measured events and the number of background events for the μ-channel are shown for the low p_T and high p_T scenarios for 1 fb^{-1} of integrated luminosity.

SM Background	Low p_T scenario	High p_T scenario
Semileptonic $t\bar{t}$ to τ-final state	0	0
Semileptonic $t\bar{t}$ to e-final state	0	0
Hadronic $t\bar{t}$	0	0
Dileptonic $t\bar{t}$	26.8	18.5
QCD multijet	0	0
Z+jets	2.7	1.5
W+jets	56.5	34.1
Diboson	1.4	1.4

Table 7.10: Breakdown of N_{bkgSM} for the μ-channel for the low p_T and high p_T scenarios for 1fb^{-1} of integrated luminosity.

7.5.2 Measuring the ratio $\frac{\varepsilon^{\mu}_{cuts}}{\varepsilon^{\tau}_{cuts}}$

The ratio $\frac{\varepsilon^{\mu}_{cuts}}{\varepsilon^{\tau}_{cuts}}$ is the ratio of the efficiency of the event selection cuts used to select the signal events for each channel. It can be expanded in terms of the individual cut efficiencies as follows:

$$\frac{\varepsilon^{\mu}_{cuts}}{\varepsilon^{\tau}_{cuts}} = \frac{\varepsilon^{\mu}_{PS}}{\varepsilon^{\tau}_{PS}} \times \frac{\varepsilon^{\mu}_{jets}}{\varepsilon^{\tau}_{jets}} \times \frac{\varepsilon^{\mu}_{E^{\mathrm{miss}}_{\mathrm{T}}}}{\varepsilon^{\tau}_{E^{\mathrm{miss}}_{\mathrm{T}}}} \times \frac{\varepsilon^{\mu}_{\Delta\phi}}{\varepsilon^{\tau}_{\Delta\phi}} \times \frac{\varepsilon^{\mu}_{M_T}}{\varepsilon^{\tau}_{M_T}} \times \frac{\varepsilon^{\mu}_{M_{jjj}}}{\varepsilon^{\tau}_{M_{jjj}}} \qquad (7.6)$$

The semileptonic $t\bar{t}$ events are divided into τ-channel and μ-channel events according to the branching ratios for these channels. Since only events for each channel with a certain lepton p_{T} and $|\eta|$ are selected, only a subset of the total events for each channel are taken. ε_{PS} refers to the efficiency of the selection of this phase space subset for each channel.

Apart from the ID cut the same event selection cuts are applied to the μ-channel and the τ-channel. As described previously, aside from the lepton flavour the τ-channel and the μ-channel are expected to be identical if the leptons have the same phase space, therefore it is expected that the efficiencies of the cuts not involving the lepton or its decay products i.e. the jets cut and the M_{jjj} cut, should be the same in both channels and thus the ratios for these cuts should be one. If this is true, Equation 7.6 can be simplified to:

$$\frac{\varepsilon^{\mu}_{cuts}}{\varepsilon^{\tau}_{cuts}} = \frac{\varepsilon^{\mu}_{PS}}{\varepsilon^{\tau}_{PS}} \times 1 \times \frac{\varepsilon^{\mu}_{E^{\mathrm{miss}}_{\mathrm{T}}}}{\varepsilon^{\tau}_{E^{\mathrm{miss}}_{\mathrm{T}}}} \times \frac{\varepsilon^{\mu}_{\Delta\phi}}{\varepsilon^{\tau}_{\Delta\phi}} \times \frac{\varepsilon^{\mu}_{M_T}}{\varepsilon^{\tau}_{M_T}} \qquad (7.7)$$

A similar cancellation of the cuts involving $E^{\mathrm{miss}}_{\mathrm{T}}$ (the $E^{\mathrm{miss}}_{\mathrm{T}}$ cut, the $\Delta\phi$ cut and the M_T cut) cannot be made since the tau has intrinsic $E^{\mathrm{miss}}_{\mathrm{T}}$ due to its subsequent decay to neutrinos, thus events with taus will have a different efficiency for these cuts. Therefore it is expected that if the muons and the taus have the same phase space only a factor for the ratio of the cuts involving $E^{\mathrm{miss}}_{\mathrm{T}}$ needs to be determined.

Tau reconstruction is performed on the visible decay products of the tau, therefore the reconstructed tau will have a lower p_{T} than the true tau had before it decayed. It follows that the reconstructed tau will therefore always have a p_{T}

lower than a muon with the same p_T as the tau before its decay. Therefore in order to test the above hypothesis the p_T of the tau that corresponds to a given muon p_T must be found in order that the same phase space can be selected for the τ-channel and the μ-channel.
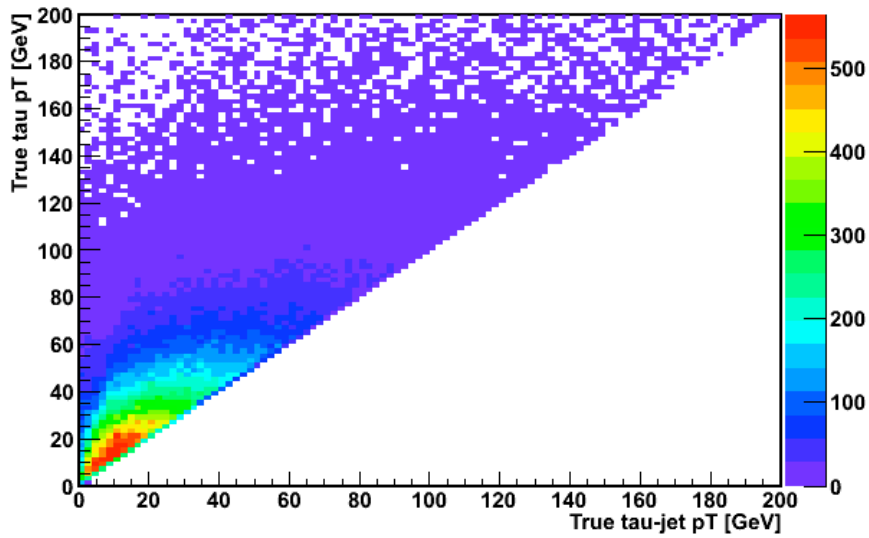
Figure 7.7: The p_T of the true taus as a function of the p_T of their corresponding true tau-jets. The corresponding true-tau jet is the tau-jet that is closest in ΔR to the true tau.

The Monte Carlo contains two types of tau objects on truth level:

- True taus: These are the tau objects generated by the MC prior to their decay. These objects are comparable to the electron truth objects and muon truth objects in the Monte Carlo.

- True tau-jets: These objects contain only the visible parts of the true tau decay products. These objects are comparable to the tau-jets that are reconstructed.

Figure 7.7 shows the p_T of the true taus as a function of the p_T of the true tau-jets in the Monte Carlo. It can be seen from the figure that there is little correlation

between the p_Ts of these objects. This implies that it is not possible to say what p_T a tau-jet will have given the p_T of the tau before it decayed. As a result, it is not easy to say what the corresponding p_T of a muon should be for a certain value of reconstructed tau p_T. Since the phase space of the muons and the taus cannot be matched exactly there will be some error associated with the assumption that the jets in the two channels will be identical. To determine how reasonable it is to still make this assumption the truth information was used to select real signal events in the Monte Carlo for each channel. The event selection cuts were then applied to these events and the efficiency of each cut was calculated. Figure 7.8 shows the combined ratio of the efficiencies of the cuts involving jets (the jets cut and the M_{jjj} cut) as a function of the reconstructed muon p_T for the two p_T scenarios of the taus. It can be seen that over the range of p_Ts selected, with a systematic error of $\pm 10\%$, the ratio of the efficiencies is one as predicted. So within this p_T range the assumption can be made that the efficiencies of the cuts involving the jets do cancel.

The E_T^{miss} of the τ-channel is different to that of the μ-channel due to the extra neutrinos from the tau decay, so the ratio of the efficiencies between the two channels for the cuts involving E_T^{miss} must be taken from the Monte Carlo. The systematic uncertainty on this term will come from how well the Monte Carlo describes the E_T^{miss} efficiency with respect to data. This can only be estimated with data. For this study an estimated conservative value of 10% was taken as the overall systematic uncertainty on this term.

Table 7.11 (Table 7.12) shows the efficiency of each selection cut for the real signal events for the τ- and μ-channels for the low p_T (high p_T) scenario. It can be seen that for this particular phase space the ratio $\frac{\varepsilon_{M_T}^{\mu}}{\varepsilon_{M_T}^{\tau}}$ is approximately one for both p_T scenarios. The ratio $\frac{\varepsilon_{E_T^{\mathrm{miss}}}^{\mu}}{\varepsilon_{E_T^{\mathrm{miss}}}^{\tau}} \times \frac{\varepsilon_{\Delta\phi}^{\mu}}{\varepsilon_{\Delta\phi}^{\tau}}$ is 0.75 ± 0.08 (0.72 ± 0.07) for the low p_T (high p_T) scenario, neglecting the statistical uncertainties.

Table 7.13 summarises the values of the efficiency terms for the low p_T and high p_T scenarios.
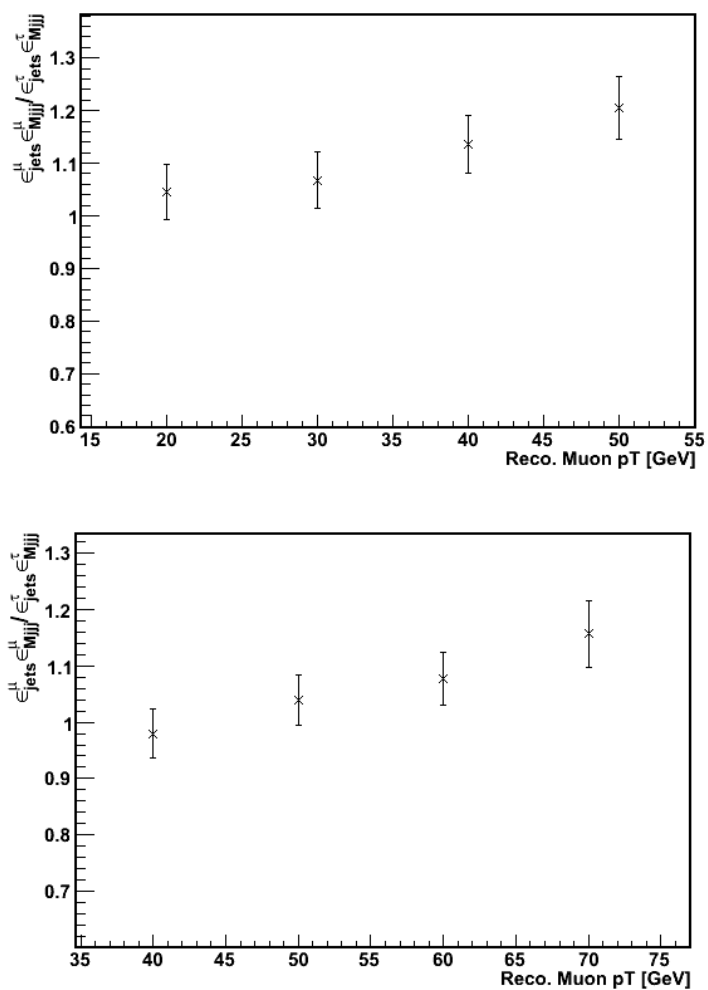
Figure 7.8: The combined ratio of the efficiencies of the cuts involving jets (the jets cut and the M_{jjj} cut) as a function of the reconstructed muon p_T for the low p_T scenario (top) and for the high p_T scenario (bottom) for 1 fb^{-1} . The error bars indicate the statistical uncertainties.

Cut Efficiency	τ-channel	μ-channel	Ratio $\frac{\mu}{\tau}$
ε_{jets}	0.116 ± 0.001	0.120 ± 0.001	1.03 ± 0.012
$\varepsilon_{M_{jjj}}$	0.398 ± 0.007	0.404 ± 0.005	1.015 ± 0.022
$\varepsilon_{E_{\mathrm{T}}^{\mathrm{miss}}}$	0.280 ± 0.010	0.207 ± 0.006	0.739 ± 0.034
$\varepsilon_{\Delta\phi}$	0.888 ± 0.013	0.903 ± 0.009	1.017 ± 0.018
ε_{ID}	0.371 ± 0.021	0.608 ± 0.016	1.639 ± 0.102
ε_{M_T}	0.995 ± 0.007	0.967 ± 0.008	0.972 ± 0.011

Table 7.11: The efficiency of each selection cut (low p_{T} scenario), for each channel, when applying the cuts to real signal events in the Monte Carlo. Numbers are shown for $1\mathrm{fb}^{-1}$ of integrated luminosity. The uncertainties given are statistical uncertainties.

Cut Efficiency	τ-channel	μ-channel	Ratio
ε_{jets}	0.123 ± 0.002	0.127 ± 0.001	1.032 ± 0.019
$\varepsilon_{M_{jjj}}$	0.393 ± 0.009	0.408 ± 0.006	1.038 ± 0.028
$\varepsilon_{E_{\mathrm{T}}^{\mathrm{miss}}}$	0.289 ± 0.013	0.210 ± 0.007	0.727 ± 0.041
$\varepsilon_{\Delta\phi}$	0.907 ± 0.015	0.894 ± 0.012	0.986 ± 0.021
ε_{ID}	0.330 ± 0.026	0.613 ± 0.020	1.858 ± 0.158
ε_{M_T}	0.991 ± 0.012	0.964 ± 0.010	0.973 ± 0.016

Table 7.12: The efficiency of each selection cut (high p_{T} scenario), for each channel, when applying the cuts to real signal events in the Monte Carlo. Numbers are shown for $1\mathrm{fb}^{-1}$ of integrated luminosity. The uncertainties given are statistical uncertainties.

Cut Efficiency	Low p_{T} scenario	High p_{T} scenario
$\frac{B^{\mu}}{B^{\tau}}\frac{\varepsilon_{PS}^{\mu}}{\varepsilon_{PS}^{\tau}}$	2.1	2.3
$\frac{\varepsilon_{jets}^{\mu}\varepsilon_{M_{jjj}}^{\mu}}{\varepsilon_{jets}^{\tau}\varepsilon_{M_{jjj}}^{\tau}}$	1.0	1.0
$\frac{\varepsilon_{E_{\mathrm{T}}^{\mathrm{miss}}}^{\mu}\varepsilon_{\Delta\phi}^{\mu}}{\varepsilon_{E_{\mathrm{T}}^{\mathrm{miss}}}^{\tau}\varepsilon_{\Delta\phi}^{\tau}}$	0.75	0.72
$\frac{\varepsilon_{M_T}^{\mu}}{\varepsilon_{M_T}^{\tau}}$	1.0	1.0

Table 7.13: The efficiency of each selection cut. Numbers are shown for the low p_{T} and high p_{T} scenarios.

7.5.3 Taking the μ-identification efficiency from Monte Carlo

With 100 pb^{-1} of data it is expected that the μ-identification efficiency will be known with a precision of $\sim 1\%$ and so the μ-identification efficiency will be taken from data. For the purpose of this study on Monte Carlo data, the μ-identification efficiency is taken from the Monte Carlo itself. Two μ-identification efficiencies are extracted; one for the low p_T scenario and one for the high p_T scenario, as follows:

1. Low p_T scenario: The μ-identification efficiency is the probability that truth muons with $p_T > 20$ GeV and $|\eta| < 2.5$ are reconstructed as muons with $p_T > 30$ GeV and $|\eta| < 2.5$.

2. High p_T scenario: The μ-identification efficiency is the probability that truth muons with $p_T > 40$ GeV and $|\eta| < 2.5$ are reconstructed as muons with $p_T > 50$ GeV and $|\eta| < 2.5$.

The μ-identification efficiencies in the Monte Carlo are extracted using the real signal events defined in the previous section. All event selection cuts, except the M_T cut and the ID cut, are applied to these events to get the number of truth muons with $p_T > X_{truth}$ (where $X_{truth} = 20$ GeV for the low p_T scenario and 40 GeV for the high p_T scenario) and $|\eta| < 2.5$. The ID cut is then applied to the events and truth matching is performed between the reconstructed muons and the truth muons to get the number of truth muons with $p_T > X_{truth}$ reconstructed as muons with $p_T > X_{reco}$ (where $X_{reco} = 30$ GeV for the low p_T scenario and 50 GeV for the high p_T scenario). The truth matching matches the reconstructed muon to the truth object that is closest in ΔR to the reconstructed muon. The results of the μ-identification efficiency extraction are summarised in Table 7.14.

p_T scenario	All cuts except ID cut	ID cut and truth matching	μ-ID efficiency
Low p_T	912.2	554.9	0.61 ± 0.02
High p_T	614.7	376.8	0.61 ± 0.02

Table 7.14: Number of events after applying all cuts except the ID cut and the M_{T} cut, and after applying the ID cut in addition to applying truth matching, and the resulting μ-ID efficiencies. Numbers are shown for both the low and high p_T scenarios for 1fb^{-1} of integrated luminosity. The uncertainties given are the statistical uncertainties.

7.6 Results

7.6.1 The Tau Identification Efficiency

Using the numbers derived in the previous sections the tau identification efficiency can be calculated for both the low p_{T} and high p_{T} scenarios. Table 7.15 summarises the values derived for each term in Equation 3 and the resulting tau identification efficiencies.

Term	Low p_T scenario	High p_T scenario
$N_{exp.}^{\tau}$	202.8	112.2
$N_{exp.}^{\mu}$	538.5	364.5
$\frac{B^{\mu}}{B^{\tau}} \frac{\varepsilon_{PS}^{\mu}}{\varepsilon_{PS}^{\tau}}$	2.1	2.3
$\frac{\varepsilon_{cuts}^{\mu}}{\varepsilon_{cuts}^{\tau}}$	0.75	0.72
ε_{ID}^{μ}	0.61	0.61
ε_{ID}^{τ}	0.36	0.31

Table 7.15: Summary of the values for each term contributing to the τ-identification efficiency for both the low p_T and high p_T scenarios for 1fb^{-1} of integrated luminosity.

To check that this method correctly reproduces the tau identification efficiency of the MC, the actual tau identification efficiency of the MC can be extracted in the same way that the muon identification efficiency was determined in Section 7.5.3. All event selection cuts, except the M_{T} cut and the ID cut, were applied to the real τ-channel signal events to get the number of true taus after cuts with

$p_\mathrm{T} > X_{truth}$ (where $X_{truth} = 15$ GeV for the low p_T scenario and 30 GeV for the high p_T scenario) and $|\eta| < 2.5$. The ID cut was then applied to the events and the truth matching was performed between the reconstructed taus and the true taus to get the number of true taus with $p_T > X_{truth}$ reconstructed as taus with $p_\mathrm{T} > X_{reco}$ (where $X_{reco} = 20$ GeV for the low p_T scenario and 40 GeV for the high p_T scenario). The truth matching matches the reconstructed tau to the truth object that is closest in ΔR to the reconstructed tau. The results are summarised in Table 7.16.

p_T scenario	All cuts except ID cut	ID cut and truth matching	τ-ID efficiency
Low p_T	548.8	203.9	0.37 ± 0.02
High p_T	831.9	395.4	0.33 ± 0.03

Table 7.16: Number of events for 1 fb^{-1}, after applying all cuts except the ID cut and M_T cut, and after applying the ID cut in addition to truth matching, and the resulting τ-ID efficiencies of the MC. Numbers are shown for both the low and high p_T scenarios. The uncertainties given are statistical uncertainties.

7.6.2 The Uncertainty on the Tau Identification Efficiency

Table 7.17 summarises both the statistical and systematic uncertainties that contribute to the final tau identification efficiency for both the low p_T and high p_T scenarios. The statistical uncertainties on N_{meas} and N_{bkg} for each channel are given by $\sqrt{N_{meas}}$ and $\sqrt{N_{bkg}}$ respectively. The statistical uncertainty on the muon identification efficiency and on the ratio of the efficiency of the selection cuts in each channel can be safely neglected.

The systematic uncertainty on N_{bkg} is given by the sum in quadrature of the uncertainties of the individual backgrounds. A 50% systematic uncertainty was taken for all SM backgrounds and a 100% systematic uncertainty was taken for the other backgrounds coming from real signal events that are wrongly reconstructed or have the wrong phase space. The main backgrounds that contribute

are W+jet events and semileptonic $t\bar{t}$ decays to an electron final state. In data the uncertainty on the background from semileptonic $t\bar{t}$ decays to an electron final state, caused by misidentification of an electron as a tau, will be estimated using very clean $Z \rightarrow ee$ events where one electron is tagged and the other electron is used to measure the probability that an electron fakes a tau. The number of semileptonic $t\bar{t}$ events where an electron fakes a tau will then be estimated by measuring the real number of semileptonic $t\bar{t}$ to an electron final state events in data and correcting the number for the electron inefficiency and applying the probability that an electron fakes a tau. Using such a method it is assumed the background from $t\bar{t}$ events can be estimated with a systematic uncertainty of $\pm 15\%$.

Term	Low p_T scenario	High p_T scenario
$N^{\tau}_{meas.}$	$397.4 \pm 19.9 \pm -$	$222.1 \pm 14.9 \pm -$
$N^{\mu}_{meas.}$	$625.7 \pm 25.0 \pm -$	$420.0 \pm 20.5 \pm -$
$N^{\tau}_{bkg.}$	$194.6 \pm 13.9 \pm 28.2$	$109.8 \pm 10.5 \pm 16.8$
$N^{\mu}_{bkg.}$	$87.3 \pm 9.3 \pm 31.3$	$55.5 \pm 7.4 \pm 19.4$
$(\varepsilon^{\mu}_{cuts}/\varepsilon^{\tau}_{cuts})$	$0.75 \pm - \pm 0.08$	$0.72 \pm - \pm 0.07$
ε^{μ}_{ID}	0.61	0.61
ε^{τ}_{ID}	$0.36 \pm 0.04 \pm 0.07$	$0.31 \pm 0.05 \pm 0.06$

Table 7.17: The terms that contribute to the τ-identification efficiency with their statistical and systematic uncertainties respectively for 1fb^{-1} of integrated luminosity. Where no uncertainty is given the contribution of this uncertainty can be safely neglected.

Tables 7.18 and 7.19 summarise the uncertainties of the SM background contributions relative to the total uncertainty on the SM background. It can be seen that the uncertainty on the background for the τ-channel is dominated by the semileptonic $t\bar{t}$ decays to an electron final state and the W+jets events. As already mentioned, in future studies it is believed that the background contribution from the semileptonic electron final state events can be significantly reduced with the use of electron-tau separation tools (as will be shown in Chapter 8). Thus the background uncertainty would depend mainly on the W+jets contribution.

Term	Uncertainty low p_T scenario [%]		Uncertainty high p_T scenario [%]	
	Statistical	Systematic	Statistical	Systematic
Semileptonic $t\bar{t}$ to e-final state	5.4	8.6	7.2	8.4
Semileptonic $t\bar{t}$ to μ-final state	2.0	1.2	1.8	0.6
Hadronic $t\bar{t}$	–	–	–	–
Dileptonic	1.9	3.4	2.8	4.2
QCD multijet	–	–	–	–
Z+jets	1.1	1.1	1.5	1.2
W+jets	3.3	10.7	4.6	11.6
Diboson	0.3	0.1	0.5	0.1
N^{τ}_{bkgPS}	0.5	0.5	0.9	0.9
$N^{\tau}_{bkgTauFake}$	0.5	0.5	0.9	0.9
$N^{\tau}_{bkgPSTauFake}$	1.0	2.1	1.3	1.9
$N^{\tau}_{bkgJetFakeTauFake}$	0.5	0.5	1.3	1.9

Table 7.18: The uncertainties of the individual SM background contributions relative to the total uncertainty of the SM background for the τ-channel for 1 fb^{-1} of integrated luminosity.

Term	Uncertainty low p_T scenario [%]		Uncertainty high p_T scenario [%]	
	Statistical	Systematic	Statistical	Systematic
Semileptonic $t\bar{t}$ to e-final state	–	–	–	–
Semileptonic $t\bar{t}$ to τ-final state	–	–	–	–
Hadronic $t\bar{t}$	–	–	–	–
Dileptonic	5.9	15.3	7.7	16.7
QCD multijet	–	–	–	–
Z+jets	1.9	1.5	2.2	1.4
W+jets	8.6	32.4	10.5	30.7
Diboson	1.4	0.8	2.1	1.3

Table 7.19: The uncertainties of the individual SM background contributions relative to the total uncertainty of the SM background for the μ-channel for 1 fb^{-1} of integrated luminosity.

The uncertainty on the ratio of the efficiency of the event selection cuts for the two channels is the sum in quadrature of the uncertainty for the jets cuts and the uncertainty for the $E_\mathrm{T}^\mathrm{miss}$ cuts, previously discussed in Section 7.5.2 to be 10% for both contributions.

Comparing the measured tau identification efficiencies with the tau identification efficiencies extracted from the MC, it can be seen that the results agree well within the errors.

7.7 Testing the Method

In order to test the method, pseudo-data was produced with reduced tau identification efficiencies. The identification efficiencies were reduced by removing tau objects in the MC. If a reconstructed tau was found that was matched to a true tau, a random number was generated and if the number was below X the reconstructed tau object was removed, and if it was above X the tau object was kept. This results in a reduction of the MC tau identification efficiency of $\sim X\%$.

Table 7.20 shows the tau identification efficiencies extracted from the MC.

p_T scenario	Reduction (%)	Extracted ID eff.
Low p_T	30	0.24
Low p_T	20	0.29
High p_T	30	0.21
High p_T	20	0.25

Table 7.20: The τ-ID efficiencies extracted from the Monte Carlo for both the low p_T and high p_T scenarios.

Table 7.21 (Table 7.22) summarises the results of the measurement of the tau identification efficiency using the method presented in this thesis, when the tau identification efficiency of the MC is reduced by 30% (20%) for the low p_T and high p_T scenarios. Comparing the extracted identification efficiencies in Table

7.20 and the measured values in Tables 7.21 and 7.22, it can be seen that there is good agreement.

Term	Low p_T scenario	High p_T scenario
$N_{exp.}^{\tau}$	136.9	76.2
$N_{exp.}^{\mu}$	536.4	363.4
$\frac{B^{\mu}\,\varepsilon_{PS}^{\mu}}{B^{\tau}\,\varepsilon_{PS}^{\tau}}$	2.1	2.3
$\frac{\varepsilon_{cuts}^{\mu}}{\varepsilon_{cuts}^{\tau}}$	0.76	0.74
ε_{ID}^{μ}	0.61	0.61
ε_{ID}^{τ}	$0.25\pm0.04 \pm 0.06$	$0.22\pm0.05 \pm 0.05$

Table 7.21: Summary of the values contributing to the τ-identification efficiency for 1 fb^{-1} for both the low p_T and high p_T scenarios when the τ-identification efficiency of the Monte Carlo is reduced by 30%. The measured τ-identification efficiencies are given with statistical and systematic uncertainties respectively for 1 fb^{-1} of integrated luminosity.

7.8 Summary and Conclusions

A new method for measuring the tau identification efficiency in data using a sample of semileptonic $t\bar{t}$ events has been presented. The method isolates the semileptonically decaying $t\bar{t}$ events by requiring high missing transverse energy and a number of high energy jets and by reconstructing the mass of the hadronically decaying t-quark. As a result, this method does not suffer from a large background from QCD multijet events and it does not require tau triggering. It also does not rely on b-tagging to reconstruct the top quark mass and is thus a promising method for early data. The method has been tested using pseudo-data with reduced tau identification efficiencies and good agreement was found between the measured tau identification efficiencies and those expected. The statistical and systematic uncertainties on the tau identification efficiency measurement have been shown to be $\pm11\%$ ($\pm16\%$) and $\pm19\%$ ($\pm19\%$) respectively for taus with $p_T > 20$ GeV ($p_T > 40$ GeV) assuming an integrated luminosity of 1 fb^{-1} at $\sqrt{s} = 14$ TeV.

Term	Low p_T scenario	High p_T scenario
$N^{\tau}_{exp.}$	163.7	87.5
$N^{\mu}_{exp.}$	536.4	363.4
$\frac{B^{\mu}}{B^{\tau}} \frac{\varepsilon^{\mu}_{PS}}{\varepsilon^{\tau}_{PS}}$	2.1	2.3
$\frac{\varepsilon^{\mu}_{cuts}}{\varepsilon^{\tau}_{cuts}}$	0.76	0.74
ε^{μ}_{ID}	0.61	0.61
ε^{τ}_{ID}	0.30±0.04 ± 0.06	0.25±0.05 ± 0.06

Table 7.22: Summary of the values contributing to the τ-identification efficiency for 1 fb^{-1} for both the low p_T and high p_T scenarios when the τ-identification efficiency of the Monte Carlo is reduced by 20%. The measured τ-identification efficiencies are given with statistical and systematic uncertainties respectively for 1 fb^{-1} of integrated luminosity.

Chapter 8

Measuring the tau identification efficiency using $t\bar{t}$ events for a centre-of-mass energy of 10 TeV

The studies detailed in this chapter have been published in an ATLAS internal note, Ref: [83].

8.1 Introduction

A new method for measuring the tau identification efficiency using $t\bar{t}$ events was introduced in the previous chapter. This chapter investigates the suitability of this method for the early data taking phase of the ATLAS experiment when the centre-of-mass energy of the LHC is 10 TeV. These studies will focus on an integrated luminosity of 200 pb^{-1} .

8.2 Experimental Setup

8.2.1 Monte Carlo Samples

The Monte Carlo samples used in this study were produced with Athena version 14 to model a centre of mass energy of 10 TeV. All samples, except those modeling QCD multijet processes are based on a full simulation of the ATLAS detec-

tor using the GEANT4 program, the QCD multijet samples were produced with ATLFAST2. All samples were generated with a top quark mass of 172.5 GeV. The samples are described in Section 4.4.2.

8.2.2 Trigger

As discussed in Chapter 7, due to the rich final state topology of $t\bar{t}$ events and the relatively strong cuts applied in this analysis (see Section 8.3) the trigger efficiency is expected to be high. With multijet and $E_{\mathrm{T}}^{\mathrm{miss}}$ triggers the trigger efficiency is expected to be greater than 95%. The trigger menus are currently under review and the trigger efficiencies will need to be reassessed once the new menu is available, but triggering is not expected to be a problem for this analysis. As a result a trigger efficiency of 100% was assumed in this study.

8.2.3 Object Selection and Overlap Removal

The object selection and overlap removal used in this analysis are detailed in Section 5.7.

8.3 Isolating the $t\bar{t}$ events from data

Running at a centre-of-mass energy of 10 TeV the LHC will still be a top factory, producing around 80,000 $t\bar{t}$ pairs every 200 pb^{-1} of integrated luminosity. Therefore $t\bar{t}$ events will still be very useful for first measurements in the early data taking phase. However, because of the lower centre-of-mass energy, on average the top quarks will be produced with a smaller boost. As a result the event selection cuts placed on the p_{T} of the decay products of the tt-pairs and on the $E_{\mathrm{T}}^{\mathrm{miss}}$ in order to isolate the $t\bar{t}$ events from data, must be re-optimised to accommodate this.

8.3.1 Optimisation of Event Selection Cuts for 10 TeV

The optimisation was performed using a two-step process: first a trial cut scenario was chosen and the purity of the τ-channel sample was optimised by using

the safe cuts and lepton vetoes implemented in Athena version 14 (as discussed in Section 5.6.3), second the p_T and E_T^{miss} cut thresholds were optimised to achieve a good separation of signal and background. The separation of signal and background for the second part of the optimisation process was assessed using the signal-to-background ratio (S/B) and the significance Z_n as defined in Section 6.3.4, which takes into account the uncertainty on the background estimation.

Table 8.1 shows the event selection cuts chosen for the trial cut scenario. These trial cuts are based on those used in the inclusive 0-lepton SUSY analysis for a centre-of-mass energy of 10 TeV (as described in Ref. [84]), which utilises a similar signature.

Cut	Trial Cut Scenario
Jets Cut	At least 4 jets
	$p_T(\text{jet}_1) > 80$ GeV
	$p_T(\text{jet}_{2,3,4}) > 40$ GeV
E_T^{miss} Cut	$E_T^{miss} > 80$ GeV
$\Delta\phi$ Cut	$\Delta\phi(jet_{1,2,3}, E_T^{miss}) > 0.2$
ID Cut	At least one τ
	(medium safe taus)
	$p_T > 20$ GeV
M_T Cut	$M_T < 100$ GeV
M_{jjj} Cut	$120 < M_{jjj} < 240$ GeV

Table 8.1: Event selection cuts used for the trial cut scenario.

Table 8.2 shows the resulting signal for the τ-channel when the trial cuts are applied for 200 pb^{-1} of integrated luminosity. It also shows the background from the other leptonically decaying $t\bar{t}$ processes and the W+jets processes since these were the main backgrounds for the channel for a centre-of-mass energy of 14 TeV (see Section 7.5.1). The medium safe cuts definition for taus was taken as defined by the ATLAS Tau Performance Group (see Section 5.6.3). The significance Z_n

is also given, which includes the systematic uncertainty on the background measurement. It is believed that a systematic uncertainty of 30% or better could be achieved for the SM background by performing a template fit to the shape of the backgrounds for the muon channel, where the event yield is higher. But in order to assess how the tau efficiency measurement performs if the SM background is measured with better or worse accuracy, the uncertainties on the method will be investigated assuming a SM background systematic uncertainty of 50%, 30% and 20% in Section 8.4. The central value of 30% was assumed here to obtain an estimate of the significance.

Sample	Number of events
Signal	43.9
$t\bar{t} \rightarrow e\nu jjjj$	23.1
$t\bar{t} \rightarrow \mu\nu jjjj$	13.3
$t\bar{t} \rightarrow ll\nu\nu jj$	5.4
$W \rightarrow e\nu$+jets	5.3
$W \rightarrow \mu\nu$+jets	2.3
$W \rightarrow \tau\nu$+jets	14.3
Total Background, B (using $t\bar{t}$ and W)	63.7
S/B (using $t\bar{t}$ and W)	0.7
Z_n (using $t\bar{t}$ and W)	2.0

Table 8.2: The signal, main backgrounds and significance for the τ-channel for the trial cut scenario defined in the text. An uncertainty of 30% is assumed for all SM backgrounds for the significance calculation. Results are shown for 200 pb^{-1} of integrated luminosity.

It can be seen that for both of these scenarios the background is larger than the signal, even without all SM background processes considered, and therefore the significance is low. In early data taking it will be desirable to have a significance $> 3\sigma$ to show that the reconstructed top quark has really been found.

The backgrounds for both scenarios are relatively large with the majority of the background produced by semileptonic $t\bar{t}$ decays to electrons or muons and $W \rightarrow \tau\nu$+jets events. Background from semileptonic $t\bar{t}$ decays can occur when the electrons or muons are either misreconstructed as a tau or are lost and one of the jets in the event is misreconstructed as a tau. The same is true for W+jets events. Looking at the background from W+jets events it can be seen that although the majority of events (65%) are from the process $W \rightarrow \tau\nu$+jets (where all possible decays of the τ are allowed), approximately a quarter are $W \rightarrow e\nu$+jets events.

If the background events from semileptonic $t\bar{t}$ decays to electron and muon final states are a result of the lepton being lost and one of the jets being misreconstructed as a tau, the transverse mass M_T will not obey $M_T < M_W$, therefore a harsher M_T cut could be used to eliminate these events. Figure 8.1 shows the transverse mass distribution for semileptonic $t\bar{t}$ decays and for dileptonic $t\bar{t}$ decays. It can be seen from this figure that the semileptonic decays to electrons and muons become dominant for $M_T > 75$ GeV; particularly the semileptonic decays to electrons, whereas events with a real tau predominantly have lower values of M_T.

In order to take advantage of this separation in the M_T distribution between real taus and fake taus, a harsher M_T cut of $M_T < 75$ GeV was explored. It was expected that this harsher cut should also help to reduce the background from W+jets events for the same reasons. Table 8.3 shows the signal, backgrounds and significance for the trial cut scenario with the harshened M_T cut. It can be seen that the harsher M_T cut substantially reduces the backgrounds from fake taus in electron final states. For example, the background from semileptonic $t\bar{t}$ decays to electron final states, which was the dominant background, is reduced by 34% and $W \rightarrow e\nu$+jets events are reduced by 41%. The cut also significantly reduces the backgrounds from fake taus in muon final states. The tighter M_T cut has relatively little effect on the signal with a loss of only 8%.
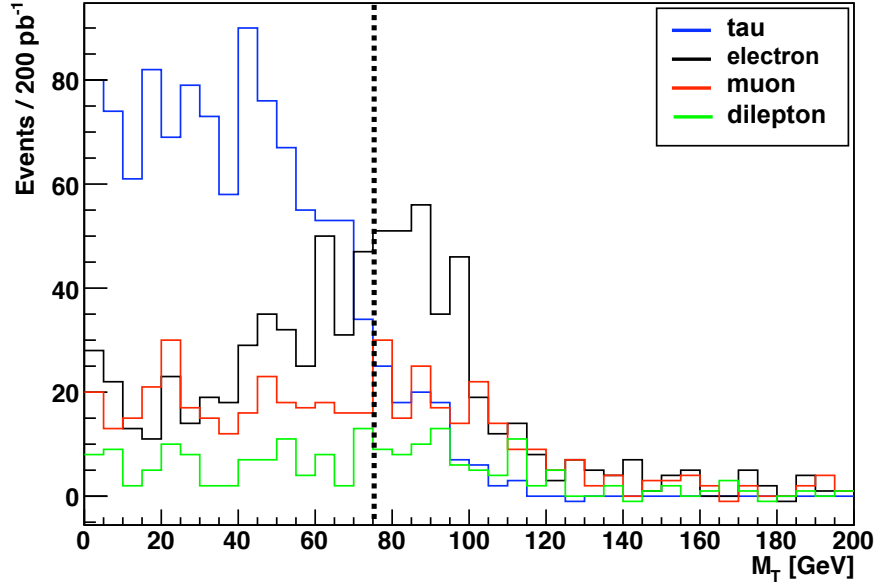
Figure 8.1: The transverse mass distribution for events were $t\bar{t}$-pairs decay semilep-
tonically to a tau (blue), to an electron (black), to a muon (red), and where the $t\bar{t}$-pairs
decay dileptonically (green). M_{T} is defined here as the invariant mass of the hardest
tau and the $E_{\mathrm{T}}^{\mathrm{miss}}$ in the transverse plane. All event selection cuts are applied except
the M_{T} cut. Results are shown for 200 pb^{-1} of integrated luminosity.

After the harsher M_{T} cut, background events from fake taus that are misrecon-
structed electrons or muons still remain since these events will obey $M_{\mathrm{T}} < M_W$.
In order to reduce these remaining events the electron and muon vetoes designed
by the ATLAS Tau Performance Group (as described in Section 5.6.3) were ex-
plored. These vetoes are designed to remove electrons and muons that have been
wrongly reconstructed as taus. Table 8.4 shows the signal, backgrounds and sig-
nificance when the vetoes are applied in combination with the harsher M_{T} cut.
It can be seen that the vetoes further reduce the remaining background from
fake taus in electron final states. The background from semileptonic $t\bar{t}$ decays
to electron final states is reduced by 57%. The background from $W \rightarrow e\nu$+jets
events is reduced by 55%. The background from fake taus in muon final states is
less affected, remaining almost the same. This is a direct result of the lower prob-
ability for a muon to be misreconstructed as a τ; the fake taus in the remaining

Sample	Number of events
Signal	40.4
$t\bar{t} \rightarrow e\nu jjjj$	15.2
$t\bar{t} \rightarrow \mu\nu jjjj$	9.4
$t\bar{t} \rightarrow ll\nu\nu jj$	4.0
$W \rightarrow e\nu$+jets	3.1
$W \rightarrow \mu\nu$+jets	1.7
$W \rightarrow \tau\nu$+jets	12.0
Total Background, B (using $t\bar{t}$ and W)	45.4
S/B (using $t\bar{t}$ and W)	0.9
Z_n	2.4

Table 8.3: The signal, main backgrounds and significance for the τ-channel for the trial cut scenario defined in the text when the M_T cut is harshened to $M_\mathrm{T} < 75$ GeV. An uncertainty of 30% is assumed on all SM backgrounds for the significance calculation. Results are shown for 200 pb^{-1} of integrated luminosity.

background from muon final states come mostly from jets being misreconstructed as taus.

In order to reduce the backgrounds further it was decided to try the tight safe cuts definition for taus as defined by the ATLAS Tau Performance Group (see Section 5.6.3). This uses a harsher set of cuts on the safe variables to define the tau, providing greater rejection against electrons and muons. Table 8.5 shows the signal, backgrounds and significance when the tight safe cuts definition was used, again applying the harsher M_T cut and the vetoes.

With the harsher M_T cut, the electron and muon vetoes and the tight safe definition for taus, the SM background is significantly reduced and is around 40% smaller than the signal.

In order to optimise the p_T and $E_\mathrm{T}^\mathrm{miss}$ cut thresholds 36 different sets of cuts where tested with full SM background. The following cuts were tested:

Sample	Number of events
Signal	38.3
$t\bar{t} \to e\nu jjjj$	6.6
$t\bar{t} \to \mu\nu jjjj$	8.8
$t\bar{t} \to ll\nu\nu jj$	3.4
$W \to e\nu$+jets	1.4
$W \to \mu\nu$+jets	1.7
$W \to \tau\nu$+jets	10.2
Total Background, B (using $t\bar{t}$ and W)	32.2
S/B (using $t\bar{t}$ and W)	1.2
Z_n	3.0

Table 8.4: The signal, main backgrounds and significance for the τ-channel for the trial cut scenario defined in the text when it is required that $M_{\mathrm{T}} < 75$ GeV and the electron and muon vetoes are applied. An uncertainty of 30% is assumed on all SM backgrounds for the significance calculation. Results are shown for 200 pb^{-1} of integrated luminosity.

- $p_{\mathrm{T}}(\mathrm{jet}_1)$: the p_{T} was varied between 65 GeV and 75 GeV in steps of 5 GeV.

- $p_{\mathrm{T}}(\mathrm{jet}_{2,3,4})$: the p_{T} was varied between 30 GeV and 40 GeV in steps of 5 GeV.

- $E_{\mathrm{T}}^{\mathrm{miss}}$: the $E_{\mathrm{T}}^{\mathrm{miss}}$ was varied between 50 GeV and 65 GeV in steps of 5 GeV.

Table 8.6 shows the signal, the background before and after the M_{jjj} cut and the significance for each of the 36 sets of cuts. Again an uncertainty of 30% was assumed for all SM backgrounds when calculating the significance.

It can be seen that the p_{T} cut on the hardest jet has approximately the same effect on both signal and background and therefore doesn't have much of an effect on the overall significance. The p_{T} of the second, third and fourth jet has more of an effect and reduces strongly both signal and background, although the effect is larger for the latter. Increasing the threshold for the $E_{\mathrm{T}}^{\mathrm{miss}}$ cut slightly also

Sample	Number of events
Signal	23.2
$t\bar{t} \to e\nu jjjj$	1.5
$t\bar{t} \to \mu\nu jjjj$	3.0
$t\bar{t} \to ll\nu\nu jj$	2.1
$W \to e\nu$+jets	0.3
$W \to \mu\nu$+jets	1.1
$W \to \tau\nu$+jets	5.4
Total Background, B (using $t\bar{t}$ and W)	13.4
S/B (using $t\bar{t}$ and W)	1.7
Z_n	3.4

Table 8.5: The signal, main backgrounds and significance for the τ-channel for the trial cut scenario defined in the text when the tight safe cuts definition for taus is used. $M_T < 75$ GeV is required and the electron and muon vetoes are applied. An uncertainty of 30% is assumed for all SM backgrounds for the significance calculation. Results are shown for 200 pb^{-1} of integrated luminosity.

reduces the background.

For this analysis a set of cuts is needed that ensures a low SM background; particularly a low QCD multijet background, the possibility of using safe trigger thresholds and provides high statistics to reduce uncertainties. Set 17, which requires $p_T(j_1) > 70$ GeV, $p_T(j_{2,3,4}) > 40$ GeV and $E_T^{\mathrm{miss}} > 55$ GeV, was chosen since it meets these requirements. This set of cuts gives a $S/B > 1$ and a significance greater than 3σ, which is good enough to provide evidence of the top peak for the semileptonic top decay to a tau. In addition, this set of cuts provides a relatively large number of events for the efficiency measurement.

To check whether any further optimisation could be made by improving the reconstruction of the hadronically decaying top quark the best methods for reconstructing the top quark (as described in Chapter 7) were compared again to check that the minimum ΔR method still performs best for these looser cut scenarios.

Set	Selection Cuts			Signal	Background		Z_n
	Jet 1	Jets 2-4	$E_\mathrm{T}^\mathrm{miss}$		Before M_{jjj} cut	After M_{jjj} cut	
1	65	30	50	92.8	335.7	126.0	2.28
2	70	30	50	88.9	320.3	121.0	2.27
3	75	30	50	84.0	326.1	119.5	2.18
4	65	35	50	67.4	228.5	93.8	2.20
5	70	35	50	65.0	226.0	92.4	2.15
6	75	35	50	61.6	224.2	91.1	2.05
7	65	40	50	46.0	127.9	36.0	3.29
8	70	40	50	44.7	127.0	35.2	3.26
9	75	40	50	42.4	125.9	34.3	3.17
10	65	30	55	84.3	277.1	114.4	2.27
11	70	30	55	81.2	273.3	112.1	2.24
12	75	30	55	77.2	269.2	108.7	2.18
13	65	35	55	61.1	180.6	87.7	2.11
14	70	35	55	59.2	178.4	86.5	2.07
15	75	35	55	56.4	177.0	85.5	1.99
16	65	40	55	42.0	105.7	32.1	3.35
17	70	40	55	41.0	104.9	31.5	3.29
18	75	40	55	39.0	104.2	31.0	3.15
19	65	30	60	75.9	188.3	86.8	2.63
20	70	30	60	73.5	184.7	84.9	2.61
21	75	30	60	70.2	181.0	81.7	2.56
22	65	35	60	55.0	141.3	62.4	2.58
23	70	35	60	53.6	139.5	61.6	2.55
24	75	35	60	51.2	138.3	60.7	2.44
25	65	40	60	38.1	90.4	28.8	2.26
26	70	40	60	37.2	89.8	28.4	3.24
27	75	40	60	35.5	89.3	27.9	3.15
28	65	30	65	68.4	163.7	77.5	2.61
29	70	30	65	66.4	160.6	76.0	2.61
30	75	30	65	63.6	157.6	73.5	2.59
31	65	35	65	49.6	121.9	55.9	2.56
32	70	35	65	48.5	120.2	55.3	2.51
33	75	35	65	46.3	119.5	54.8	2.45
34	65	40	65	34.5	75.8	25.7	3.28
35	70	40	65	33.8	75.3	25.3	3.26
36	75	40	65	32.3	74.8	24.8	3.16

Table 8.6: The signal, the background before and after the M_{jjj} cut and the significance (Z_n) for 36 sets of cuts. Results are shown for 200 pb^{-1} of integrated luminosity. An uncertainty of 30% was assumed for all SM backgrounds when calculating the significance.

Figure 8.2 shows this comparison. On the y-axis is M_{jjj} reconstructed with the highest vector summed p_{T} method, on the x-axis is M_{jjj} reconstructed with the minimum ΔR method. It can be seen that the minimum ΔR method still performs best since it picks up events lost to the high mass tail with the highest vector-summed p_{T} method.
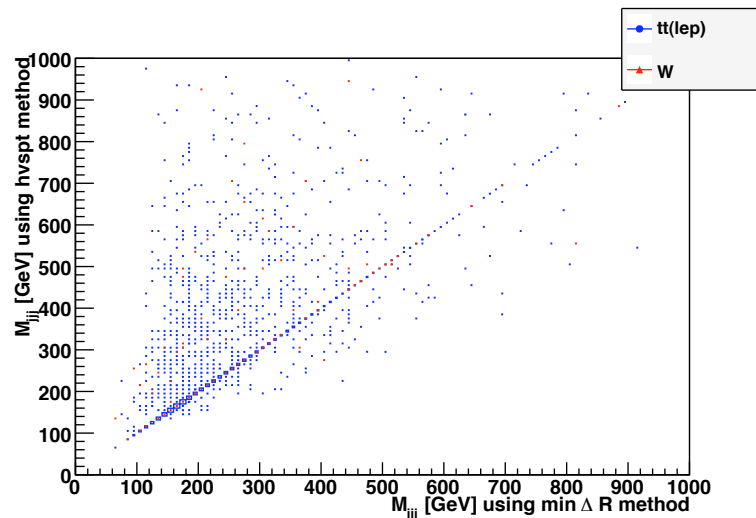
Figure 8.2: Comparison of the two methods used to reconstruct the hadronically decaying t-quark for the τ-channel. On the y-axis is M_{jjj} reconstructed with the highest vector summed p_{T} method and on the x-axis is M_{jjj} reconstructed with the minimum ΔR method. In blue the points for leptonically decaying $t\bar{t}$ events are shown and in red the W+jets background.

It was also investigated whether the reconstruction could be tightened by applying a cut on the ΔR between the three jets chosen by the minimum ΔR method to be from the hadronically decaying top quark. Figure 8.3 (top) shows the minimum ΔR between the two closest jets and Figure 8.3 (bottom) shows the minimum ΔR between the two closest jets and the third closest jet. It can be seen that there isn't a cut that would make a dramatic improvement. A possible cut that might help would be $\Delta R(jet_1 + jet_2, jet_3) < 2.4$ but this wouldn't have a big effect since most of the W+jets background is still included. In future studies more sophisticated methods for performing the top quark mass reconstruction using

a likelihood or a kinematic fit could be investigated. However, simple methods are preferred during early data taking and this is the main reason why simple reconstruction and cuts were explored.

8.3.2 Isolating the τ-channel events

Table 8.7 summarises the event selection cuts chosen for this study, for the τ-channel. Table 8.8 shows the resulting signal and SM backgrounds for 200 pb^{-1} of integrated luminosity. Statistical uncertainties and systematic uncertainties assuming a systematic uncertainty of 50%, 30% and 20% on all SM backgrounds are given. The statistical uncertainties on the SM backgrounds are calculated assuming each source of background is a gaussian with width $\sqrt{N}$, where N is the number of background events for that source. The different sources of SM background are assumed to be statistically independent and therefore the statistical uncertainties are summed in quadrature to calculate the total statistical uncertainty on the SM background. The systematic uncertainties are also assumed to be independent and are therefore summed in quadrature to give the total systematic uncertainty of the SM background.

It can be seen that the largest background comes from W+jets processes. Figure 8.4 (top) shows the M_{jjj} distribution for the signal separately from the backgrounds due to semileptonic $t\bar{t}$ decays to electron and muon final states and dileptonic $t\bar{t}$ decays. The W+jets background is also shown. Figure 8.4 (bottom) shows the resulting M_{jjj} distributions for the main SM processes. Here all of the the semileptonic and dileptonic $t\bar{t}$ decays are combined in "tt (lep)", including the signal.
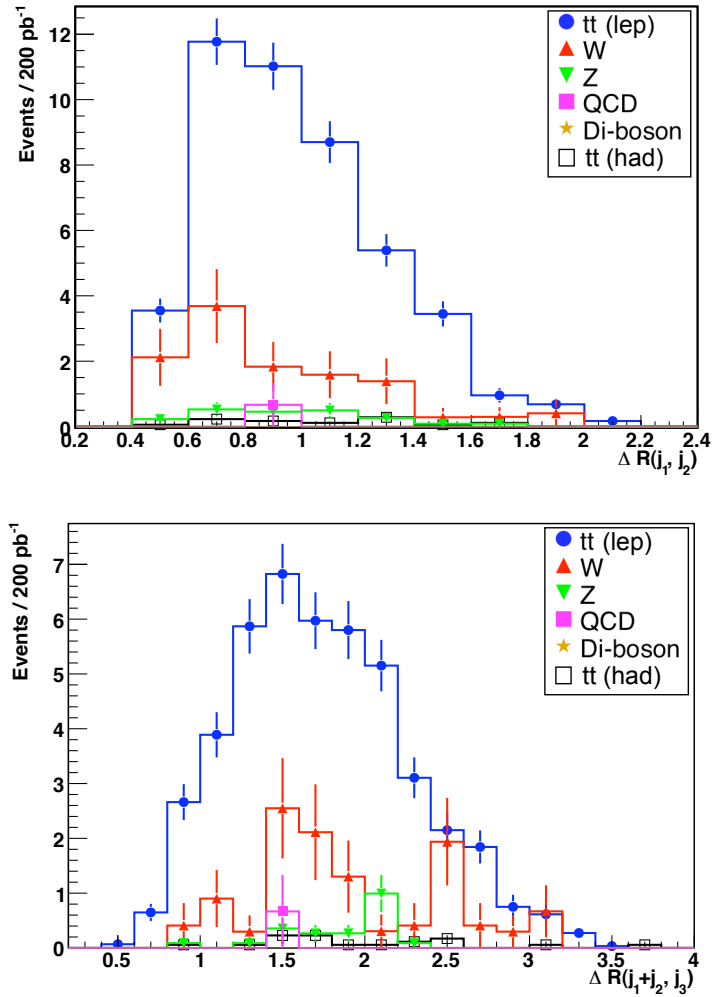
Figure 8.3: Top: The minimum ΔR between the closest two jets out of the hardest four jets. Bottom: The minimum ΔR between the vector sum of the closest two jets and the jet closest to this sum, out of the four hardest jets. Results are shown for 200 pb^{-1} of integrated luminosity.

Cuts	Central Scenario
Jets Cut	At least 4 jets
	$p_\mathrm{T}(\mathrm{jet}_1) > 70$ GeV
	$p_\mathrm{T}(\mathrm{jet}_{2,3,4}) > 40$ GeV
$E_\mathrm{T}^\mathrm{miss}$ Cut	$E_\mathrm{T}^\mathrm{miss} > 55$ GeV
$\Delta\phi Cut$	$\Delta\phi(\mathrm{j}_{1,2,3}, E_\mathrm{T}^\mathrm{miss}) > 0.2$
ID Cut	At least one τ selected using tight safe cuts
	$p_\mathrm{T} > 20$ GeV, $|\eta| < 2.5$
	electron and muon vetoes applied
M_T Cut	$M_\mathrm{T} < 75$ GeV
M_{jjj} Cut	$120 < M_{jjj} < 240$ GeV

Table 8.7: The event selection cuts chosen for the τ-channel to study the tau identification efficiency at a centre-of-mass energy of 10 TeV.

8.3.3 Isolating the μ-channel events

The event selection cuts shown in Table 8.9 were used to isolate the μ-channel events from SM backgrounds for a centre-of-mass energy of 10 TeV. The same event selection cuts were used as for the τ-channel except that the ID cut requires a muon with $p_\mathrm{T} > 30$ GeV rather than a tau with $p_\mathrm{T} > 20$ GeV. Table 8.10 shows signal and SM backgrounds after the event selection cuts, for 200 pb^{-1} of integrated luminosity. Statistical and systematic uncertainties assuming a systematic uncertainty of 50%, 30% and 20% on all SM backgrounds are given.

Table 8.11 summarises the signal S and background B after the M_{jjj} cut for the τ-channel and μ-channel for 200 pb^{-1} of integrated luminosity. It also gives the signal-to-background ratio S/B and significance Z_n assuming a 50%, 30% and 20% uncertainty on all SM backgrounds. It can be seen that even in the worse case scenario where the SM background is known with an uncertainty of 50%, a significance > 2 can be achieved for the τ-channel.

Sample	No. Events	Statistical Uncertainty	Systematic Uncertainty		
			50%	30%	20%
Signal	41.0	6.4	-	-	-
$t\bar{t} \rightarrow e\nu jjjj$	3.1	1.7	1.5	0.9	0.6
$t\bar{t} \rightarrow \mu\nu jjjj$	4.9	2.2	2.5	1.5	1.0
$t\bar{t} \rightarrow ll\nu\nu jj$	3.1	1.8	1.6	0.9	0.6
Top Hadronic	1.0	1.0	0.5	0.3	0.2
QCD multijets (light flavour)	3.9	2.0	2.0	1.2	0.8
QCD multijets (heavy flavour)	1.4	1.2	0.7	0.4	0.3
Z+jets	1.4	1.2	0.7	0.4	0.3
W+jets	11.2	3.3	5.6	3.4	2.2
Di-Boson	0.0	-	-	-	-
Single top	1.1	1.1	0.6	0.3	0.2
Total SM Bkg.	31.5	5.6	6.9	4.2	2.7

Table 8.8: The signal and SM backgrounds after the τ-channel event selection cuts are applied, for 200 pb^{-1} of integrated luminosity. Statistical uncertainties and systematic uncertainties assuming a systematic uncertainty of 50%, 30% and 20% for all SM backgrounds are given. The statistical uncertainties on the SM backgrounds are calculated assuming each source of background is a gaussian with width $\sqrt{N}$, where N is the number of events for that source of background. The different sources of SM background are assumed to be statistically independent and are therefore summed in quadrature to calculate the total statistical uncertainty on the SM background.
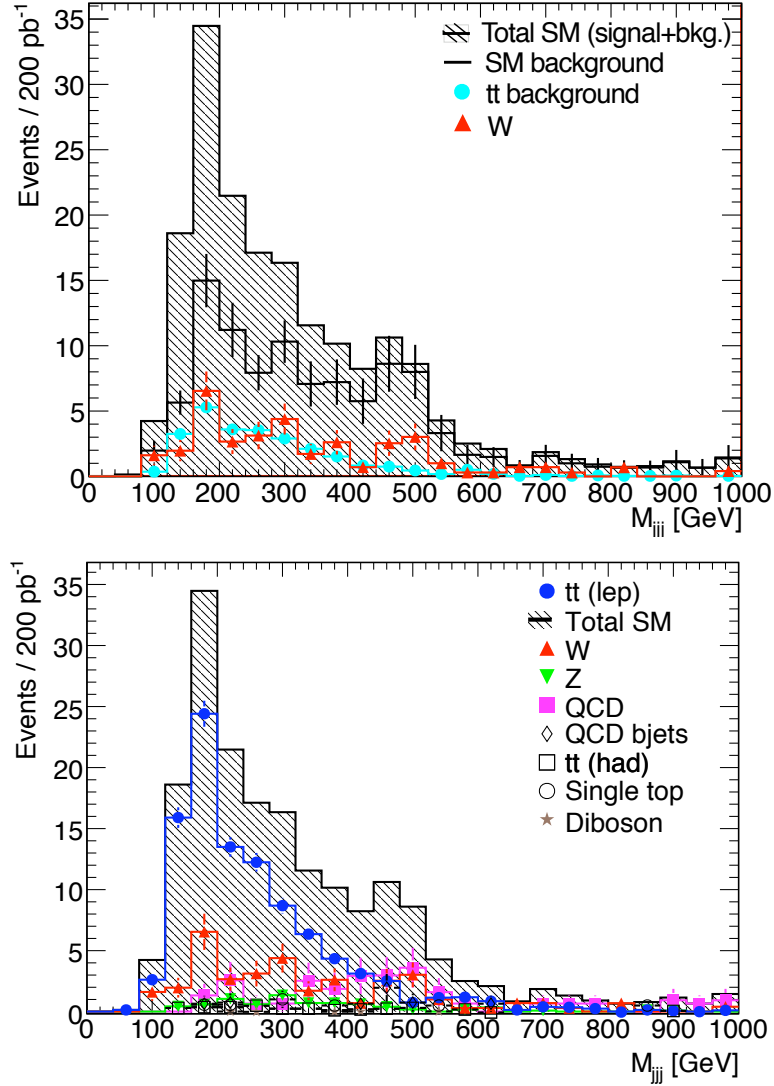
Figure 8.4: M_{jjj} distributions for the selected cut scenario (as defined in the text) to select τ-channel events when the centre-of-mass energy is 10 TeV. Results are shown for 200 pb^{-1} . Top: the M_{jjj} distribution for the signal shown separately from the SM background contributions to "tt (lep)" i.e. the backgrounds from semileptonic $t\bar{t}$ decays to electron and muon final states and dileptonic $t\bar{t}$ decays. The W+jets background is also shown. Bottom: the resulting M_{jjj} distributions for the main SM processes. Here all of the semileptonic and dileptonic $t\bar{t}$ decays are combined into "tt (lep)".

Cuts	Central Scenario
Jets Cut	At least 4 jets
	$p_T(\text{jet}_1) > 70$ GeV
	$p_T(\text{jet}_{2,3,4}) > 40$ GeV
E_T^{miss} Cut	$E_T^{\text{miss}} > 55$ GeV
$\Delta\phi Cut$	$\Delta\phi(\text{j}_{1,2,3}, E_T^{\text{miss}}) > 0.2$
ID Cut	At least one μ
	$p_T > 30$ GeV
M_T Cut	$M_T < 75$ GeV
$M_{jjj} Cut$	$120 < M_{jjj} < 240$ GeV

Table 8.9: The event selection cuts chosen for the μ-channel to study the tau identification efficiency at a centre-of-mass energy of 10 TeV.

Sample	No. Events	Statistical Uncertainty	Systematic Uncertainty		
			50%	30%	20%
Signal	165.0	12.8	-	-	-
$t\bar{t} \rightarrow e\nu jjjj$	0.2	0.4	0.1	0.1	0.0
$t\bar{t} \rightarrow \tau\nu jjjj$	0.1	0.3	0.0	0.0	0.0
$t\bar{t} \rightarrow ll\nu\nu jj$	8.7	2.9	4.3	2.6	1.7
Top Hadronic	0.2	0.4	0.1	0.1	0
QCD multijets (light flavour)	1.7	1.3	0.9	0.5	0.3
QCD multijets (heavy flavour)	0.0	-	-	-	-
Z+jets	2.9	1.7	1.5	0.9	0.6
W+jets	37.1	6.1	18.5	11.1	7.4
Di-Boson	0.04	0.2	0.02	0.01	0.01
Total SM Bkg.	55.9	7.4	19.2	11.5	7.7

Table 8.10: The signal and SM backgrounds after the μ-channel event selection cuts are applied, for 200 pb^{-1} of integrated luminosity. Statistical uncertainties and systematic uncertainties assuming a systematic uncertainty of 50%, 30% and 20% for all SM backgrounds are given. The statistical uncertainties on the SM backgrounds are calculated assuming each source of background is a gaussian with width $\sqrt{N}$, where N is the number of background events for that source. The different sources of SM background are assumed to be statistically independent and are therefore summed in quadrature to calculate the total statistical uncertainty on the SM background.

Channel	S	B	S/B	Z_n (50%)	Z_n (30%)	Z_n (20%)
τ-channel	41.0	31.5	1.3	2.3	3.3	4.1
μ-channel	165.0	55.9	3.0	5.3	> 6	> 6

Table 8.11: Signal (S) and SM background (B) after the mass window cut for τ- and μ-channels, the signal-to-background ratio S/B and the significance Z_n assuming a 50%, 30% and 20% systematic uncertainty for all SM backgrounds. Events are normalised to 200 pb^{-1} .

8.4 Measuring the tau identification efficiency

To recap the method introduced in Chapter 7, the tau identification efficiency is measured using the following relation between the τ- and μ-channels:

$$\varepsilon_{ID}^{\tau} = \frac{N_{exp.}^{\tau}}{N_{exp.}^{\mu}} \times \frac{B^{\mu}}{B^{\tau}} \times \frac{\varepsilon_{cuts}^{\mu}}{\varepsilon_{cuts}^{\tau}} \times \varepsilon_{ID}^{\mu} \qquad (8.1)$$

N_{exp}^{τ} (N_{exp}^{μ}) is the number of signal events expected for the τ-channel (μ-channel) as obtained in the previous section. The branching ratios B^{τ} and B^{μ} are well known. Therefore only the ratio of the event selection cut efficiencies $\frac{\varepsilon_{cuts}^{\mu}}{\varepsilon_{cuts}^{\tau}}$ and the ID efficiency of the muon ε_{ID}^{μ} must be obtained from the MC.

As described in Section 7.5.2, $\frac{\varepsilon_{cuts}^{\mu}}{\varepsilon_{cuts}^{\tau}}$ can be expanded as:

$$\frac{\varepsilon_{cuts}^{\mu}}{\varepsilon_{cuts}^{\tau}} = \frac{\varepsilon_{PS}^{\mu}}{\varepsilon_{PS}^{\tau}} \times \frac{\varepsilon_{jets}^{\mu}}{\varepsilon_{jets}^{\tau}} \times \frac{\varepsilon_{E_{T}^{miss}}^{\mu}}{\varepsilon_{E_{T}^{miss}}^{\tau}} \times \frac{\varepsilon_{\Delta\phi}^{\mu}}{\varepsilon_{\Delta\phi}^{\tau}} \times \frac{\varepsilon_{M_T}^{\mu}}{\varepsilon_{M_T}^{\tau}} \times \frac{\varepsilon_{M_{jjj}}^{\mu}}{\varepsilon_{M_{jjj}}^{\tau}}. \qquad (8.2)$$

In Section 7.5.2 it was shown that the ratio of the cuts involving the jets from the hadronically decaying top quark (the jets cut and the M_{jjj} cut) could be cancelled with a systematic uncertainty of 10%, since the hadronic decay of the top quark is identical for both channels if the leptons have a similar phase space and therefore the top quarks have similar energies. A check was made to ensure this assumption still holds for a centre-of-mass energy of 10 TeV. Figure 8.5 shows $\frac{\varepsilon_{cuts}^{\mu}}{\varepsilon_{cuts}^{\tau}}$ as a function of the p_{T} of the reconstructed muon. It can be seen that the ratio can still be taken as 1.0 with a systematic uncertainty of 10%.
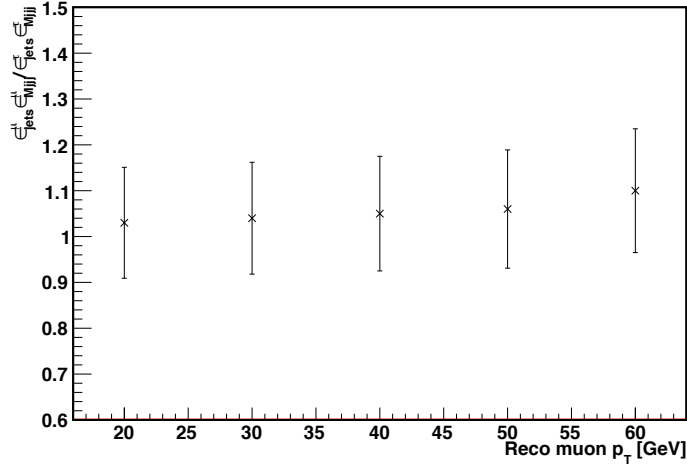
Figure 8.5: The combined ratio of the efficiencies of the cuts involving jets (the jets cut and the M_{jjj} cut) as a function of the reconstructed muon p_T for 200 pb^{-1} . The error bars indicate the statistical uncertainties.

Since the leptonic decays of the top quarks are not identical in the τ- and μ-channels due to the intrinsic E_T^{miss} of the tau, the ratio of the efficiencies of the cuts involving E_T^{miss} (the E_T^{miss} cut, $\Delta\phi$ cut and the M_T cut) must be taken from MC. This was done as described in Section 7.5.2, by extracting the real signal events in the MC using the truth information and passing these events through the event selection cuts in order to determine the true efficiencies of these cuts. Table 8.12 summarises these efficiencies and the ratio of the efficiencies for the τ- and μ-channels. The systematic uncertainty on these terms will come from how well the Monte Carlo describes the E_T^{miss} efficiency with respect to data. This can only be estimated with data. For this study an estimated conservative value of 10% was taken for the overall systematic uncertainty of the ratio of the efficiencies of the cuts involving E_T^{miss}.

The muon identification efficiency ε_{ID}^{μ} can also be extracted from Table 8.12 as described in Section 7.5.3. It can be seen that $\varepsilon_{ID}^{\mu} = 0.598\pm0.023$. The systematic uncertainty can be safely neglected since the μ-identification efficiency will be measured to an accuracy of $\sim 1\%$ with 200 pb^{-1} of data [53].

Cut Efficiency	τ-channel	μ-channel	Ratio $\frac{\mu}{\tau}$
ε_{jets}	0.180 ± 0.005	0.197 ± 0.004	1.094 ± 0.038
$\varepsilon_{M_{jjj}}$	0.553 ± 0.016	0.547 ± 0.011	0.989 ± 0.035
$\varepsilon_{E_{\mathrm{T}}^{\mathrm{miss}}}$	0.523 ± 0.022	0.462 ± 0.015	0.883 ± 0.047
$\varepsilon_{\Delta\phi}$	0.907 ± 0.018	0.901 ± 0.014	0.993 ± 0.025
ε_{ID}	0.190 ± 0.025	0.598 ± 0.023	-
ε_{M_T}	0.901 ± 0.046	0.628 ± 0.030	0.697 ± 0.049

Table 8.12: The efficiency of each selection cut, for each channel, when applying the cuts to real signal events in the Monte Carlo. Numbers are shown for 200 pb^{-1} of integrated luminosity. The uncertainties given are statistical uncertainties.

Table 8.13 summarises the elements required to measure the tau identification efficiency and presents the resulting tau identification efficiency. Statistical and systematic uncertainties are given. The overall statistical and systematic uncertainties of the tau identification efficiency measurement are calculated using Equation 7.5.

The tau identification efficiency can be extracted from the MC using the same method used to extract the muon identification efficiency (as described in Section 7.6.1). Using this method the tau identification efficiency is found to be 0.19 ± 0.02 (where the uncertainty quoted is the statistical uncertainty). Therefore, the tau identification efficiency measured using the new method presented in this thesis (as shown in Table 8.13) is in good agreement with the tau identification efficiency extracted from MC.

From Table 8.13 it can be seen that the overall uncertainty (statistical plus systematic) of the tau identification efficiency measurement ranges from 32% to 36% for 20% to 50% systematic uncertainties on the SM backgrounds respectively. Although little effort has been employed to constrain the systematic uncertainties of the method, it can been seen that the method is currently limited by statistics, with a total statistical uncertainty of 28%. This limitation is predominantly due to the relatively small number of events expected in the tau channel. This is

Term	Value	Statistical Uncertainty	Systematic Uncertainty		
			50%	30%	20%
N^{τ}_{meas}	72.5	8.5	-	-	-
N^{μ}_{meas}	220.9	14.9	-	-	-
N^{τ}_{bkg}	31.5	5.6	6.9	4.2	2.7
N^{μ}_{bkg}	55.9	7.4	19.2	11.5	7.7
$\dfrac{B^{\mu}}{B^{\tau}}\dfrac{\varepsilon^{\mu}_{PS}}{\varepsilon^{\tau}_{PS}}$	1.9				
$\dfrac{\varepsilon^{\mu}_{jets}\varepsilon^{\mu}_{M_{jjj}}}{\varepsilon^{\tau}_{jets}\varepsilon^{\tau}_{M_{jjj}}}$	1.0	0.1	0.1	0.1	0.1
$\dfrac{\varepsilon^{\mu}_{E^{miss}_{T}}\varepsilon^{\mu}_{\Delta\phi}}{\varepsilon^{\tau}_{E^{miss}_{T}}\varepsilon^{\tau}_{\Delta\phi}}\cdot\dfrac{\varepsilon^{\mu}_{MT}}{\varepsilon^{\tau}_{MT}}$	0.61	0.07	0.07	0.06	0.06
ε^{μ}_{ID}	0.60				
ε^{τ}_{ID}	0.18	0.05	0.04	0.03	0.03

Table 8.13: Summary of the values for each term contributing to the τ-identification efficiency for both the low p_{T} and high p_{T} scenarios for 200 pb^{-1} of integrated luminosity. Three columns are given for the systematic uncertainty corresponding to the 50%, 30% and 20% systematic uncertainty on the SM background.

partly due to the fact that the safe cuts for taus were not optimised for busy environments like $t\bar{t}$; the tight safe cuts were optimised for clean $Z \to \tau\tau$ events. Future studies should investigate how the statistical uncertainty could be reduced. One possibility is that $W \to \tau\nu+$jets could be included as signal to boost the number of events. This approach is valid provided the goal is to measure the tau identification efficiency in busy environments and not specifically for $t\bar{t}$ events. Another possibility may be to use an alternative to the tight safe cuts.

The largest contribution to the SM background and its systematic uncertainty comes from $W+$jets processes. It is believed that the uncertainty on the measurement of this background could be reduced by using a template fit to this background. For such a method a systematic uncertainty on the SM background of 30% or less is expected. For a systematic uncertainty of 30% the systematic uncertainty on the tau identification efficiency measurement is $\pm 17\%$.

8.5 Comments regarding the performance of the method for 7 TeV

Process	Reduction factor (10 TeV/7 TeV)
$t\bar{t}$	2.5
$W+$jets	1.5
$Z+$jets	1.5
QCD multijets	2.5

Table 8.14: Expected reduction in the production cross-sections of different processes when moving from a centre-of-mass of 10 TeV to a centre-of-mass of 7 TeV. Taken from Figure 1.2

Since the initial centre-of-mass energy of the LHC will be 7 TeV, it was estimated how the method would perform for this energy. This was done by scaling the expected number of events to the reduced expected cross-sections for 7 TeV. The

Channel	S	B	S/B	$Z_n(50\%)$	$Z_n(30\%)$	$Z_n(20\%)$
τ-channel (200 pb^{-1})	16.4	14.5	1.1	1.7	2.3	2.8
μ-channel (200 pb^{-1})	66.0	31.0	2.1	3.6	5.2	> 6
τ-channel (1 fb^{-1})	82.0	72.5	1.1	2.1	3.3	4.5
μ-channel (1 fb^{-1})	330.0	155.2	2.1	4.1	> 6	> 6

Table 8.15: The estimated signal (S), SM background after all selection cuts (B), the signal-to-background ratio (S/B) and the significance (Z_n) assuming a 50%, 30% and 20% systematic uncertainty on all SM backgrounds, for the τ- and μ-channels, for 200 pb^{-1} and 1 fb^{-1} of integrated luminosity at 7 TeV centre-of-mass energy.

reduction factors are given in Table 8.14 and the resulting signal, background and significances are shown in Table 8.15 for 200 pb^{-1} and 1 fb^{-1} of integrated luminosity at a centre-of-mass energy of 7 TeV. It can be seen that the situation for 1 fb^{-1} at 7 TeV centre-of-mass energy is similar to the situation for 200 pb^{-1} at 10 TeV. For 1 fb^{-1} it is estimated that 3.3σ evidence of $t\bar{t}$ decaying semileptonically to a tau could be expected assuming systematic uncertainties on the SM background estimation of up to 30%, providing important support to analyses aimed to discover new physics with tau final states. This estimation is rather simplified and does not take into account the challenges at 7 TeV due to the less boosted $t\bar{t}$ topologies, which will have an impact on the statistics due to trigger limitations and will also challenge the top-quark reconstruction method proposed. Further studies are required to investigate the performance of this method for a centre-of-mass energy of 7 TeV, however the estimates made here show that it appears to be a potentially promising method for measuring the tau identification efficiency in early data.

8.6 Summary and Conclusions

A new method for measuring the tau identification efficiency in data using a sample of semileptonic $t\bar{t}$ events was presented in Chapter 7. The performance of this method when the centre-of-mass energy of the LHC is 10 TeV was investigated in this chapter. Measuring the tau identification efficiency in an early data

taking phase with a centre-of-mass energy of 10 TeV is more challenging than for a centre-of-mass energy of 14 TeV. The $t\bar{t}$ pairs are less boosted and so the event selection cuts used to isolate the $t\bar{t}$ events from the SM background must be loosened giving a poorer rejection against SM backgrounds. Also, the cross-section for $t\bar{t}$ production drops faster than the cross-section for $W+$jets processes, the dominant background to this analysis, with decreasing centre-of-mass energy as can be seen from Figure 1.2 so this background is larger than for 14 TeV. Despite these difficulties it has been shown that the method introduced in Chapter 7 for measuring the tau identification efficiency using $t\bar{t}$ events is able to correctly measure the tau identification efficiency for a centre-of-mass energy of 10 TeV and 200 pb^{-1} of integrated luminosity. The method could therefore be suitable during the early data taking phase of the experiment for a centre-of-mass energy of 10 TeV.

The statistical and systematic uncertainties on the tau identification efficiency measurement have been shown to be $\pm 28\%$ and $\pm 22\%$ respectively in a worst case scenario where the systematic uncertainty on the SM background is 50%. The uncertainty of the method is currently dominated by the statistical uncertainty partly due to the relatively small number of events expected in the tau channel. Future studies should investigate how this uncertainty could be reduced.

Simple estimates of the performance of the tau identification efficiency measurement for a centre-of-mass energy of 7 TeV have been made by scaling the expected events for each channel by the expected reduction in the cross-sections of the SM processes involved. According to these estimates the situation for 1 fb^{-1} at a centre-of-mass energy of 7 TeV can be expected to be similar to the situation for 200 pb^{-1} at 10 TeV. However, these estimates do not take into account the reduction in the boost of the top quarks at 7 TeV that may provide challenges for triggering and top-quark reconstruction. Further studies are required to investigate the performance of this method for a centre-of-mass energy of 7 TeV, however the estimates made here show that it appears to be a potentially promising method for measuring the tau identification efficiency in early data.

Chapter 9

Summary and Conclusions

Despite its success, the Standard Model has a number of short-comings that lead particle physicists to believe the Standard Model is only a low-energy approximation of a more fundamental theory. One of the most promising candidates for an extension of the Standard Model is supersymmetry. A new inclusive search for SUSY in tau final states has been developed for the ATLAS experiment. The search focuses on the signature of taus, jets and missing transverse energy. Analyses with different jet multiplicities (4, 3 and 2-jets) have been studied. The requirement of the tau significantly reduces the abundant QCD multijet background making the mode potentially more robust than other modes already in use that focus only on jets and missing transverse energy as the signature.

The discovery reach for R-parity conserving mSUGRA models has been studied for a centre-of-mass energy of 14 TeV and an integrated luminosity of 1fb^{-1}. It has been shown that this tau mode is competitive with other inclusive search modes used by the ATLAS Collaboration, particularly for regions of the SUSY parameter space with high $\tan\beta$ where tau decays are enhanced. It has been shown that models with high $\tan\beta$ and squark and gluino masses less than $\mathcal{O}(1$ TeV) are within the 5σ discovery reach.

Tau leptons will play an important role in the physics expected at the LHC both in Standard Model and beyond the Standard Model processes. However, due to their prompt decay, taus are challenging objects to identify, but the excel-

lent tracking and calorimetry of the ATLAS detector should allow for efficient identification and reconstruction of hadronically decaying taus. The validation of the ATLAS tau identification will be important in early data. A new method for determining the tau identification efficiency using $t\bar{t}$ decays, which will be abundant at the LHC, has been developed. The method isolates the semileptonically decaying $t\bar{t}$ events by requiring high missing transverse energy, a number of high energy jets and by reconstructing the mass of the hadronically decaying t-quark. As a result, this method does not suffer from a large background from QCD multijet events and it does not require tau triggering. It also does not rely on b-tagging to reconstruct the top quark mass and is thus a suitable method for early data. The method has been tested using pseudo-data with reduced tau identification efficiencies and good agreement was found between the measured tau identification efficiencies and those expected. The statistical and systematic uncertainties on the tau identification efficiency measurement have been shown to be $\pm 11\%$ ($\pm 16\%$) and $\pm 19\%$ ($\pm 19\%$) respectively for taus with $p_T > 20$ GeV ($p_T > 40$ GeV) assuming an integrated luminosity of 1 fb^{-1} for a centre-of-mass energy of 14 TeV.

Measurement of the tau identification efficiency in an early data taking phase with a centre-of-mass energy of 10 TeV using the new method has also been investigated. Despite this being a more challenging environment, it has been shown that the method for measuring the tau identification efficiency using $t\bar{t}$ events is able to correctly measure the tau identification efficiency for a centre-of-mass energy of 10 TeV and 200 pb^{-1} of integrated luminosity. The method is therefore a promising method for the 10 TeV data taking phase of the ATLAS experiment. The statistical and systematic uncertainties on the tau identification efficiency measurement have been shown to be $\pm 28\%$ and $\pm 22\%$ respectively in a worst case scenario where the systematic uncertainty on the SM background is 50%. The uncertainty of the method is currently dominated by the statistical uncertainty partly due to the relatively small number of events expected in the tau channel. Future studies should investigate how this uncertainty could be reduced. The largest contribution to the SM background and its uncertainty comes from W+jets processes. It is believed that the uncertainty on the measurement

of this background could be reduced by using a template fit to this background. For such a method a systematic uncertainty of 30% or less is expected. For a systematic uncertainty of 30% the systematic uncertainty on the tau identification efficiency measurement is $\pm 17\%$.

Simple estimates of the performance of the tau identification efficiency measurement for a centre-of-mass energy of 7 TeV have been made by scaling the expected events for each channel by the expected reduction in the cross-sections of the SM processes involved. According to these estimates the situation for 1 fb^{-1} at a centre-of-mass energy of 7 TeV can be expected to be similar to the situation for 200 pb^{-1} at 10 TeV. However, these estimates do not take into account the reduction in the boost of the top quarks at 7 TeV that may provide challenges for triggering and top-quark reconstruction. Further studies are required to investigate the performance of this method for a centre-of-mass energy of 7 TeV. However the estimates made here show that the method appears to be a potentially promising method for measuring the tau identification efficiency in early data.

Bibliography

[1] W. S. C. Williams. *Nuclear and Particle Physics*, Oxford University Press, 1991. 1

[2] A. D. Martin F. Halzen. *Quarks and Leptons: An Introductory Course in Modern Particle Physics*, John Wiley Sons, 1984. 24

[3] B. R. Martin. Nuclear and Particle Physics, Wiley-Blackwell; 2nd Edition, 2006. 1

[4] S. P. Martin. *A Supersymmetry Primer*, arXiv:hep-ph/9709356, 2008. 1, 10, 11, 12, 13, 14, 15, 16, 18, 95, 96, 97, 194, 198, 199

[5] I. J. R. Aitchison. *Supersymmetry and the MSSM: An Elementary Introduction*, arXiv:hep-ph/0505105v1, 2005. 1, 14, 15, 16, 203

[6] F. I. Stancu. *Group theory in subnuclear physics*, Clarendon Press, 2007. 2

[7] S. Pokorski. *Gauge Field Theories*, Cambridge University Press; 2nd Edition, 2000. 2

[8] C. Becchi. *Introduction to Gauge Theories*, arXiv:hep-ph/9705211v1, 1997. 2

[9] C. Amsler and others (Particle Data Group). PL 667, 1 (2008) and 2009 partial update for the 2009 edition (http://pdg.lbl.gov). 2, 4, 6, 7, 9, 12, 14, 16, 17, 19, 20, 22, 25, 29, 195, 203

[10] S. Dawson. *Introduction to Electroweak Symmetry Breaking*, arXiv:hep-ph/9901280v1, 1999. 3, 4

[11] S. Catani et al. *QCD*, arXiv:hep-ph/0005025v1, 2000. 5, 26, 194

[12] The ATLAS Collaboration. *Expected Performance of the ATLAS Experiment - Detector, Trigger and Physics: Top Quark Physics*, arXiv:hep-ex/0901.0512, 2008. 6, 7, 9, 125

[13] M. W. Grunewald. *Combined Electroweak Analysis*, arXiv:hep-ph/0709.3744, 2007. 11

[14] C. Quigg B. W. Lee and H. B. Thacker. *Weak interactions at very high energies: The role of the Higgs-boson mass*, Phys. Rev. **D16**, 1519-1531, 1977. 11

[15] K. R. Dienes. *String Theory and the Path to Unification: A Review of Recent Developments*, Physics Reports **287** 6:447-525, 1997. 11, 12, 194

[16] G. G. Ross and R. G. Roberts. *Minimal supersymmetric unification predictions*, Nuclear Physics **B377** 3:571-592, 1992. 17

[17] LEPSUSYWG, ALEPH, DELPHI, L3 and OPAL experiments, note LEPSUSYWG/04-01.1, http://lepsusy.web.cern.ch/lepsusy/Welcome.html. 19, 195

[18] LEPSUSYWG, ALEPH, DELPHI, L3 and OPAL experiments, note LEPSUSYWG/02-04.1, http://lepsusy.web.cern.ch/lepsusy/Welcome.html. 19

[19] LEPSUSYWG, ALEPH, DELPHI, L3 and OPAL experiments, note LEPSUSYWG/04-07.1, http://lepsusy.web.cern.ch/lepsusy/Welcome.html. 20, 195

[20] LEPSUSYWG, ALEPH, DELPHI, L3 and OPAL experiments, note LEPSUSYWG/02-06.2, http://lepsusy.web.cern.ch/lepsusy/Welcome.html. 20

[21] The CDF Collaboration. *Search for Gluino and Squark Production in Multijets Plus Missing $E_{\rm T}$ Final States*, 2006, http://www-cdf.fnal.gov. 21, 195

[22] D0 Collaboration: V. Abazov et al. *Search for squarks and gluinos in events with jets and missing transverse energy using 2.1 fb^{-1} of ppbar collision data at $\sqrt{s}$=1.96 TeV*, Phys. Lett. **B660** 449-457, 2008. 21

[23] *WMAP*, http://map.gsfc.nasa.gov/. 21

[24] D. N. Spergel et al. *Wilkinson Microwave Anisotropy Probe (WMAP) Three Year Results: Implications for Cosmology*, The Astrophysical Journal **170** 377, 2007. 21

[25] T. aaltonen and others (on behalf of the cdf collaboration). *Search for $B_s^0 \to \mu^+\mu^-$ and $B^0 \to \mu^+\mu^-$ Decays with 2 fb^{-1} of $p\bar{p}$ Collisions*, Phys. Rev. Lett. **100** 101802, 2008. 22

[26] J. Ellis and et al. *Supersymmetric Dark Matter in Light of WMAP*, Phys. Lett. **B565** 176, 2003. 23, 195

[27] *The CTEQ Group*, http://zebu.uoregon.edu/ parton/partonCTEQ.html. 25

[28] A. D. Martin. *The structure of the proton*, Contemporary Physics **36** 5:335-353, 1995. 25

[29] M. D. Shapiro and J. L. Siegrist. *Hadron Collider Physics*, Annual Review of Nuclear and Particle Science **41** 97-132, 1991. 25

[30] L. Evans and P. Bryant. *LHC Machine*, Journal of Instrumentation **3** S08001, 2008. 30

[31] The ATLAS Collaboration. *The ATLAS Experiment at the CERN Large Hadron Collider*, Journal of Instrumentation **3** S08003, 2008. 30, 31, 36, 38, 39, 41, 44, 45, 46, 47, 49, 50, 81, 196

[32] The ATLAS Collaboration. *ATLAS detector and physics performance. Technical design report* Vol. 1, CERN-LHCC-99-014, 1999. 30, 41, 50, 196

[33] *ATLAS public images*, http://atlas.ch/photos/index.html. 32, 35, 36, 37, 40, 44, 195, 196

[34] The ATLAS Collaboration. *ATLAS Muon Spectrometer: Technical Design Report*, CERN-LHCC-97-022, 1997. 33, 48, 195, 196

[35] The ATLAS Collaboration. *Expected Performance of the ATLAS Experiment - Detector, Trigger and Physics: The Expected Performance of the Inner Detector*, arXiv:hep-ex/0901.0512, 2008. 35

[36] The ATLAS Collaboration. *ATLAS Calorimeter Performance: Technical Design Report*, CERN-LHCC-96-40, 1996. 43

[37] J. Andreeva et al. *High-Energy Physics on the Grid: the ATLAS and CMS Experience*, Journal of Grid Computing **6** 1:3-13, 2008. 51

[38] *Worldwide LHC Grid Computing*, http://lcg.web.cern.ch/LCG/. 51

[39] *Athena Framework*, https://twiki.cern.ch/twiki/bin/view/Atlas/AthenaFramework. 52

[40] *ATLAS Work Book*, https://twiki.cern.ch/twiki/bin/view/Atlas/WorkBookFullChain. 54, 196

[41] S. Mrenna T. Sjostrand and P. Skands. *PYTHIA 6.4 physics and manual*, JHEP **0605**:026, arXiv:hep-ph/0603175, 2006. 55

[42] G. Corcella et al. *HERWIG 6: An event generator for hadron emission reactions with interfering gluons (including supersymmetric processes)*, JHEP **01**:010, arXiv:hep-ph/0011363, 2001. 55

[43] J. Forshaw J. Butterworth and M. Seymour. *Multiparton interactions in photoproduction at HERA*, Z. Phys. **C72** 637-646, arXiv:hep-ph/9601371, 1996. 55

[44] A. Moraes et al. *Prediction for minimum bias and the underlying events at LHC energies*, Eur. Phys. J. **C50** 435-466, 2007. 55

[45] M. Mangano et al. *ALPGEN, a generator for hard multiparton processes in hadronic collisions*, JHEP **07** 001, arXiv:hep-ph/0206293, 2003. 55

[46] J. Alwall et al. *Comparative study of various algorithms for the merging of parton showers and matrix elements in hadronic collisions*, Eur. Phys. J. **C53** 473-500, 2008. 56

[47] S. Frixione and B.R. Webber. *Matching NLO QCD computations and parton shower simulations*, JHEP **06** 029, arXiv:hep-ph/0204244, 2002. 56

[48] H. Baer F. Paige, S. Protopopescu and X. Tata. *ISAJET 7.69: A Monte Carlo event generator for pp, $p\bar{p}$, and e^+e^- reactions*, arXiv:hep-ph/0312045, 2003. 56

[49] S. Jadach et al. *The tau decay library TAUOLA: Version 2.4.*, Comput. Phys. Commun. **76** 361-380, 1993. 56

[50] S. Agnostinelli et al. *GEANT4: A simulation toolkit.*, Nucl. Intrum. Meth. **A506**, 250-303, 2003. 56

[51] K. Assamagan et al. *The ATLAS Monte Carlo Project*, To be submitted to JINST 2009. 56, 57

[52] E. Richter-Was et al. *ATLFAST 2.0 a fast simulation package for ATLAS*, ATL-PHYS-INT-98-131, 1998. 57

[53] The ATLAS Collaboration. *Expected Performance of the ATLAS Experiment - Detector, Trigger and Physics*, arXiv:hep-ex/0901.0512, 2008. 58, 94, 99, 128, 176

[54] W. Beenakker et al. *Squark and gluino production at hadron colliders*, Nucl. Phys. **B492** 51-103, 1997. 59

[55] W. Beenakker et al. *The production of charginos/neutralinos and sleptons at hadron colliders*, Phys. Rev. Lett. **83** 3780-3783, 1999.

[56] *Prospino2*, http://www.ph.ed.ac.uk/ tplehn/prospino/. 59

[57] D. Stump et al. *Inclusive jet production, parton distributions, and the search for new physics*, JHEP **10** 046, 2003. 59

[58] J. Abdallah et al. *Propsects for SUSY discovery based in inclusive searches with the ATLAS detector at the LHC (Long Version)*, ATL-COM-PHYS-2009-261, 2009. 62, 82, 85, 87, 88, 92, 94, 98, 101, 197, 198

[59] K. Melnikov and F. Petriello. *Electroweak gauge boson production at hadron colliders through $O(\alpha(s)^2)$*, Phys. Rev. **D74** 114017, 2006. 61, 67

[60] J. Campbell and J. Ellis. User guide available at http://mcfm.fnal.gov/, 2007. 64, 67

[61] S. Abdulling et al. *The qcd, ew and higgs working group: Summary report*, arXiv:hep-ph/0604120:88, 2006. 67

[62] B. P. Kersevan and R. W. Elzbieta. *The monte carlo generator acermc version 3.5 with interfaces to pythia 6.4, herwig 6.5 and ariadne 4.1*, arXiv:hep-ph/0405247, 2008. 67

[63] The ATLAS Collaboration. *Expected Performance of the ATLAS Experiment - Detector, Trigger and Physics: Jet Reconstruction Performance*, arXiv:hep-ex/0901.0512, 2008. 68, 70

[64] The ATLAS Collaboration. *Expected Performance of the ATLAS Experiment - Detector, Trigger and Physics: Reconstruction and identification of electrons in ATLAS*, arXiv:hep-ex/0901.0512, 2008. 69, 81

[65] S. Hassini et al. *A muon identification and combined reconstruction procedure for the ATLAS detector at the LHC using the MUONBOY, STACO and MuTag reconstruction packages*, Nucl. Instrum. Meth. **A 572** 77-70, 2007. 70

[66] D. Fassouliotis et al. *Muon Identification using the MUID package*, ATL-COM-MUON-2003-003, 2003. 70

[67] Th. Lagouri et al. *A Muon Identification and Combined Reconstruction Procedure for the ATLAS Detector at the LHC at CERN*, ATL-CONF-2003-011, 2003. 70

[68] The ATLAS Collaboration. *Expected Performance of the ATLAS Experiment - Detector, Trigger and Physics: Measurement of Missing Transverse Energy*, arXiv:hep-ex/0901.0512, 2008. 71

[69] The ATLAS Collaboration. *Expected Performance of the ATLAS Experiment - Detector, Trigger and Physics: Reconstruction and identification of hadronic tau decays with ATLAS*, arXiv:hep-ex/0901.0512, 2008. 72, 75, 76, 80, 85, 124, 197

[70] The ATLAS Collaboration. *Expected Performance of the ATLAS Experiment - Detector, Trigger and Physics: Detector Level Jet Corrections*, arXiv:hep-ex/0901.0512, 2008. 72

[71] A. Christov et al. *Performance of the tau reconstruction and identification algorithm with release 14.2.10*, ATL-COM-PHYS-2008-122, 2009. 76

[72] Philip Bechtle et al. *Cut Based Identification of Hadronic τ Decays*, ATL-PHYS-INT-2009-082, 2009. 77

[73] A. Kaczmarska and S. Lai. *Reconstruction and Identification of Hadronic Tau Decays with ATLAS*, ATL-PHYS-PROC-2008-02, 2008. 80

[74] P. Bechtle et al. *Identification of hadronic tau decays with the ATLAS detector: Tau leptons in discovery physics*, ATL-PHY-INT-2008-003, 2008. 80, 98

[75] The ATLAS Collaboration. *Expected Performance of the ATLAS Experiment - Detector, Trigger and Physics: Prospects for Supersymmetry Discovery Based on Inclusive Searches*, arXiv:hep-ex/0901.0512, 2008. 90, 91, 94, 98, 100, 117, 119, 198, 200, 204

[76] F. Ahles. Ph.D. Thesis, to be published. 91

[77] J. D. Wells. *The importance of tau leptons for supersymmetry searches at the Tevatron*, Mod. Phys. Lett. **A13** 1923, 1998. 98, 99, 116

[78] The ATLAS Collaboration. *ATLAS High-Level Trigger, Data Acquisition and Controls Technical Design Report*, CERN-LHCC-2003-022, 2003. 100

[79] The ATLAS Collaboration. *ATLAS detector and physics performance. Technical design report*, Vol. 2, CERN-LHCC-99-15, 1999. 102

[80] The ATLAS Collaboration. *Expected Performance of the ATLAS Experiment - Detector, Trigger and Physics: Data-Driven Determinations of W, Z and Top Backgrounds to Supersymmetry*, arXiv:hep-ex/0901.0512, 2008. 112

[81] The ATLAS Collaboration. *Expected Performance of the ATLAS Experiment - Detector, Trigger and Physics: Estimation of QCD Backgrounds to Searches for Supersymmetry*, arXiv:hep-ex/0901.0512, 2008. 112

[82] D. Lumb S. Caron and X. Portell Bueso. *Measuring Tau Identification Efficiency With $t\bar{t}$ Events*, ATL-PHYS-INT-2009-058, 2009. 123

[83] D. Lumb S. Caron and X. Portell Bueso. *Prospects for the Semileptonic Top Decay to a Tau Lepton and the Measurement of Tau Identification Efficiency*, ATL-PHYS-INT-2010-070, 2010. 158

[84] S. Caron et al. *Prospects for Supersymmetry and Universal Extra Dimensions discovery based on inclusive searches at a 10 TeV centre-of-mass energy with the ATLAS detector*, ATL-PHYS-PUB-2009-084; ATL-COM-PHYS-2009-342, 2009. 160

List of Figures

List of Tables